SANDIA REPORT
SAND2019-xxxx
Printed September 2019

Sandia National Laboratories

# Uncertainty Quantification of Microstructural Material Variability Effects

Reese E. Jones, Brad L. Boyce, Ari L. Frankel, Krishna Garikipati, Nathan Heckman, Mohammad Khalil, Jakob T. Ostien, Francesco Rizzi, Kousuke Tachida, Gregory H. Teichert, Jeremy A. Templeton

Prepared by
Sandia National Laboratories
Albuquerque, New Mexico 87185
Livermore, California 94550

Issued by Sandia National Laboratories, operated for the United States Department of Energy by National Technology & Engineering Solutions of Sandia, LLC.



Available to DOE and DOE contractors from

U.S. Department of Energy
Office of Scientific and Technical Information
P.O. Box 62
Oak Ridge, TN 37831

Telephone: (865) 576-8401
Facsimile: (865) 576-5728
E-Mail: reports@osti.gov
Online ordering: http://www.osti.gov/scitech

Available to the public from

U.S. Department of Commerce
National Technical Information Service
5301 Shawnee Road
Alexandria, VA 22312

Telephone: (800) 553-6847
Facsimile: (703) 605-6900
E-Mail: orders@ntis.gov
Online order: https://classic.ntis.gov/help/order-methods

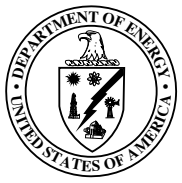

# ABSTRACT

This project has developed models of variability of performance to enable robust design and certification. Material variability originating from microstructure has significant effects on component behavior and creates uncertainty in material response. The outcomes of this project are uncertainty quantification (UQ) enabled analysis of material variability effects on performance and methods to evaluate the consequences of microstructural variability on material response in general.

Material variability originating from heterogeneous microstructural features, such as grain and pore morphologies, has significant effects on component behavior and creates uncertainty around performance. Current engineering material models typically do not incorporate microstructural variability explicitly, rather functional forms are chosen based on intuition and parameters are selected to reflect mean behavior. Conversely, mesoscale models that capture the microstructural physics, and inherent variability, are impractical to utilize at the engineering scale. Therefore, current efforts ignore physical characteristics of systems that may be the predominant factors for quantifying system reliability. To address this gap we have developed explicit connections between models of microstructural variability and component/system performance. Our focus on variability of mechanical response due to grain and pore distributions enabled us to fully probe these influences on performance and develop a methodology to propagate input variability to output performance.

This project is at the forefront of data-science and material modeling. We adapted and innovated from progressive techniques in machine learning and uncertainty quantification to develop a new, physically-based methodology to address the core issues of the Engineering Materials Reliability (EMR) research challenge in modeling constitutive response of materials with significant inherent variability and length-scales.

# CONTENTS

# LIST OF FIGURES

# LIST OF TABLES

# 1. OVERVIEW

Variability of material response is ubiquitous and especially pronounced in manufactured and natural materials where the creation process is not tightly controlled. Rock, biological tissue, nanoscale materials, and additively manufactured (AM) materials are particular examples were variability is significant. Robust design requires accounting for this variability in the design process. The primary goal of this project is to create models of material variability that can be used to augment the traditional design process. We focus on AM metals, where microstructural sources of variability are widely agreed to be: porosity, surface defects and deviations from the nominal geometry, non-optimal grain structure, and residual stresses due to the sintering process. In addition to direct experimental investigation, we used two broad classes of modeling techniques to address the challenges; we employed uncertainty quantification (UQ) methods to predict the distributions of response and machine learning (ML).

Our specific achievements are:

- Technological developments to bring characterization on par with high-throughput mechanical testing: demonstrated femtosecond laser cutting for rapid surface preparation for electron backscatter diffraction, and deployed 30 times faster electron backscatter imaging systems. These developments enable characterization of the statistics and distributions of microstructure, and pairing this information with corresponding high-throughput tests. This will be the basis for breakthroughs in structure-property-mechanism discovery.
- *In situ* investigation of how pores in stainless steel evolve under deformation. We observed sub-threshold voids emerge, voids grow and merge, and voids migrate to the surface. These observations will impact plasticity-damage models of this a related materials especially the processes leading to failure.
- We developed a technique for modelling and calibrating both voids visible in computed tomography (CT) scans and the invisible sub-threshold population. The visible voids are represented explicitly in the mesh via a Karhunen-Loève expansion based on the CT information and the unresolved population are represented with a damage model. This methodology is generally applicable to all additively manufactured metals and can accurately predict failure.
- Using a method of embedded uncertainty, where model parameters are given distributions, we are able to assess and represent material variability through the joint distribution of the parameters of a selected material model [1]. The fact that this approach maps observed variable mechanical response of an ensemble of test specimens onto interpretable material parameters is crucial in inferring mechanisms for the observed variability. For instance, wide distributions of parameters controlling failure versus those determining elastic response imply that defects are eliciting the distribution of response.
- Bayesian model selection methodology to determine which parameters vary due to microstructure and which are uncertain due to merely a lack of data [1]. Since all calibrated parameters are uncertain given limited data, this is key to assessing which physical

parameters are actually varying across the population of test samples and hence which properties should vary in making predictions at the component or assemblage level.

- We extended our Bayesian methods to map variability of response onto distributions of parameters to handle aleatoric (*e.g.* distribution of voids) and epistemic (*e.g.* the value of the yield parameter in a plasticity model) sources of variablity. This calibration technique is specifically useful in modeling AM materials and also quite general to calibrating models of materials with microstructure where high dimensional spaces describing the location of voids and other defects are involved.
- We generalized the use classical representation theory to construct neural network models of plasticity [2] and are currently extending it to Gaussian process models. The use of representation theory in machine learning is a key use of domain knowledge in creating models from data. Specifically, it enables direct satisfaction of physical symmetries and principles so that they do not need to be learned approximately from data. Application of this technique leads to more stable predictions and a many fold smaller burden on training data collection.
- Using only images of initial microstructure and a novel hybrid convolutional-recurrent neural network we are able to predict the stress-strain and full field stress response of polycrystals with greater than 95% accuracy [3]. These developments usher in a whole new class of microstructural material models that are many orders of magnitude cheaper to evaluate. These models enable more rapid uncertainty quantification and more effect probing and optimization of structure-property relationships. This ML architecture can used to mine and interpret the wealth of microstructural imaging data being produced. Experimental data and lower fidelity simulation data could be used in conjunction in the training of these models.

Following sections document the focus and progress of the project. Sec. 2 discusses microstructural influences on the mechanical response of metals. Sec. 3 develops uncertainty quantification theory to model material variability by mapping it onto distributions of physical parameters and handling aleatoric aspects of microstructure. Sec. 4 develops machine learning models guided by classical representation theory and incorporating microstructural information. Finally Sec. 5 summarizes the report and briefly discusses late breaking developments.

## 1.1. Papers

The outcomes of this projects have been and will be documented in numerous peer-reviewed journal articles, as well as this report.

### *1.1.1. Published work*

- Rizzi, Francesco, Mohammad Khalil, Reese E. Jones, Jeremy A. Templeton, Jakob T. Ostien, and Brad L. Boyce. "Bayesian modeling of inconsistent plastic response due to

material variability." Computer Methods in Applied Mechanics and Engineering 353 (2019): 183-200 [1].

- Jones, Reese, Jeremy A. Templeton, Clay M. Sanders, and Jakob T. Ostien. "Machine learning models of plastic flow based on representation theory." Computer Modeling in Engineering and Sciences (2018): 309-342 [2].

- AL Frankel, RE Jones, C. Alleman, JA Templeton, Predicting the mechanical response of oligocrystals with deep learning, Computational Materials Science 169, 109099 (2019) [3].

- CC. Seepersad, C.C., J. Allison, A. Dressler, B. Boyce, D. Kovar, "An Experimental Approach for Enhancing the Predictability of Mechanical Properties of Additively Manufactured Architected Materials with Manufacturing-Induced Variability," accepted in Uncertainty Quantification in Multiscale Materials Modeling (D. McDowell and Y. Wang, Eds.), Elsevier, 2019.

- A.D. Dressler, E.W. Jost, J.C. Miers, D.G. Moore, C.C. Seepersad, B.L. Boyce, "Heterogeneities Dominate Mechanical Performance of Additively Manufactured Metal Lattice Struts", Additive Manufacturing, 2019.

- CC. Seepersad, C.C., J. Allison, A. Dressler, B. Boyce, D. Kovar, “An Experimental Approach for Enhancing the Predictability of Mechanical Properties of Additively Manufactured Architected Materials with Manufacturing-Induced Variability,” accepted for publication in Uncertainty Quantification in Multiscale Materials Modeling (D. McDowell and Y. Wang, Eds.), Elsevier, 2019.

- A.D. Dressler, E.W. Jost, J.C. Miers, D.G. Moore, C.C. Seepersad, B.L. Boyce, “Heterogeneities Dominate Mechanical Performance of Additively Manufactured Metal Lattice Struts”, Additive Manufacturing, 2019.

- S.L.B. Kramer, B.L. Boyce, A. Jones, A. Mostafa, B. Ravaji, T. Tancogne-Dejean, C.C. Roth, M.G. Bandpay, K. Pack, J.T. Foster, M. Behzadinasab, J.C. Sobotka, J.M. McFarland, J. Stein, A.D. Spear, P. Newell, M.W. Czabaj, B.W. Williams, C.H.M. Simha, M. Gesing, L.N. Gilkey, C.A. Jones, R. Dingreville, S.E. Sanborn, J.L. Bignell, A. Cerrone, V. Keim, A. Nonn, S. Cooreman, P. Thibaux, N. Ames, D.T. O’Connor, M.D. Parno, B. Davis, J. Tucker, B. Coudrillier, K.N. Karlson, J.T. Ostien, J.W. Foulk III, C.I. Hammetter, S. Grange, J.M. Emery, J.A. Brown, J.E. Bishop, K.L. Johnson, K.R. Ford, S. Brinckmann, M.K. Neilsen, J. Jackiewicz, K. Ravi-Chandar, T.A. Ivanoff, B.C. Salzbrenner, "The third Sandia Fracture Challenge: predictions of ductile fracture in additively manufactured metal", submitted to Int. J. Fracture, 2018.

- R. Banerjee, K. Sagiyama, G. H. Teichert and K. Garikipati, “A graph-theoretic framework for representation, exploration and analysis on computed states of physical systems”, Computer Methods in Applied Mechanics and Engineering, 351, 501-530, (2019)

### *1.1.2. In preparation or submitted papers*

- C. Alleman, A. Frankel, R. Jones, M. Khalil, “Analysis of evolving length-scales in crystal mechanics via autocorrelation”.
- C. Alleman, R. Jones, “Variability in Apparent Properties of Polycrystalline Materials”.
- A. Frankel, R. Jones, L. Swiler, "Gaussian process regression of hyperelastic constitutive relations".
- A. Frankel, R. Jones, "Prediction of stress states in plastic deformation of oligocrystals with deep learning".
- M. Khalil, G. H. Teichert, C. Alleman, N.M.Heckman, R. Jones, K. Garikipati, and B.L. Boyce. "Modeling strength and failure variability due to porosity in additively manufactured metals".
- K. Sagiyama and K. Garikipati “Machine learning materials physics: Deep neural networks trained on elastic free energy data from martensitic microstructures predict homogenized stress fields with high accuracy”, Preprint: arXiv.
- X. Zhang and K.I Garikipati, “Machine learning materials physics: Multi-resolution learning with convolutional and deep neural networks predicts the homogenized elastic response of materials with evolving microstructures".
- A.M. Roach, B. White, A. Garland, B.H. Jared, J.D. Carroll, B.L.Boyce, “Size-Dependent Stochastic Tensile Properties in Additively Manufactured 316L Stainless Steel" to be submitted to Additive Manufacturing.
- N.M. Heckman, H.J. Brown-Shacklee, T.A. Ivanoff, B.H. Jared, John Erickson, J.D. Madison, Reese Jones, B.L. Boyce, “Evolution and coalescence of void networks in additively manufactured stainless steel 316L”.
- Nathan M. Heckman, Thomas A. Ivanoff, Ashley M. Roach, Bradley H. Jared, Daniel J. Tung, Harlan J. Brown-Shaklee, Todd Huber, David J. Saiz, Josh R. Koepke, Jeffrey M. Rodelas, Jonathan D. Madison, Bradley C. Salzbrenner, Laura P. Swiler, Reese E. Jones, Brad L. Boyce, “Automated high-throughput tensile testing for process optimization and process-aware design”.

## 1.2. Presentations

- C. Alleman. Apparent anisotropy of cubic materials as a function of material and geometric length-scales, Conference on Computational Plasticity, Barcelona, (2019). Invited.
- C. Alleman. Variability in Apparent Properties of Polycrystalline Materials and its Effects on Uncertainty in Engineering Analysis, USNCCM, Austin, (2019). Invited.
- C. Alleman. Modeling the mechanical performance of AM stainless steels, SNL AM Workshop, Livermore, (2019). Invited.

- A. Frankel, "Predicting the mechanical response of oligocrystals with deep learning", MLUQ workshop, University of Southern California (2019).
- A. Frankel, "Predicting the mechanical response of oligocrystals with deep learning", 15th U.S. National Congress on Computational Mechanics in Austin, TX (2019).
- R. Jones. "Modeling material variability with uncertainty quantification and machine learning techniques", Mechanical engineering department seminar at University of Colorado in Boulder, CO (2019) Invited.
- R. Jones. "Designing neural network models of mechanical variability due to microstructural features", Mach Conference in Annapolis, MD (2019) Invited.
- R. Jones. "Modeling material variability with uncertainty quantification and machine learning techniques", International Conference on Multiscale Materials Modeling in Osaka, Japan (2018)
- M. Khalil. "Embedded Model Error and Bayesian Model Selection for Material Variability", SIAM Conference on Uncertainty Quantification, Orange Grove, CA, (2018).
- R. Jones. "Modeling material variability with uncertainty quantification and machine learning techniques", Keynote in World Congress on Computational Mechanics in New York, (2018). Invited.
- R. Jones. "Modeling material variability with uncertainty quantification and machine learning techniques", SIAM Conference on Mathematical Aspects of Materials Science in Portland, OR (2018). Invited.
- J. Templeton, "Neural Network Models of Multicrystalline Mechanical Behavior", ASC ML conference, Lawrence Livermore National Laboratory (2018).
- J. Templeton, "Neural Network Models of Multicrystalline Mechanical Behavior", Oak Ridge National Laboratory, (2018).
- J. Templeton, "Neural Network Models of Multicrystalline Mechanical Behavior", ASC Headquarters. (2018).
- C. Alleman, "Modeling Plasticity And Failure In Additively Manufactured Stainless Steel", Mach Conference in Annapolis, MD (2018)
- F. Rizzi, "Bayesian Methods to Capture Inherent Material Variability in Additively Manufactured Samples", 14th U.S. National Congress on Computational Mechanics in Montreal, Quebec, Canada (2017).
- R. Jones. "Modeling material variability with uncertainty quantification and machine learning techniques", Sandia National Laboratories, Albuquerque, NM (2017).
- K. Garikipati. Machine Learning Material Physics: A Data-driven Approach for Predicting Effective Material Properties in Multi-component Crystalline Solids. US National Congress of Computational Mechanics, in the minisymposium on Data-driven Modeling Using Uncertainty Quantification, Machine Learning and Optimization. Austin TX. (2019).

- K. Garikipati. Graph Theoretic Framework for Representation, Exploration and Analysis on Computed States of Physical Systems. Keynote at the US National Congress of Computational Mechanics, in the minisymposium on Data-driven Modeling Using Uncertainty Quantification, Machine Learning and Optimization. Austin (2019).
- K. Garikipati. Mechano-chemical phase transformations: Computational framework, machine learning studies and graph theoretic analysis, University of Southern California, (2019).
- B.L. Boyce, "Opportunities for high-throughput characterization", ADAPT Workshop, Colorado School of Mines, August, 2019.
- B.L. Boyce, "Mitigating rare defects in metal additive manufacturing", Gordon Research Conference on Heterogeneous Materials, Hong Kong, China, June, 2019.
- B.L. Boyce, S.L.B. Kramer, "The Sandia Fracture Challenge: Learning from Blind Benchmarks", VI International Conference on Computational Modeling of Fracture and Failure of Materials and Structures, Braunschweig, Germany, June 2019.
- B.L. Boyce, "Rare microstructural events limit the mechanical reliability of materials", Drexel University, Philadelphia, PA, April, 2019.
- B.L. Boyce "The promise and risk of metal 3D printing", Drexel workshop on Additive Manufacturing, April, 2019.
- B.L. Boyce "Rare microstructural events limit the mechanical reliability of materials", Graduate Student Enhancement Council, University of Texas at Austin, March, 2019.
- B.L. Boyce "Rare microstructural events limit the mechanical reliability of materials", University of California at Irvine, March, 2019.
- B.L. Boyce, "Lessons learned from the Sandia Fracture Challenges," Purdue Damage Workshop, West Lafayette, IN, February, 2019.
- B.L. Boyce "Rare microstructural events limit the mechanical reliability of materials", New Mexico Tech, Soccoro, NM, February, 2019.
- B.L. Boyce, "Rare microstructural events limit the mechanical reliability of materials", University of New Mexico Center for High Technology Materials, Albuquerque, NM, Nov 20, 2018.
- B.L. Boyce, "Rare microstructural events limit the mechanical reliability of materials", University of California at Berkeley Department of Materials Science and Engineering, Berkeley, CA, Nov 8, 2018.
- B.L. Boyce, "Stochastic performance of additively manufactured alloys", Michigan State University, May, 2018.
- B.L. Boyce, "Accelerating the process-structure-properties discovery cycle", TMS Annual Meeting, Phoenix, Arizona, February 2018.

- B.L. Boyce, “Rapid discovery of rare failure mechanisms”, International Conference on Plasticity, San Juan, Puerto Rico, January 2018.
- B.L. Boyce, “High-throughput testing reveals rare, catastrophic defects”, TMS Annual Meeting, March, 2017.
- B.L. Boyce, “High-throughput testing reveals rare, catastrophic defects”, University of California at Santa Barbara Materials Science and Engineering Department Seminar, October, 2016.

# 2. PHENOMENOLOGY

A significant amount of data is needed characterize distributions of uncertain material parameters. In this section we describe the high-throughput mechanical tests we employ, a novel *in situ* study of how visible and sub-threshold voids evolve with deformation, and an analysis of the length-scales in relevant microstructures and how they relate to homogenization and extracting a distribution of responses. The developing high-throughput characterization techniques will be documented elsewhere (see list of pending papers in Sec. 1).

## 2.1. High-throughput tension dogbones

The experiments of Boyce *et al.* [4] provide tensile stress-strain data quantifying the mechanical response up to failure (refer to Fig. 2-1) and corresponding computed tomography (CT) scans that reveal the internal porosity of the additively manufactured 17-4PH stainless steel dogbone specimens. One build provided 120 nominally identical replica dogbones with 1mm$\times$1mm$\times$4mm gauge sections, a subset of each build were imaged with CT prior to mechanical testing. For this study we examined 105 stress-strain curves and 18 CT scans from the same build.

All the tensile tests were performed at a $10^{-3}$/s strain rate effected by grips engaging the dovetail ends of the specimen seen in the inset of Fig. 2-1. Engineering stress was measured with a load cell, the cross-section measured by CT and optical techniques, and the strain was determined by digital image correlation (DIC) of the gauge section. Fig. 2-1 illustrates the ensemble of tensile tests which display minimal variation in their elastic response, moderate variability in their yield and hardening behavior, and wide variability in their failure characteristics. From these experimental stress-strain curves we extracted a number of features $\mathcal{F}$: the effective elastic modulus $\bar{E}$ from the initial slope, the yield strength $\sigma_Y$ from a 0.001 offset strain criterion, the yield strain $\varepsilon_Y$ from the strain corresponding to the yield stress, the ultimate tensile strength $\sigma_U$ from the maximum stress, the ultimate tensile strain $\varepsilon_U$ from the strain corresponding to the maximum stress, the failure strain $\varepsilon_f$ from maximum strain achieved, and the failure stress $\sigma_f$ stress corresponding to maximum strain. Model calibration described in Sec. 3.2.4 utilized this data (with the exception of $\bar{E}$ since it is highly correlated with $\sigma_Y/\varepsilon_Y$) which is summarized in Table 2-1. From Fig. 2-1 and Table 2-1 it is apparent that there is significant variability in the

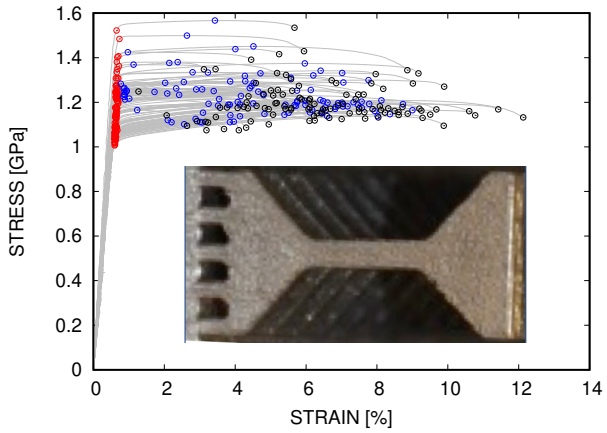


**Figure 2-1 Stress-strain response of dogbone specimens (inset). Features demarked with circles: yield (red), maximum/ultimate stress (blue), failure strain (black).**

| Parameter | | Min | Mean±deviation | Max |
|---|---|---|---|---|
| Elastic modulus (GPa) | $\bar{E}$ | 165.0 | 218.4 ± 22.5 (10.3%) | 277.8 |
| Yield strength (GPa) | $\sigma_Y$ | 1.02 | 1.17 ± 0.11 ( 9.8%) | 1.54 |
| Yield strain (%) | $\varepsilon_Y$ | 0.53 | 0.67 ± 0.08 (11.5%) | 0.93 |
| Ultimate tensile strength (GPa) | $\sigma_U$ | 1.10 | 1.23 ± 0.09 ( 7.0%) | 1.57 |
| Ultimate tensile strain (%) | $\varepsilon_U$ | 0.77 | 4.49 ± 2.24 (50.0%) | 9.00 |
| Failure strength (GPa) | $\sigma_f$ | 1.07 | 1.20 ± 0.08 ( 6.8%) | 1.53 |
| Failure strain (%) | $\varepsilon_f$ | 1.27 | 6.34 ± 2.14 (33.8%) | 12.13 |

**Table 2-1 Experimental response features $\mathcal{F}$ from 105 tensile tests of AM 17-4PH stainless steel tensile specimens.**

mechanical response, with strain-based features having greater variance than stress-based features due to the flatness of the post-yield stress curve.

The microstructural source of the variance in mechanical response was partially revealed by the CT of the 0.75mm×0.75mm×4mm interior of the gauge sections of some of the specimens. The CT scans were performed on each dogbone independently with 7.5 $\mu$m resolution, utilizing the same scan parameters. Identification of porous voxels was performed by applying a (per sample) threshold to the per-voxel CT intensity, and voids were identified by the spatial connectivity of porous voxels. The interior region of the samples appear to have a fairly homogeneous distribution of voids. However, post-fracture analysis shows that the specimens have a distinct surface crust which is approximately 0.05mm thick. Within the central CT scanned region, the void distribution appears to be isotropic, as the spatial correlations averaged across all samples in different directions through the cross-section. The mean porosity across all samples examined for this study was $\bar{\varphi} = 0.008$ and spatial correlation length was on the order of 50 $\mu$m. The average porosity varied sample to sample $\approx 60\%$ which is reflected in the $\approx 10\%$ variance of the effective elastic modulus $\bar{E}$ reported in Table 2-1.

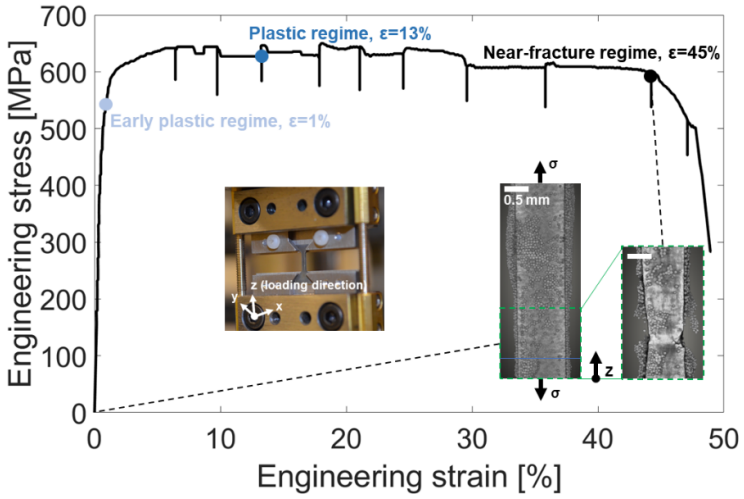


**Figure 2-2 Stress-strain curve of AM 316L tested in situ micro-CT test. Inset: an optical image of the mounted dogbone, and radiographs of the dogbone during testing (unloaded and post-necking state). The green box corresponds to the region of the micro-CT data analyzed.**

## 2.2. Evolution of void networks

The stress-strain data for the tensile test is illustrated in Fig. 2-2. The strengths and total elongation of the sample are within the range of values observed in high-throughput tensile tests on the same material [5], with yield and tensile strengths of 550 and 650 MPa, respectively, and a total elongation of 48%. Note that because tomographic scans tended to take on the order of hours, stress relaxation and load cell drift occurred during these periods, as seen in the vertical spikes in the stress-strain data. The inset dogbone images represented in Fig. 2-2 illustrate the region analyzed during deformation. The region of the inset outlined in green represents the specific region of interest that was compared at the early plastic (1% strain), plastic (13% strain), and near-fracture (45% strain) regimes. As seen in these images, the necking regime, which was also the site of fracture in the material, is contained within this regime. The normalized Z-position of fracture was determined to be ≈0.27.

The overall void evolution is presented in Fig. 2-3. The values for total porosity in Fig. 2-3a represent lower-bound values, as the minimum resolved pore size is ≈220 $\mu m^3$. The porosity tends to increase with increased sample strain, where the resolved porosity within the region of interest doubles between 1% and 13% strain, and exhibits a more than five-fold increase between 1% and 45% strain. The distribution chart indicates not only an increase in the total porosity, but also a general increase in the presence of larger voids at higher strains. While the distribution shapes are similar at 1% and 13% strain, a bimodal distribution is observed in the 45% strain sample. The cause for this is illustrated in the void maps presented in Fig. 2-3b: from 1% to 13% strain, there is a uniform increase in the number and size of voids throughout the sample. However, at 45% strain, the necking region shows a localized increase in void growth; the localized void growth at the neck is responsible for the bimodal void distribution. The normalized

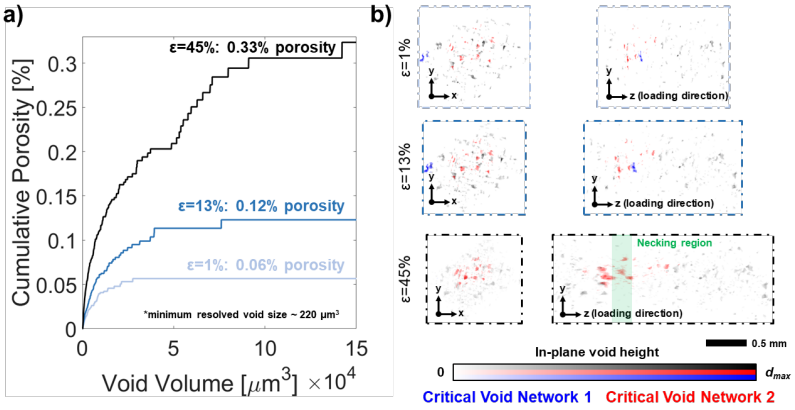


**Figure 2-3 (a) Cumulative porosity at each strain for the early plastic, plastic, and near-fracture regimes. These values correspond to the resolvable porosity measured by CT, which does not include any voids with a volume below 220 $\mu$m$^3$. (b) Void maps display the spatial evolution of porosity throughout deformation. The necking region is highlighted in green.**

void positions at all three strains of interest are presented in Fig. 2-4. The overlapping of voids at the three different strains indicates the effectiveness of the manual void selection and linear interpolation method used to correlate the position of voids at different strains. In the X-Y plane (orthogonal to the loading direction), the voids are relatively evenly distributed at all strains. In the Z-Y (transverse) plane, a clear localization is observed in the necking regime when the sample is at 45% strain. Void networks were generated based on these normalized void positions, generating a total of 443 void networks in the region of interest. Analysis of void evolution maps, which show the voids contained within a same network at all three strains, provides insight into the void-network based deformation mechanisms, and how these mechanisms contribute to overall fracture of the material.

### *2.2.1. Void correlation and void-network based deformation mechanisms*

Based on all of the void evolution maps analyzed in this study, a total of four primary void-network based deformation mechanisms were observed. The void network evolution maps presented in Fig. 2-5 illustrate each of these mechanisms, including void growth, void emergence, void coalescence, and free-surface absorption. Note, the void evolution maps display two-dimensional projections of the three-dimensional void data, where the intensity of the map corresponds to the in-plane depth, calculated as the sum of voxels contained within the void at each point. Each mechanism is described as follows: Void growth: As illustrated in Fig. 2-5a, voids grew in volume under sample deformation. In general, the direction of growth was largest along the tensile direction, where most voids at least doubled in size between 1% and 47% strain. The relatively large growth of voids (*e.g.* higher than the long-range sample strain) can be attributed to an enhancement in local plastic behavior due to high stress concentrations created by voids [6, 7]. This mechanism appears to be largely responsible for the significant increase in

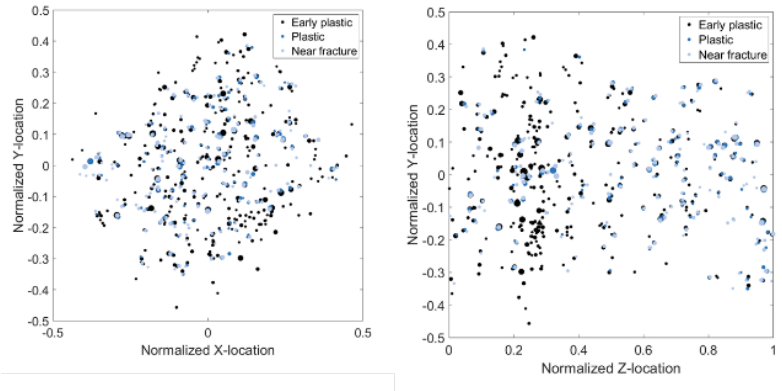


**Figure 2-4 Spatially correlated position of all voids at all strains. The diameter of each point is proportional to the equivalent spherical diameter of each void.**

overall porosity seen in Fig. 2-3. Void emergence: This mechanism, illustrated in Fig. 2-5b, represents when voids within the material become resolvable by micro-CT ($>$220 $\mu$m$^3$). This can occur from two underlying mechanisms, including the formation of new voids as well as the growth of previously unresolvable voids. Within the testing technique, the two mechanisms cannot be distinguished, and both are expected to occur. This mechanism is closely related to microvoid formation in the fracture of ductile materials [8, 9, 10], where defects can combine in areas of high local strains to form microvoids. The newly emerged voids tended to have relatively small volumes, with typical volumes below 103 $\mu$m$^3$, and were responsible for the increase in resolvable void quantity from 219 to 762, a $\approx$3.5x increase. Void coalescence: This mechanism, illustrated in Fig. 2-5c, represents when two initially separate voids combine to form a single void. This is similar to microvoid coalescence in ductile materials, where microvoids that have formed due to localized damage grow together, often to propagate a crack [8, 9]. This is different, however, in that while microvoid coalescence is often associated with failure, the coalescence of voids did not always lead to the detrimental failure in this study; instead, coalesced voids simply contributed to an increase in local damage. Void coalescence appeared to enhance the local void growth behavior, where the percentage volumetric growth in coalesced voids was higher than that of non-coalesced voids. Free-surface absorption: This mechanism, illustrated in Fig. 2-5d, indicates the consolidation of one or several voids and the free-surface of the material. The void evolution map alone cannot identify this mechanism, as after voids meet with the free surface, they are no longer classified as voids. By analyzing CT slices, however, one can see that a portion of the free-surface protrudes into the material with a shape reminiscent of the initial void. Similar to void emergence, voids displaying this deformation mechanism tended to show relatively large growth, and the free-surface of the material tended to show higher localized deformation in the vicinity of these voids. This is analogous to surface defects or cracks contributing to higher stress concentrations in fracture mechanics [11, 12]. These mechanisms serve as the basis for understanding how AM metals deform and fracture under uniaxial tension. In the following section, two void networks which are observed to be critical for material fracture are analyzed based on these mechanisms to understand how the mechanisms contribute to this specific sample's fracture.

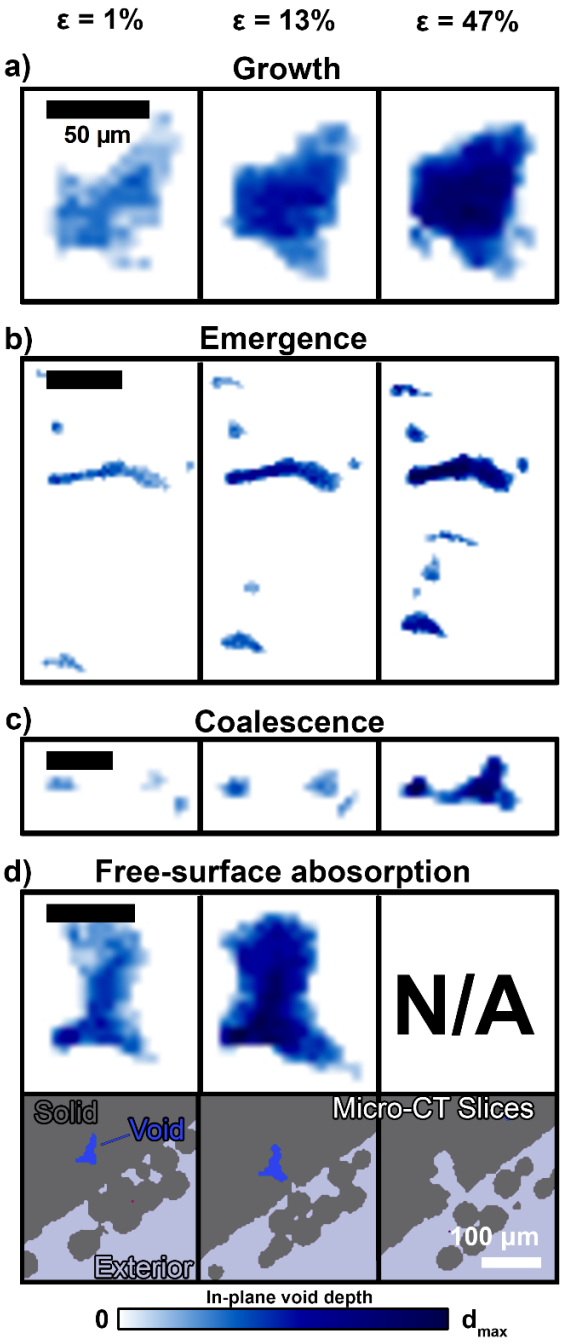


**Figure 2-5 Void network evolution maps illustrating the four primary void-network based deformation mechanisms: (a) void growth, (b) void emergence, (c) void coalescence, and (d) free-surface absorption. Note the micro-CT slices in (d) show the same region as the void evolution maps.**

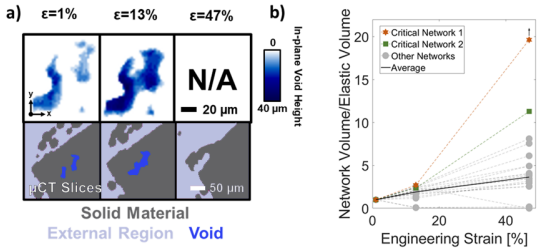


**Figure 2-6 (a) Void network evolution map of critical void network 1 showing void growth and emergence from 1% to 13% strain, and free surface absorption (coupled with micro-CT images) from 13% to 47% strain. (b) Relative change in volume compared to the early-plastic regime for all void-networks in the largest 10% of volumes; critical void network 1 and 2 show the highest relative growth.**

As indicated in Fig. 2-2, the sample was observed to fracture at a Z position of roughly 0.27 in the normalized coordinate system. Close to the fracture regime, two void networks were identified that seemingly dominated the void network-based deformation in this sample, termed “critical void” networks 1 and 2.

Critical void network 1 initially consists of a total of 3 voids close to the free surface of the material, illustrated in Fig. 2-6. Throughout deformation, the two largest voids within this network are seen to grow, coalesce, and eventually absorb into the free surface. The spatial location of this void network is illustrated in blue in Fig. 2-3b, where it can be seen that necking and fracture occur at the same normalized Z position as this network. As illustrated in Fig. 2-6b, this network showed the largest relative increase in volume between 1% and 13% strain, presumably due to the combination of deformation mechanisms. This trend continued at 45% strain, where the surface cavity created by this network was nearly 20x that of the initial void network volume. This cavity is expected to have contributed to a large localization in stress. Critical void network 2 represents the largest void network in the sample, centered roughly on the fracture plane of the material; the location is represented in red in Fig. 2-3. This void network, which is far from free-surfaces on the material and initially consists of many relatively close-packed voids, deforms through a combination of void growth, emergence, and coalescence. The amount of void emergence is roughly equivalent to that observed in the rest of the sample, with a ≈3.7x increase in the number of voids in this network. The void growth, however, is higher than that of other networks, with a more than tenfold increase in volume within this network, and an analogous increase of more than 12x for the largest void.

A combined analysis of these two critical networks provides a total description of failure within this dogbone. Because the two large voids in void network 1 were close to each other and the free surface, the growth of these voids was initially enhanced. These voids absorbed into the free surface, creating a large strain localization, and surface defect which enhances the effect of the localization. This localization enhances the deformation at this location (e.g. normalized Z-position of 0.27), and enhances the deformation of critical void network 2, a network of highly-connected voids centered at this same Z- position. The enhanced deformation appears to manifest primarily in the form of void growth in this regime, as void emergence is not

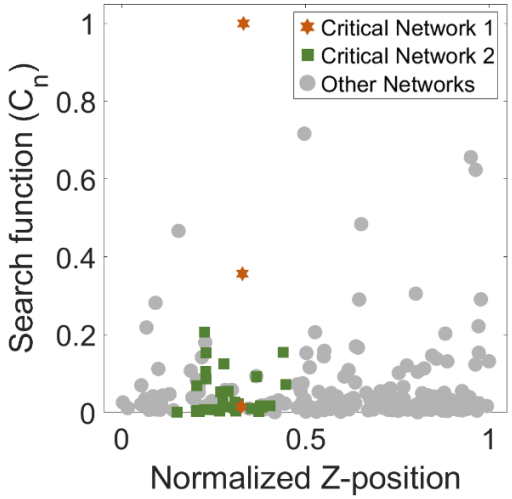


**Figure 2-7 Connectivity search function defined in Equation 2 at 1% strain**

substantially changed. The combined deformation of these two networks leads to the eventual failure of the material in this regime. While analysis of void network deformation lends to an understanding of the global deformation behavior within this specific sample, extrapolating this can provide some insight as to what void parameters may influence failure. We speculate as to how this may be utilized to predict material failure and potentially provide means to qualify porous AM parts.

### *2.2.2. Critical void parameters*

The basis for analyzing which void parameters contribute to part failure is based on work by Erickson and Spear, where a search function is utilized to identify spatial void relationships. In this model, they utilize a spatial radial distribution function to identify local connectivity of voids, predicting where failure will occur by identifying where this function is maximized within porous AM parts. Based on this concept, a global search function is defined which can include multiple parameters to identify potential regimes of failure within porous materials.. For our function, we assume that failure will originate from some void (n) and so the function is defined spatially at each void. The global search function, $C_n$ has the form:

$$C_n = \sum_m \prod_p f_p \tag{1}$$

where the indices $n$ and $m$ represent voids, where $n$ is the void being analyzed and $m$ is all other voids. The function $f_p$ represents a contributing factor to the search function, where each factor represents a physically informed scaling factor that ultimately contributes to the material failure, and the quotient of a finite set of $p$ factors is considered for each void. In the present study, empirical equations are utilized in each of the factors. However, as the understanding of plasticity within porous additively manufactured metals improves, plasticity models can help to inform more appropriate scaling factors. Analyzing the deformation mechanisms in this study reveals

several key concepts that should be represented in this function. Void Size: The increase in void volume throughout deformation is largely attributed to the growth of large voids, one of the four observed mechanisms. In general, larger voids were observed to have a larger increase in volume, such as the largest void in Critical void network 2, where the growth of just the largest void itself accounted for ≈5% of the change in porosity. Thus, we consider the first term to represent failure likely originating from a large void, with the following form for $C_1$, where ESD represents the equivalent spherical diameter of the void:

$$f_1 = \mathrm{ESD}_n \tag{2}$$

Distance to large voids: The proximity of voids to each other was observed to influence two of the deformation mechanism: emergence and coalescence. In general, the emergence of voids was seen when there were neighboring large voids, such as the example presented in Fig. 2-5b. In addition, the coalescence of voids was largely observed when there were two large voids in close proximity to each other, such as the example in Fig. 2-5c. This is not dissimilar to fracture in ductile materials, where the formation and growth of microvoids leads to their eventual coalescence which leads to crack formation [7, 8]. In this case, the close proximity of large voids can lead to stress concentrations which allow for this localized behavior to occur. To reflect the enhancement of localized damage due to large voids in close proximity to other large voids, we introduce the term $C_2$ based on the parameter used by Erickson and Spear where a radial distribution function is used to quantify void connectivity based on dn,m, the normalized distance between voids n and m, and the ESD of all other voids:

$$f_2 = \frac{\mathrm{ESD}_m}{\exp d_{n,m}^2} \tag{3}$$

Distance to free surface: The absorption of voids into the free surface was only observed in voids that were initially close to the free surface. Based on fracture mechanics, the voids close to the free surface enhance the stress concentration larger than those at the center of the sample, and create an even larger stress concentration once they are part of the free surface [11, 12]. Due to this, it is critical to weight voids which are closer to the surface more than those closer to the center. For simplicity, this is done using a normalized linear function, with a maximum value for voids on the surface, and minimum for voids at the center of the sample; this value, $C_3$, has the following form:

$$f_3 = 1 - d_{m,surf} \tag{4}$$

where $d_{m,surf}$is the normalized distance of the void to the surface, ranging from 0 to 1. In this study, these combined functions serve primarily as a search function, identifying regions within the material where there are large voids close to both the free surface and other large voids. A normalized plot of the search function at 1% strain is illustrated in Fig. 2-7. The function is maximum at one of the voids in critical void network 1 and is consistent with the location of fracture. This supports the premise that the size, location, and distance to neighboring voids contribute to the stress localization caused by this void network. Using this search function, the voids in critical void network 2 show relatively high values in the same spatial region as critical void network 1, indicating their high connectivity. The preference of these voids to grow into a largely connected network under tensile deformation is seemingly governed by this initial connectivity of voids. While the global search function as applied in this study serves well to

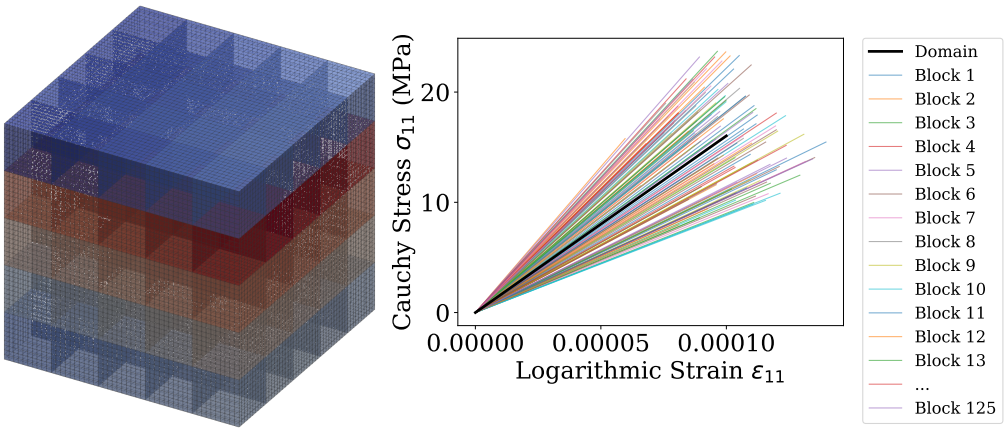


**Figure 2-8 The grainwise response of a polycrystalline aggregate under uniaxial-stress elastic loading. Left: the grain morphology of the aggregate, colored by grain ID. Right: the stress-strain curves from each grain.**

identify regions within the material where there are large voids that are simultaneously close to other large voids and close to the free surface, the equation used does not necessarily represent the quantitative deformation behavior within the material. Future studies may consider a more numerical understanding of how void-network based mechanisms contribute to localized damage and ultimately failure within AM metals. These equations may be largely material dependent, however, as for perfectly brittle materials, the elastic contributions of void networks should be dominating, and for plastic materials (such as in this study), the relationships governed by the plastic deformation mechanisms will be more controlling. In addition, the list of parameters discussed in this manuscript include only those directly related to the mechanisms observed in this study and is not exhaustive. Factors such as void roughness, aspect ratio, surrounding grain structure, etc. are all expected to have non-negligible contributions to damage evolution of voids. In addition, surface roughness has been speculated to play a large role in the mechanical behavior of AM metals with similar geometries to that used in this study [13].

## 2.3. Homogenization and asymptotic response of microstructure

The unit of study in this section is an idealization of polycrystalline microstructure such as that shown in Fig. 2-8. Two simplifications are made in the proceeding analysis. First, the sub-grain response is ignored, so that the micromechanical calculations are based on grain averages. Second, the microstructure is idealized as a collection of cube-shaped grains to simplify some parts of the calculation. For example, the permutations of a set of cube-shaped grains are finite in number, whereas general grain morphologies do not admit finite permutations of the orientations.

Consider a spatially-varying material property $0 < P(\boldsymbol{x}) < \infty$. The cumulative distribution function (CDF) $F_P(p)$ gives the probability that the property $P$ measured at a material point $\boldsymbol{x}$ is less than or equal to a value $p$. Now, consider a material sample with $P(\boldsymbol{x})$ drawn independently

for each $\boldsymbol{x}$ from the distribution $\mathcal{D}_P$ with CDF $F_P$. For a continuum with $P(\boldsymbol{x})$ independent of $P(\boldsymbol{x}')$ for all $x' \neq x$, there are uncountably infinitely many arrangements of $P(\boldsymbol{x})$ that satisfy the same sample distribution. For practical scenarios, there is usually a limit to this continuum definition of $P$, so that it may only be meaningful to examine a finite set of arrangements. For example, the definition of a material property may have a lower limit $v$ on the volume of material that may be considered to exhibit that property. In this case, for a body with volume $V = n \cdot v$, there are $n!$ permutations of the field $P(\boldsymbol{x})$ that have the same sample distribution. For many homogenization techniques, the input data is just the sample distribution, and information about the spatial arrangement is discarded. For this reason, the analysis below considers separately the *bias* error due to model lack-of-fit and the *irreducible* error that derives from spatial arrangement for some idealized cases. Of course, homogenization techniques can include input data related to spatial arrangement, but wherever a reduced-order model is employed, some version of this concern remains.

The analysis of convergence of apparent to effective properties focuses on the scaling of the variance over sets $\mathcal{S}^{\text{eqv}}$ of statistically-equivalent spatial arrangements $\sigma_P^2(l)$ as a function of a material lengthscale $l$. The existence of a representative volume element (RVE) for a property $P$ thus requires the following conditions be met as $l \to \infty$:

1. The apparent property $P^{\text{app}}(l)$ goes to the effective property $P^{\text{eff}}$ which is equal to the expectation of $P$ over $\mathcal{S}^{\text{eqv}}$, which must be finite.
2. The variance $\sigma_P^2$ over $\mathcal{S}^{\text{eqv}}$ goes to 0.

The RVE length $l_P^{\text{RVE}}(\delta)$ is then defined such that for $\delta > 0$,

$$l > l_P^{\text{RVE}}(\delta) \to \sigma_P^2(l) < \delta \tag{5}$$

This definition of RVE differs significantly from those previously put forward in the literature. First, the proposed definition does not mention the idea that the response of the RVE should be representative of the entire body. Although this seems like a deviation from the original intent of the RVE concept, meaningful definition of the response of the entire body is only possible in general for macroscopically homogeneous materials. In place of this overly restrictive condition, the proposed definition naturally allows for variation in material properties in a given body and allows for comparison of $l_P^{\text{RVE}}$ and gradient lengths of $l_P^{\nabla}$ for that body. This type of comparison enables a determination of the conformity of a particular specimen to RVE assumptions and thus determines the appropriateness of a homogenized constitutive law. For example, we can find a $\delta(l)$, for $l > 0$ such that

$$l' > l \to \sigma_P^2(l') < \delta(l) \tag{6}$$

If the function $\sigma_P^2(l)$ is strictly decreasing, $\delta(l)$ can be taken simply as the inverse of $l_P^{\text{RVE}}$. Otherwise, we can make $\delta(l)$ take on unique values by finding the minimum $\delta$ for a given $l$. This allows the extension of (5) to cover practical cases where $l$ is dictated by computational limitations or limited by $l_P^{\nabla}$. Essentially, (5) and (6) define an RVE subject to a limit on uncertainty on the one hand, and quantify the uncertainty in an RVE representation at a given lengthscale. We then do not require a monolithic interpretation of what it is to be representative; instead, we can quantify *how* representative a given volume element is. Of course, we can

arbitrarily choose a $\delta$ and rigidly define an RVE length, but we must recognize some degree of arbitrariness in this choice.

The second conceptual deviation in the proposed definition is in the insertion of the homogenization method into the definition of the RVE via the sets $\mathcal{S}^{\text{eqv}}$. Under the proposed definition, homogenization procedures which require different input data may give rise to different $\mathcal{S}^{\text{eqv}}$, and in turn different $l_P^{\text{RVE}}$. This effectively makes the RVE a property of the material constitutive response and homogenization technique rather than the material itself. Again, this may seem to be outside the spirit of the original conception of the RVE, but it endows a mathematical rigor and generality that is absent when conceiving of a RVE for so-called "material behavior" that is conceptually independent of any constitutive law. Given that RVEs are almost exclusively used for the mathematical analysis of the application of homogenized constitutive laws, it is appropriate to trade the vaguer but perhaps more intuitively satisfying original definition for the more rigorous and more easily applied proposed definition. For example, given a particular constitutive law, homogenization procedure, and degree of uncertainty, we can say quantitatively whether the RVE concept is feasible for a given instance of the material by comparing $l_P^{\text{RVE}}$ and $l_P^{\nabla}$. This extends the concept of scale separation from the asymptotic regime to apply to any scenario where the aforementioned quantities can be calculated in a meaningful way.

The detailed implications of the RVE definition above are explored below for some idealized cases. Of course, more realistic cases may elude the full analysis suggested above, but it will be shown that more realistic cases can be analyzed within the context of the idealized results in order to provide meaningful situation.

### *2.3.1. Apparent elastic moduli*

The first material properties to be considered here are the elastic moduli. Specifically, we compute the apparent (anisotropic) elastic moduli of some idealized microstructures and analyze the convergence of these values to effective moduli. We use the stainless steel constants in [14] as an example.

We consider a single set of $m$ rotations, where $m$ is a perfect cube. An ensemble of $n$ sets of rotations is then considered, where each set of rotations is denoted $R_i$ with $i = 1, \ldots, n$. For the techniques considered here, statistically equivalent sets $\mathcal{S}_i^{\text{eqv}}$ of spatial arrangement can be created as follows. Each set of rotations $R_i$ can be assigned in $m!$ ways to a unit cube microstructure with grain size $d = m^{-1/3}$. Each such spatial arrangement is denoted $S_{ij} \in \mathcal{S}_i^{\text{eqv}}$ with $j = 1, \ldots, m$. For each $S_{ij}$, the elastic modulus is computed via finite element approximation.

As an example, the sample cumulative distribution function (CDF) for $R_1$ with $m = 2000$ is shown in Fig. 2-9. For plotting purposes, the theoretical minimum and maximum single crystal moduli are appended to the sample and assigned cumulative probabilities of 0 and 1, respectively. Taking $n = 100$, a set of samples are generated, and the CDFs are shown in Fig. 2-10. Again, the standard estimates for apparent elastic moduli ignore spatial arrangement, so that there is a single set of estimates for each $R_i$. Typically, analyses of the effectiveness of these estimates conflate the

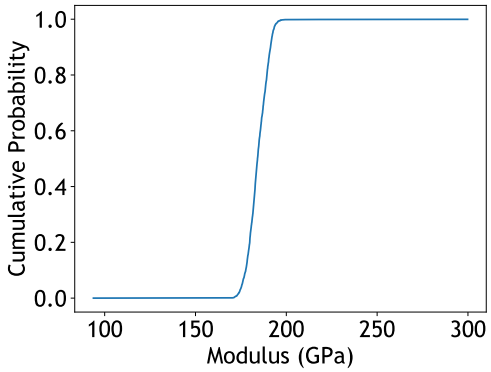


**Figure 2-9 CDF of computed elastic modulus $E_x$ for idealized eight-grain microstructures $S_{1j}$ with rotations $R_1$.**

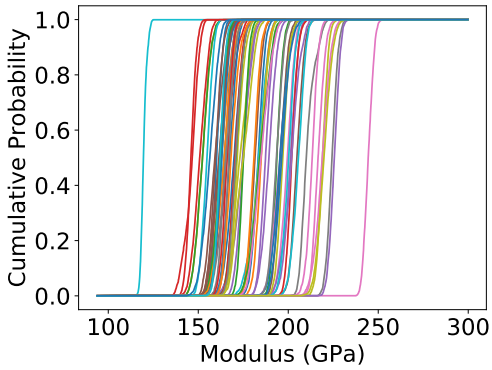


**Figure 2-10 CDFs of computed elastic modulus $E_x$ for idealized eight-grain microstructures $S_{ij}$ with rotations $R_i$.**

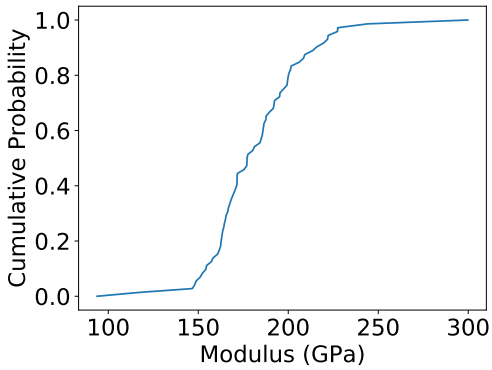


**Figure 2-11 CDF of computed elastic modulus $E_x$ for idealized eight-grain microstructures $S_{ij}$ with combined orientation and arrangement sampling.**

effects of variability due to sampling rotations and the variability due to sampling spatial arrangements. Here, these effects are considered separately.

First, consider the typical method of sampling, which returns $n$ sets of rotations, each in a particular spatial arrangement. This corresponds to sampling over $P \sim \mathcal{U}(1,m)$ and returning $S_{iP_i}$ for each $i = 1,\ldots,n$. The CDF for such a sample is shown in Fig. 2-11. In order to produce statistical data on apparent modulus, and in fact, to provide a solution to the problem of what to predict as the moduli for a given microstructure, it is necessary to introduce a framework for such calculations. For this study, some of the methods commonly available in the literature are employed. A summary follows.

### *2.3.2. Approximation of the apparent elastic tensor*

In a region $k$ of a composite material, the elastic constitutive relation is given by

$$\boldsymbol{T}_k^* = \mathbb{L}_k : \boldsymbol{E}_k^e \tag{7}$$

If the volume fraction of region $k$ is $c_k$, the average elastic strain in the body is

$$\bar{\boldsymbol{E}}^e = \sum_{k=1}^{N} c_k \boldsymbol{E}_k^e \tag{8}$$

The average stress is likewise

$$\bar{\boldsymbol{T}}^* = \sum_{k=1}^{N} c_k \boldsymbol{T}_k^* = \sum_{k=1}^{N} c_k \mathbb{L}_k : \boldsymbol{E}_k^e \tag{9}$$

We postulate the existence of concentration tensors $\mathbb{A}_k$ such that

$$\bar{\boldsymbol{E}}_k^e = \mathbb{A}_k : \bar{\boldsymbol{E}}^e \tag{10}$$

Combining (9) and (10),

$$\bar{\boldsymbol{T}}^* = \sum_{k=1}^{N} c_k \bar{\boldsymbol{T}}_k^* = \left( \sum_{k=1}^{N} c_k \mathbb{L}_k : \mathbb{A}_k \right) : \bar{\boldsymbol{E}}^e \tag{11}$$

Following (11), we define

$$\mathbb{L}_{\text{eff}} = \sum_{k=1}^{N} c_k \mathbb{L}_k \mathbb{A}_k \tag{12}$$

so that

$$\bar{\boldsymbol{T}}^* = \mathbb{L}_{\text{eff}} : \bar{\boldsymbol{E}}^e \tag{13}$$

From the case where the material properties are uniform, we derive the constraint

$$\mathbb{I} = \sum_{k=1}^{N} c_k \mathbb{A}_k \tag{14}$$

Given the equivalence

$$\mathbb{L}_k : \left( \bar{\boldsymbol{E}}^e + \tilde{\boldsymbol{E}}^e \right) = \mathbb{L}_{\text{ref}} : \left( \bar{\boldsymbol{E}}^e + \tilde{\boldsymbol{E}}^e - \boldsymbol{\Lambda}_k \right) \tag{15}$$

We postulate the existence of the Eshelby tensor $\mathbb{S}_k$ [15], such that

$$\tilde{\boldsymbol{E}}^e = \mathbb{S}_k : \boldsymbol{\Lambda}_k \tag{16}$$

From (15) and (16),

$$\begin{aligned}
\mathbb{L}_k : \left( \bar{\boldsymbol{E}}^e + \mathbb{S}_k : \boldsymbol{\Lambda}_k \right) &= \mathbb{L}_{\text{ref}} : \left[ \bar{\boldsymbol{E}}^e + (\mathbb{S}_k - \mathbb{I}) : \boldsymbol{\Lambda}_k \right] \\
(\mathbb{L}_k - \mathbb{L}_{\text{ref}}) : \bar{\boldsymbol{E}}^e &= [\mathbb{L}_{\text{ref}} : (\mathbb{S}_k - \mathbb{I}) - \mathbb{L}_k : \mathbb{S}_k] : \boldsymbol{\Lambda}_k \\
\left( \mathbb{L}_{\text{ref}}^{-1} : \mathbb{L}_k - \mathbb{I} \right) : \bar{\boldsymbol{E}}^e &= \left[ \mathbb{I} : (\mathbb{S}_k - \mathbb{I}) - \mathbb{L}_{\text{ref}}^{-1} : \mathbb{L}_k : \mathbb{S}_k \right] : \boldsymbol{\Lambda}_k \\
\left( \mathbb{L}_{\text{ref}}^{-1} : \mathbb{L}_k - \mathbb{I} \right) : \bar{\boldsymbol{E}}^e &= \left[ \mathbb{I} - \left( \mathbb{L}_{\text{ref}}^{-1} : \mathbb{L}_k - \mathbb{I} \right) : \mathbb{S}_k \right] : \boldsymbol{\Lambda}_k \\
\bar{\boldsymbol{E}}^e &= \left[ \left( \mathbb{L}_{\text{ref}}^{-1} : \mathbb{L}_k - \mathbb{I} \right)^{-1} - \mathbb{S}_k \right] : \boldsymbol{\Lambda}_k
\end{aligned} \tag{17}$$

We define the interaction tensor $\mathbb{T}_k$ such that

$$\boldsymbol{E}_r^e = \bar{\boldsymbol{E}}^e + \tilde{\boldsymbol{E}}^e = \mathbb{T}_k : \bar{\boldsymbol{E}}_{\text{ref}}^e \tag{18}$$

Then from (17) and (18),

$$\mathbb{T}_k = \left[ \mathbb{I} + \mathbb{S}_k : \mathbb{L}_{\text{ref}}^{-1} : (\mathbb{L}_k - \mathbb{L}_{\text{ref}}) \right]^{-1} \tag{19}$$

A class of approximations use the Eshelby tensor $\mathbb{S}$ to derive an interaction tensor $\mathbb{A}$ that produces an effective elasticity tensor. The dilute approximation that each phase is an isolated inhomogeneity, so that the reference strain is approximately equal to the average strain in the body $\bar{\boldsymbol{E}}^e$. Then, comparing Equations (10) and (18),

$$\mathbb{A}_k^{\text{dilute}} = \mathbb{T}_k \tag{20}$$

The *Mori-Tanaka* approximation [16] assumes that the reference strain $\bar{\boldsymbol{E}}^e$ is approximately equal to the (uniform) strain $\bar{\boldsymbol{E}}^e_0$ in the *matrix* phase $(r = 0)$, so that

$$\boldsymbol{E}^e_k = \mathbb{T}_k : \bar{\boldsymbol{E}}^e_0 \tag{21}$$

Then

$$\bar{\boldsymbol{E}}^e = \sum_{k=1}^{N} c_k \boldsymbol{E}^e_k = \sum_{k=1}^{N} c_k \mathbb{T}_k : \bar{\boldsymbol{E}}^e_0 \tag{22}$$

Combining (21) and (22),

$$\boldsymbol{E}^e_k = \mathbb{T}_k : \left( \sum_{k=1}^{N} c_k \mathbb{T}_k \right)^{-1} : \bar{\boldsymbol{E}}^e \tag{23}$$

That is,

$$\mathbb{A}^{\mathrm{mt}}_k = \mathbb{T}_k : \left( \sum_{k=1}^{N} c_k \mathbb{T}_k \right)^{-1} \tag{24}$$

The *self-consistent* approximation [17] assumes

$$\mathbb{L}_{\mathrm{ref}} = \mathbb{L}_{\mathrm{eff}} \tag{25}$$

$$\bar{\boldsymbol{E}}^e_{\mathrm{ref}} = \bar{\boldsymbol{E}}^e \tag{26}$$

so that

$$\mathbb{A}^{\mathrm{sc}}_k = \left[ \mathbb{I} + \bar{\mathbb{S}}_k : \left( \bar{\mathbb{L}}^{-1} : \mathbb{L}_k - \mathbb{I} \right) \right]^{-1} \tag{27}$$

where $\bar{\mathbb{S}}_k$ is constructed using $\bar{\mathbb{L}}$.

In Equation (12), the index $i$ ranges over the phases, from 0 for the matrix, and through $1, \ldots, N$ for $N$ inhomogeneities. Then $c_i$ is the volume fraction of the inhomogeneity $i$, while $\mathbb{L}_i$ is the elasticity tensor, and $\mathbb{A}_i$ is the interaction tensor. The $\mathbb{A}_i$ are constrained so that

$$\sum_{i=0}^{N} c_i \mathbb{L}_i \mathbb{A}_i = \mathbb{I} \tag{28}$$

Given (28), the interaction tensor for the matrix can be determined a priori as

$$\mathbb{A}_0 = \frac{1}{c_0} \left( \mathbb{I} - \sum_{i=1}^{N} c_i \mathbb{L}_i \mathbb{A}_i \right) \tag{29}$$

We consider four estimates of the apparent elastic moduli:

1. The *isostrain* estimate (Voigt bound [18]).

$$\boldsymbol{\sigma}(\boldsymbol{x}) = \mathbb{C}(\boldsymbol{x}) : \langle \boldsymbol{\varepsilon} \rangle \tag{30}$$

$$\mathbb{C}^{\mathrm{app}}_{\mathrm{V}} = \frac{1}{V} \sum_{i=1}^{8} v_i \mathbb{C}_i \tag{31}$$

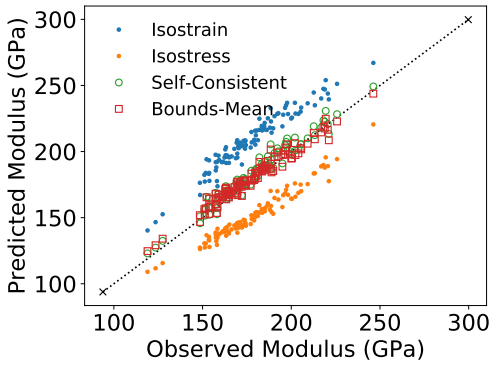


**Figure 2-12 Predictions of apparent moduli from the four methods detailed in Eqs** (31)**-**(35)**.**

2. The *isostress* estimate (Reuss bound [19]).

$$\boldsymbol{\varepsilon}(\boldsymbol{x}) = \mathbb{C}^{-1}(\boldsymbol{x}) : \langle \boldsymbol{\sigma} \rangle \tag{32}$$

$$\mathbb{C}_{\mathrm{R}}^{\mathrm{app}} = \left( \frac{1}{V} \sum_{i=1}^{8} v_i \mathbb{C}_i^{-1} \right)^{-1} \tag{33}$$

3. The *bounds-mean* estimate (Hill average [20]).

$$\mathbb{C}_{\mathrm{BM}}^{\mathrm{app}} = \frac{1}{2} \left( \mathbb{C}_{\mathrm{V}}^{\mathrm{app}} + \mathbb{C}_{\mathrm{R}}^{\mathrm{app}} \right) \tag{34}$$

4. The *self-consistent* estimate [17].

$$\begin{aligned} \mathbb{C}_{\mathrm{SC}}^{\mathrm{app}} &= \sum_{i=1}^{8} v_i \mathbb{C}_i : \mathbb{A}_i \\ &= \sum_{i=1}^{8} v_i \mathbb{C}_i : \left\{ \mathbb{I} + \mathbb{S}\left(\mathbb{C}_{\mathrm{SC}}^{\mathrm{app}}\right) : \left[ \left(\mathbb{C}_{\mathrm{SC}}^{\mathrm{app}}\right)^{-1} : \mathbb{C}_i - \mathbb{I} \right] \right\}^{-1} \end{aligned} \tag{35}$$

Here, $\mathbb{C}_{\mathrm{XX}}^{\mathrm{app}}$ are the estimated apparent elastic tensors, and $\mathbb{S}(\mathbb{C})$ is the Eshelby tensor [15] for a medium with elastic tensor $\mathbb{C}$. For the ensemble with sample distribution shown in Fig. 2-11, the predictions of apparent modulus are shown in Fig. 2-12. It is immediately obvious from Fig. 2-12 that there is significant variability in the quality of the predictions. This is even true for a particular observed modulus. That is to say, there are multiple microstructures that have the same apparent modulus and which yield different predictions for apparent modulus.

The limiting case is for a single crystal. First, it is recognized that any observed modulus between the minimum and maximum single crystal moduli can be observed for a single crystal of some orientation. This result is due to the smoothness of single crystal modulus as a function of orientation and the intermediate value theorem. The variation in single crystal elastic modulus across orientation space is depicted in Fig. 2-13, where the smooth, nonlinear variation is evident.

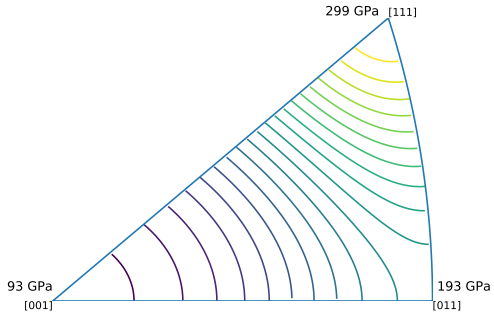


**Figure 2-13 Variation in elastic modulus $E_{xx}$ over the standard triangle. The [001], [011], and [111] moduli are shown on the figure. Contours represent 10 GPa steps.**

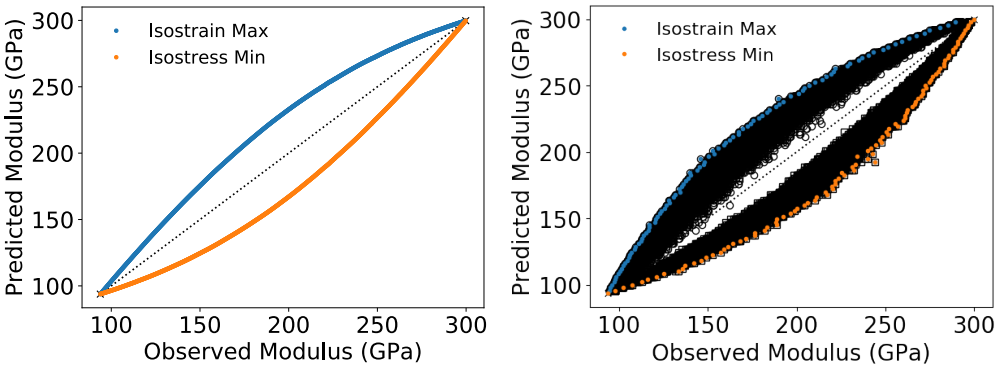


**Figure 2-14 Maximum isostrain and minimum isostress predictions of apparent moduli across the range of potentially observable moduli. Left: Approximation of observed modulus via** (34)**. Right: DNS calculation of observed modulus.**

There, it can be clearly seen that intermediate values of modulus can be obtained, for example, by traversing the arc from the [001] orientation to the [111] orientation.

The next noteworthy point is that the error in the approximation made here is finite. This is guaranteed to be true due to the finite positive values taken on by the moduli. For the isostrain and isostress approximations, the arithmetic and harmonic means respectively ensure finiteness in the approximations. For the self-consistent approach, the key ingredient is the fact that $\sum_{i=1}^{8} v_i \mathbb{A}_i = \mathbb{I}$ by construction. More precise bounds are investigated here numerically, where the maximum upper bound and minimum lower bounds are shown in Fig. 2-14.

The approximation to the extremal bounds is computed by constructing an ensemble of 100 eight-grain microstructures for each target observed modulus and returning the maximum and minimum approximations. Each of the 100 samples corresponds to solving an unconstrained optimization to determine the set of eight rotations that will produce the target modulus, approximated by the bounds-mean computed for that set of rotations. Since this solution is generally non-unique, repeating this process with a randomly seeded initial guess produces a

population of samples with potentially different isostrain and isostress approximations. The solutions are then simulated to compute the observed modulus, which deviates from the predicted value by a maximum of around 25%. The result is the slightly asymmetric lenticular-shaped region shown in Fig. 2-14.

The maximum and minimum bounds converge to the maximum and minimum single crystal moduli at the endpoints of the range, where the isostress and isostrain conditions are identical. Thus, the potentially observable polycrystal moduli are bounded above and below by the maximum and minimum single crystal moduli.

For each modulus $y_{ij}$, take the self-consistent estimate $x_i$ as a model, and consider

$$\begin{aligned} y_{ij} =& ax_i + b + \varepsilon_{ij} \\ =& \hat{y}_i + \varepsilon_{ij} \end{aligned} \tag{36}$$

$a$ and $b$ are determined from linear regression, and where $\varepsilon_{ij}$ is the error associated with the estimate. The sum of squared errors, $\varepsilon^2$ is then a useful measure of the effectiveness of the model, and the coefficient of determination $R^2$ can be defined in terms of $\varepsilon^2$ as

$$R^2 = 1 - \frac{\varepsilon^2}{\sum_{i=1}^{n} (y_{iP_i} - \bar{y})^2} \tag{37}$$

where $\bar{y}$ is the average over spatial arrangements $S_{iP_i}$ for and corresponding rotations $R_i$. For the sample shown in Fig. 2-11, $R^2 \approx 0.962$. However, some of the error is coming from a deficiency in the fit, and some of the error is coming from the inherent uncertainty in the modulus due to variability arising from the spatial arrangement of a given set of rotations. To get at the latter source, consider the following partition of $\varepsilon^2$, with $\bar{y}_i$ as the mean over spatial arrangements $S_{ij}$ for a given set of rotations $R_i$:

$$\varepsilon^2 = \sum_{i=1}^{n} \sum_{j=1}^{m} (y_{ij} - \bar{y}_i)^2 + \sum_{i=1}^{n} (\bar{y}_i - \hat{y}_i)^2 \tag{38}$$

Here, the first summand is the *pure* error due in this case to spatial-arrangement induced variability, and the second is the *lack of fit* error. The expected value of $\varepsilon^2$ is then decomposed as

$$\begin{aligned} E[\varepsilon^2] =& E\left[\sum_{i=1}^{n} \sum_{j=1}^{m} (y_{ij} - \bar{y}_i)^2\right] + E\left[\sum_{i=1}^{n} (\bar{y}_i - \hat{y}_i)^2\right] \\ =& \sum_{i=1}^{n} E\left[\sum_{j=1}^{m} (y_{ij} - \bar{y}_i)^2\right] + E\left[\sum_{i=1}^{n} (\bar{y}_i - \hat{y}_i)^2\right] \\ =& m \sum_{i=1}^{n} s_i^2 + E\left[\sum_{i=1}^{n} (\bar{y}_i - \hat{y}_i)^2\right] \end{aligned} \tag{39}$$

where $s_i^2$ is the sample variance over spatial arrangements $S_{ij}$ of a given set of rotations $R_i$. Taking $m = 1$,

$$E[\varepsilon^2] = \sum_{i=1}^{n} s_i^2 + E\left[\sum_{i=1}^{n} (\bar{y}_i - \hat{y}_i)^2\right] \tag{40}$$

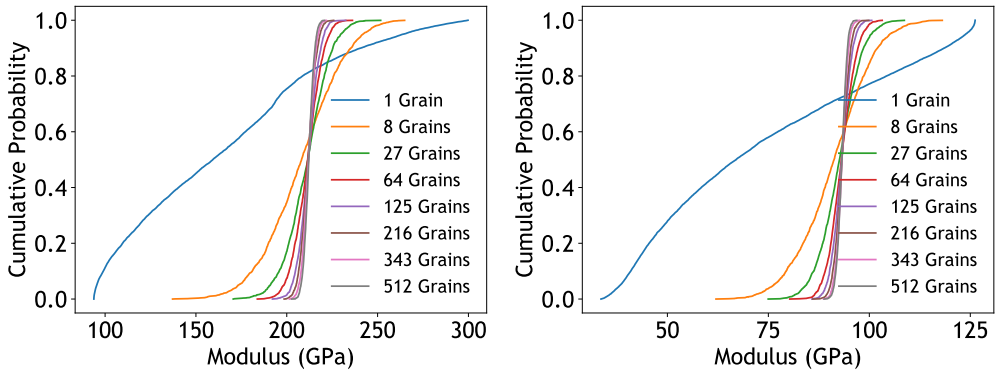


**Figure 2-15 CDFs of isostrain-estimated elastic moduli (Left: xx, Right: xy) for idealized microstructures with varying numbers of grains.**

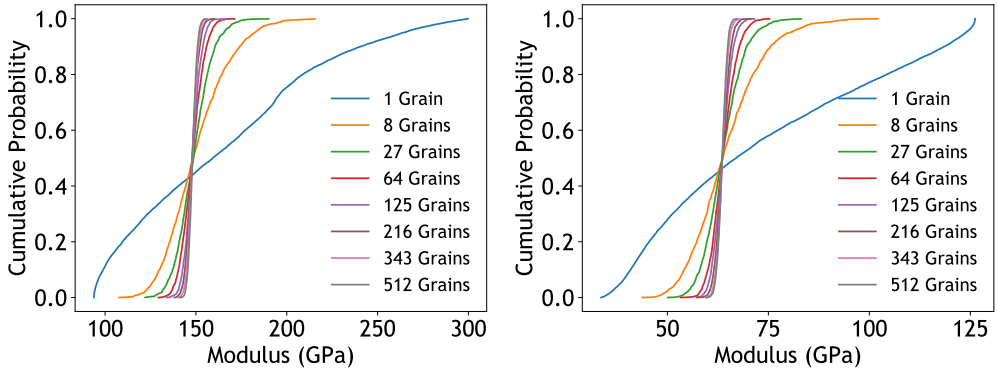


**Figure 2-16 CDFs of isostress-estimated elastic moduli (Left: xx, Right: xy) for idealized microstructures with varying numbers of grains.**

It is clear that the model which minimizes the lack of fit error is $\hat{y}_i := \bar{y}_i$, in which case

$$E[\varepsilon^2] = \sum_{i=1}^{n} s_i^2 \tag{41}$$

Now define an error measure $e$, which estimates the lack of fit error, as

$$e := \varepsilon^2 - \sum_{i=1}^{n} s_i^2 \tag{42}$$

so that

$$E[e] = E\left[\sum_{i=1}^{n} (y_i - \hat{y}_i)^2\right] \tag{43}$$

With the preceding analysis, there is an estimation in hand of the aggregate elastic properties derived directly from the microstructure and analysis of the variability to be expected from sample to sample as a function of the number of constituents in the aggregate. Implicit in this is

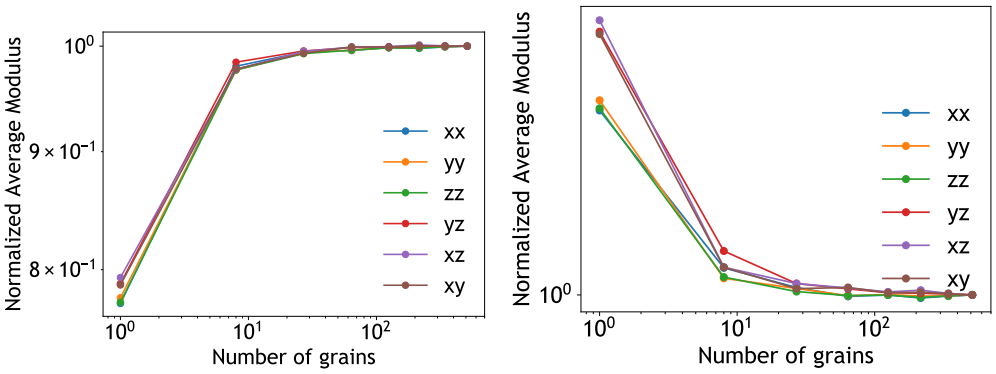


**Figure 2-17 Convergence of averages of isostrain-estimated (Left) and isostress-estimated (Right) moduli with increasing numbers of grains.**

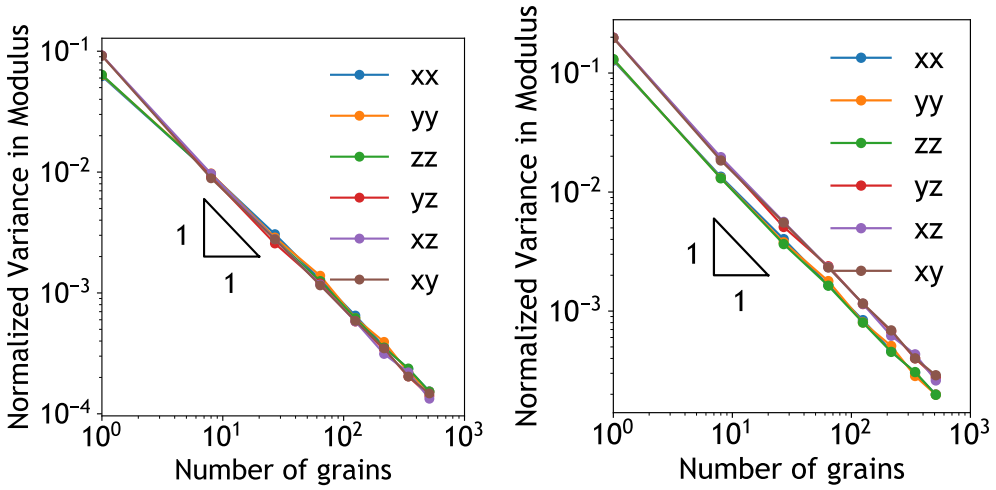


**Figure 2-18 Normalized variances of isostrain-estimated (Left) and isostress-estimated (Right) moduli as a function of number of grains.**

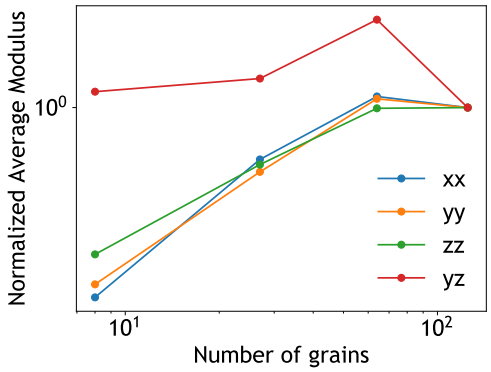


**Figure 2-19 Convergence of averages of DNS-computed moduli with increasing numbers of grains.**

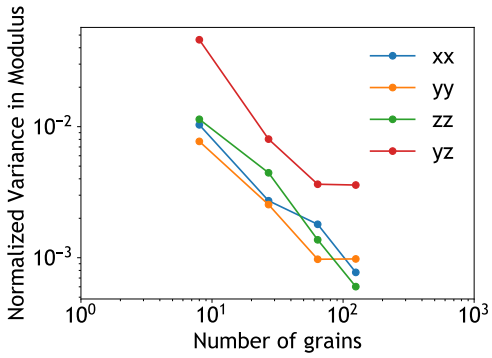


**Figure 2-20 Normalized variances of DNS-computed moduli as a function of number of grains.**

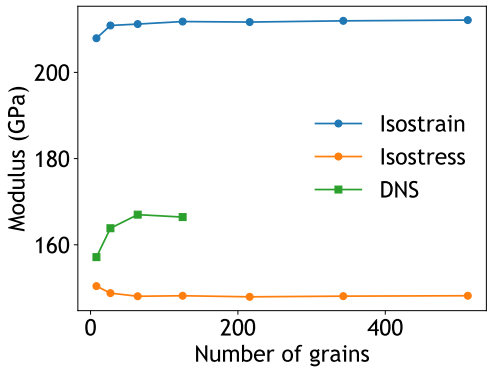


**Figure 2-21 Comparison of estimated and computed xx moduli.**

the notion of a material length-scale upon which the scaling of the variance is determined. It is the material length-scale which allows for the determination of the strength of the interactions between the constituents as a function of some physical quantity. Quantification of these interactions is required to move beyond simple averaging schemes such as (31) and (33) to more accurate estimations. The fact that the combination of these averages in (34) produces good estimates is somewhat of an accident; it seems that the enforcement of equilibrium and compatibility in an aggregate produces constraints that split the difference between the isostrain and isostress assumptions. The success of the self-consistent scheme (35) is not an accident, as it takes into account some version of the interactions between the constituents in an aggregate. However, extending this notion to plastically-deforming materials is not straightforward, so the following sections examine the mechanism underlying the self-consistent approximation: material points interact with each other over some distance, with the strength of the interaction decaying with increasing distance. Perhaps in understanding the scaling of this interaction, some insight into the general non-linear problem can be attained.

## 2.4. A notion of material length scale

The notion of a material length-scale features in many regularized theories of constitutive behavior and damage mechanics. However, the physical dimension corresponding to this concept is usually taken as a constant, rationalized by reference to some physical phenomenon after the fact. In practice, the material length-scale is a fitting parameter, and the a posteriori correspondence between the parameter value and some physical length-scale is, at best, taken as validation of the theory rather than incorporating this correspondence into the base of the theory. On top of the discomfort this may introduce is another set of challenges introduced by the possible evolution of the material length-scale. The paradigm previously mentioned makes the rationalization of any scheme to evolve the value of the material length-scale parameter difficult, and if such dynamics is incorporated into the theory, it must be close to strictly empirical or ad hoc. On the other hand, one might choose to examine the material length-scale and its evolution and to subsequently form a theory around this a priori determination of appropriate values and dynamics of the material length-scale. This manuscript represents an attempt at this endeavor of understanding the concept of a material length-scale for a particular set of phenomena and erecting a framework for quantifying the length-scale and its evolution.

The basis of this investigation is the autocorrelation function, which measures the likelihood that the value of some field at a point will take on a value similar to the values of the field in the neighborhood of the point. The notion of autocorrelation is perhaps more common in the analysis of time-series, where there is a wealth of theory and practical application in the literature. Application of the autocorrelation to spatial data is also well established, for example in geology, but applications in continuum solid mechanics are sparse. Nevertheless, it is argued here that autocorrelation is an effective lens through which to view material-length scales and provides valuable insight into heterogeneous deformations. In the following section, some basic mathematical preliminaries are discussed, and concepts are developed and applied to simulated random fields. Subsequently, the framework is applied to idealized problems in crystal

elasto-viscoplasticity, and some conclusions are drawn with respect to material length-scale and its evolution.

### 2.4.1. Mathematical preliminaries and definition of length scale

In the following exposition, it is assumed that there is a scalar random field $X$ which takes on a finite value $X(\boldsymbol{t})$ at every point $\boldsymbol{t} \in \mathcal{B}$ for some finite $d$-dimensional body $\mathcal{B} \subset \mathbb{R}^d$. The field $X$ is taken to be spatially homogeneous; that is, the probability density of $X$ at a point $\boldsymbol{t}_1$ is identical to the probability density of $X$ at a point $\boldsymbol{t}_2$ for all $\boldsymbol{t}_1, \boldsymbol{t}_2 \in \mathcal{B}$. It is also assumed that $X$ is ergodic; that is, sampling the spatial values of $X$ over $\mathcal{B}$ is equivalent to sampling the distribution of $X$, except for any effects of the finite size of $\mathcal{B}$. A brief review of the relevant treatments of these random fields is given below; a more thorough treatment can be found, for example, in [21].

The covariance function for a random field $X(\boldsymbol{t})$ is defined as

$$\begin{aligned} B(\boldsymbol{t},\boldsymbol{t}') &:= \mathrm{Cov}\left[X(\boldsymbol{t}), X(\boldsymbol{t}')\right] \\ &= \mathrm{E}\left[X(\boldsymbol{t})X(\boldsymbol{t}')\right] - \mathrm{E}\left[X(\boldsymbol{t})\right]\mathrm{E}\left[X(\boldsymbol{t}')\right] \end{aligned} \tag{44}$$

Because the field $X(\boldsymbol{t})$ is statistically homogeneous, the covariance function depends only on the lag vector $\boldsymbol{\tau} = \boldsymbol{t} - \boldsymbol{t}'$, and ergodicity ensures that the expectation can be obtained by a spatial integral. For the finite body $\mathcal{B}$, the covariance function is approximated by

$$B(\underline{\tau}) \approx \frac{1}{|\mathcal{B}_\tau|} \int_{\mathcal{B}_\tau} X(\boldsymbol{t}) X(\boldsymbol{t} - \boldsymbol{\tau}) dt \tag{45}$$

That is, the covariance function is approximated by an integral over a subset of the body $\mathcal{B}$, denoted $\mathcal{B}_\tau$ and defined as

$$\mathcal{B}_\tau = \{\boldsymbol{t} : \boldsymbol{t} \in \mathcal{B} \,\mathrm{and}\, \boldsymbol{t} - \boldsymbol{\tau} \in \mathcal{B}\} \tag{46}$$

A commonly explored form for the covariance function is the squared-exponential function, given in two dimensions by

$$B_{SE}(\tau_1, \tau_2) = \sigma^2 \exp\left(-\frac{\tau_1^2 + \tau_2^2}{2d^2}\right) \tag{47}$$

Taking $\boldsymbol{\tau} = \mathbf{0}$ in Equation (45), we obtain an approximation of the variance $\sigma^2 = B(\mathbf{0})$, so that the normalization of the covariance function yields the *autocorrelation* function:

$$\rho(\boldsymbol{\tau}) = \frac{B(\boldsymbol{\tau})}{B(\mathbf{0})} \tag{48}$$

For the squared-exponential covariance function, the autocorrelation function is thus

$$\rho_{SE}(\tau_1, \tau_2) = \exp\left(-\frac{\tau_1^2 + \tau_2^2}{2d^2}\right) \tag{49}$$

For reference, the landscape of (49) is shown in Fig. 2-22. The spectral density function is defined

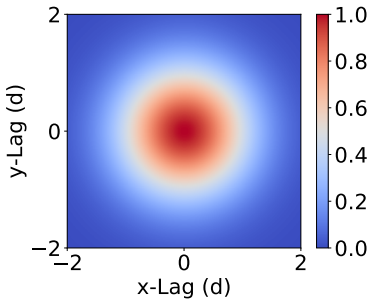


**Figure 2-22 Values of the two-dimensional squared-exponential auto-correlation function as a function of the normalized lag components $\tau_1/d$ and $\tau_2/d$.**

as the Fourier transform of the covariance function,

$$S(\boldsymbol{\omega}) = \mathcal{F}\{B\} \tag{50}$$

For the squared-exponential covariance function, the spectral density function is

$$S_{SE}(\omega_1, \omega_2) = \frac{\sigma^2 d^2}{2\pi} \exp\left\{ -\frac{d^2}{2}\left(\omega_1^2 + \omega_2^2\right) \right\} \tag{51}$$

By the convolution theorem,

$$S(\boldsymbol{\omega}) = \mathcal{F}\{X\}\overline{\mathcal{F}\{X\}} \tag{52}$$

Thus, the covariance function can be recovered via the inverse Fourier transform,

$$B(\boldsymbol{\tau}) = \mathcal{F}^{-1}\{S\} = \mathcal{F}^{-1}\{\mathcal{F}\{X\}\overline{\mathcal{F}\{X\}}\} \tag{53}$$

One limitation of the formula (45), as seen in (46) is that the approximation worsens with increasing magnitude of $\boldsymbol{\tau}$, given that the subset $\mathcal{B}_\tau$ 'shrinks' with increasing magnitude of $\boldsymbol{\tau}$, providing a smaller finite sample of the random field $X(\boldsymbol{t})$. Because brute-force computation via (45) scales badly, it is convenient to use (53); given a finite sample of the random field $X$ over the body $\mathcal{B}$, the covariance function can be efficiently estimated by applying fast Fourier transforms to the field data. This process is illustrated by way of application to some synthetic data in the following.

### *2.4.2. Synthetic random fields*

To apply the formulae of the previous section, it is necessary to generate some field data for analysis. In the interest of verifying the algorithms to be used, it is desirable to generate field data with known characteristics. Two methods to generate such data are explored here for a structured two-dimensional grid.

Given an autocorrelation such as (49) and a structured two-dimensional $M \times N$ grid with spacing $(\Delta\tau_1, \Delta\tau_2)$, a correlation matrix can be constructed, with entries

$$A_{ij} = \rho(\boldsymbol{\tau}_i - \boldsymbol{\tau}_j) \tag{54}$$

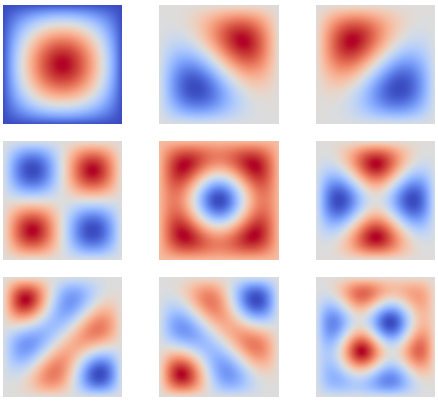

**Figure 2-23 Highest-energy KL modes in order of decreasing energy.**

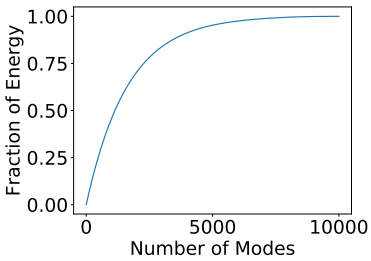


**Figure 2-24 The fraction of variance explained (energy) as a function of the number of KL modes included for .**

where $1 \leq i \leq MN$ and $1 \leq j \leq MN$ each index all of the points in the grid. The eigenvalues $\lambda_k$ and eigenvectors $\boldsymbol{v}_k$ of $A$ allow for the construction of a field $\boldsymbol{X}$ via the Karhunen-Loève Expansion (KLE),

$$\boldsymbol{X} = \sum_{k=1}^{MN} w_k \sqrt{\lambda_k} \boldsymbol{v}_k \tag{55}$$

where $w_k$ are drawn from a given distribution, taken here to be $\mathcal{N}(0,1)$. The highest energy KL modes are shown in Fig. 2-23. The KLE is slow to converge for the squared-exponential covariance function, as shown in Fig. 2-24. Nevertheless, it can be shown that the KLE is optimal, in the sense that it captures a given amount of energy with the fewest possible number of modes. An additional difficulty is the computation of the eigenmodes, which scales as $n^d$, where $l/n$ is the resolution for a given domain-size $l$ and number of points $n$, and $d$ is the dimensionality of the domain. The memory demands of this problem make the computational cost of generating random fields in this way intractable for system sizes larger than about $n = 100$ in 2D. By taking advantage of (53), it is possible to simulate much larger fields using an FFT-based technique, as described below.

Given an autocorrelation function $\rho$, such as (49), with associated spectral density $S$, such as (51),

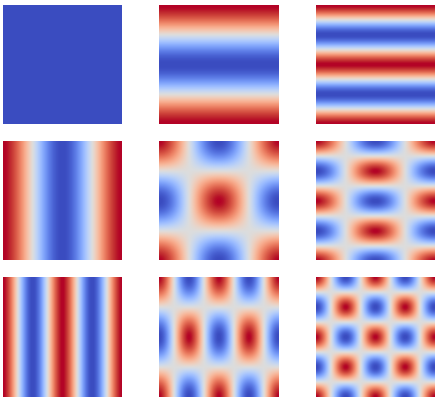

**Figure 2-25 Longest wavelength SRM modes in order of decreasing wavelengths.**

it is possible to generate a field $f(x_1,x_2)$ via the spectral representation method (SRM),

$$f(x_1,x_2) = \sqrt{2}\sum_{n_1=0}^{N_1-1}\sum_{n_2=0}^{N_2-1} A_{n_1n_2}\cos\left(\frac{n_1\kappa_{1u}}{N_1}x_1 + \frac{n_1\kappa_{2u}}{N_2}x_2 + \Phi^{(1)}_{n_1n_2}\right) + \tilde{A}_{n_1n_2}\cos\left(\frac{n_1\kappa_{1u}}{N_1}x_1 - \frac{n_1\kappa_{2u}}{N_2}x_2 + \Phi^{(2)}_{n_1n_2}\right) \tag{56}$$

$$A_{n_1n_2} = \sqrt{2S\left(\frac{n_1\kappa_{1u}}{N_1}, \frac{n_1\kappa_{2u}}{N_2}\right)\frac{\kappa_{1u}}{N_1}\frac{\kappa_{2u}}{N_2}} \tag{57}$$

$$\tilde{A}_{n_1n_2} = \sqrt{2S\left(\frac{n_1\kappa_{1u}}{N_1}, -\frac{n_1\kappa_{2u}}{N_2}\right)\frac{\kappa_{1u}}{N_1}\frac{\kappa_{2u}}{N_2}} \tag{58}$$

where $\Phi^{(1)}$ and $\Phi^{(2)}$ are two independent sets of random phase angles distributed uniformly on $[0,2\pi]$, and $\kappa_{1u},\kappa_{2u}$ are cutoff values in $k$-space beyond which it is assumed that $S \approx 0$. It can be shown [22] that $f$ has an autocorrelation function identical to $\rho$ in the limit as $N_1,N_2 \to \infty$. The first few SRM modes are shown in Fig. 2-25.

### *2.4.3. Estimates of length-scale*

Given a correlation structure, a natural next step is to quantify the decay of the autocorrelation in order to determine some measure of a length-scale over which values are significantly correlated. A brief discussion of the mathematics of one such determination follows; a detailed exposition is available, for example, in [21].

Given the random field $X(\underline{t})$, a new random field can be defined via:

$$X_{\mathcal{T}}(\underline{t}) = \frac{1}{|\mathcal{T}|}\int_{\mathcal{T}} X(\underline{\tau})d\mathcal{T} \tag{59}$$

Here, $\underline{t}$ is the center of an n-orthotope (line segment, rectangle, rectangular prism) $\mathcal{T} \subset \mathcal{B} \subset \mathbb{R}^d$ with extent $\underline{T} = (T_1, T_2, \ldots, T_d)$. In two dimensions,

$$X_{\mathcal{T}}(t_1,t_2) = \frac{1}{T_1 T_2} \int_{t_1-\frac{T_1}{2}}^{t_1+\frac{T_1}{2}} \int_{t_2-\frac{T_2}{2}}^{t_2+\frac{T_2}{2}} X(\tau_1,\tau_2) d\tau_2 d\tau_1 \tag{60}$$

The variance $\sigma^2_{\mathcal{T}}$ of the field $X_{\mathcal{T}}$ is related to the variance $\sigma^2$ of the field $X$ as

$$\sigma^2_{\mathcal{T}} = \gamma(\underline{T})\sigma^2 \tag{61}$$

In two dimensions, the correlation measure (characteristic area) $\alpha$ is defined as

$$\alpha = \lim_{T_1,T_2\to\infty} T_1 T_2 \gamma(T_1,T_2) \tag{62}$$

Equivalently, for the situations investigated here,

$$\alpha = \int_{-\infty}^{\infty}\int_{-\infty}^{\infty} \rho(x_1,x_2) dx_1 dx_2 \tag{63}$$

or

$$\alpha = \left(\frac{2\pi}{\sigma}\right)^2 S(0,0) \tag{64}$$

For an isotropic correlation structure, a single scale of fluctuation can be defined as

$$\theta = \sqrt{\alpha} \tag{65}$$

For a separable correlation structure, with

$$\rho(\tau_1,\tau_2) = \rho_1(\tau_1)\rho_2(\tau_2) \tag{66}$$

The one-dimensional scales of fluctuation $\theta^{(1)}$ and $\theta^{(2)}$ are given by

$$\theta^{(1)} = \int_{-\infty}^{\infty} \rho(x_1,0) dx_1 \tag{67}$$

$$\theta^{(2)} = \int_{-\infty}^{\infty} \rho(0,x_2) dx_2 \tag{68}$$

respectively, and

$$\alpha = \theta^{(1)}\theta^{(2)} \tag{69}$$

As an example an ellipsoidal correlation structure, which is separable but not isotropic, admits the following of an autocorrelation function

$$\rho(\tau_1,\tau_2) = \exp\left\{-\left(\frac{\tau_1}{a}\right)^2 - \left(\frac{\tau_2}{b}\right)^2\right\} \tag{70}$$

Of course, there is no guarantee that the principal coordinates $x_1$ and $x_2$ are aligned with the reference coordinates, so that in practice, the autocorrelation may behave as

$$\rho(x_1,x_2) = \exp\left\{-\left(\frac{x_1\cos(\theta)+x_2\sin(\theta)}{a}\right)^2 - \left(\frac{x_2\cos(\theta)-x_1\sin(\theta)}{b}\right)^2\right\} \tag{71}$$

The components of the (symmetric) moment tensor $\boldsymbol{M}$ are given by

$$[\boldsymbol{M}] = \begin{bmatrix} I_{11} & I_{12} \\ I_{12} & I_{22} \end{bmatrix} \tag{72}$$

$$I_{ij} = \int_{-\infty}^{\infty}\int_{-\infty}^{\infty} x_i x_j \rho(x_1, x_2) dx_1 dx_2 \tag{73}$$

These components must be approximated for a finite (square) sample as

$$I_{ij} \approx \int_{-L/2}^{L/2}\int_{-L/2}^{L/2} x_i x_j \rho(x_1, x_2) dx_1 dx_2 \tag{74}$$

The principal axes of correlation are determined from the eigenvalue analysis

$$\det(\boldsymbol{M} - \lambda_j \boldsymbol{I}) = 0 \tag{75}$$

$$\boldsymbol{M} \cdot \boldsymbol{v}_j = \lambda_j \boldsymbol{v}_j \tag{76}$$

where $\lambda_1$ and $\lambda_2$ are the eigenvalues corresponding to the eigenvectors $\boldsymbol{v}_1$ and $\boldsymbol{v}_2$, respectively. For (70) and (71),

$$\begin{bmatrix} x_1 \\ x_2 \end{bmatrix} = \begin{bmatrix} \cos(\theta) & -\sin(\theta) \\ \sin(\theta) & \cos(\theta) \end{bmatrix} \cdot \begin{bmatrix} \tau_1 \\ \tau_2 \end{bmatrix} \tag{77}$$

The major semi-axis is oriented in the $\tau_1$-direction with length $a$, and the minor semi-axis is oriented in the $\tau_2$-direction with length $b$. In this case, the components of the moment tensor are given by

$$I_{x_1x_1}(\theta) = \frac{\pi}{2}\left(\frac{\cos^2(\theta)}{b^2} + \frac{\sin^2(\theta)}{a^2}\right) a^3 b^3 \tag{78}$$

$$I_{x_1x_2}(\theta) = \frac{\pi}{4}\left(a^2 - b^2\right) ab \sin(2\theta) \tag{79}$$

$$I_{x_2x_2}(\theta) = \frac{\pi}{2}\left(\frac{\cos^2(\theta)}{a^2} + \frac{\sin^2(\theta)}{b^2}\right) a^3 b^3 \tag{80}$$

$$\tag{81}$$

The eigenvalues are given by

$$\begin{aligned} \lambda_1 &= \frac{\pi}{2} a^3 b = I_{x_1x_1}(\theta = 0) \\ \lambda_2 &= \frac{\pi}{2} ab^3 = I_{x_2x_2}(\theta = 0) \end{aligned} \tag{82}$$

with $\lambda_1 \geq \lambda_2$. The corresponding eigenvectors are

$$\begin{aligned} \boldsymbol{v}_1 &= \begin{bmatrix} \cos(\theta) \\ \sin(\theta) \end{bmatrix} \\ \boldsymbol{v}_2 &= \begin{bmatrix} -\sin(\theta) \\ \cos(\theta) \end{bmatrix} \end{aligned} \tag{83}$$

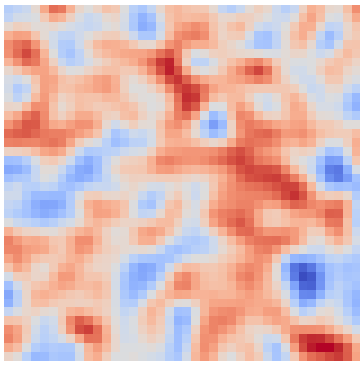

**Figure 2-26 Simulated random field with box length / correlation length = 20 and correlation length / pixel size = 2.**

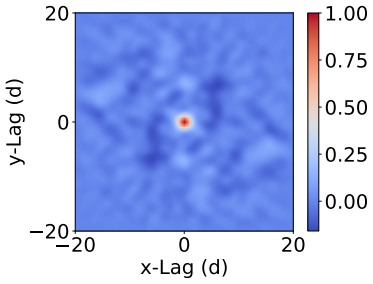


**Figure 2-27 Correlation structure of simulated random field with box length / correlation length = 20 and correlation length / pixel size = 2.**

Thus, the alignment of the correlation structure with respect to the spatial orientation is characterized by $\theta$, which can be approximated from $\boldsymbol{v}_1$ and $\boldsymbol{v}_2$, and the constants $a$ and $b$ can be determined as

$$a = \left( \frac{4\lambda_1^3}{\pi^2 \lambda_2} \right)^{1/8} \tag{84}$$

$$b = \left( \frac{4\lambda_2^3}{\pi^2 \lambda_1} \right)^{1/8} \tag{85}$$

Here, an ellipsoidal correlation structure is assumed for short lags in order to make certain approximations to facilitate the inference of length-scales from finite samples, as discussed next.

An example of a simulated random field with correlation as in (49) and generated with the KLE method is shown in Fig. 2-26. The correlation structure of this field is shown in Fig. 2-27, where it can be seen that there is significant pollution due to the effects of the finite size of the sample. A problem arises in evaluating the correlation of points with lag approaching the size of the simulated domain. Either the number of averaging points must be reduced, or the data must be padded with an artificial field which may not obey the correlation structure of simulated field. It is of course possible to generate larger domains for theoretical investigation, but there is no

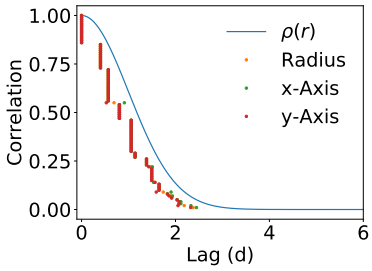


**Figure 2-28 Approximation of the correlation structure of simulated random field with box length / correlation length = 20 and correlation length / pixel size = 2.**

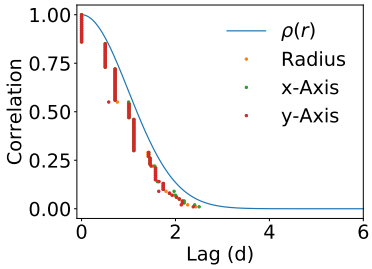


**Figure 2-29 Corrected approximation of the correlation structure of simulated random field with box length / correlation length = 20 and correlation length / pixel size = 2.**

guarantee that a real field of interest will have a domain size significantly larger than its correlation length. Here, an attempt to circumvent this difficulty for a limited class of correlation structures is outlined.

It is assumed that the correlation structure of the field possesses at least ellipsoidal symmetry, and then the process proceeds as follows. First, the correlation structure of the field is analyzed using the domain padding technique. Then, convex hulls are generated for a number of correlation cutoffs, and the area and moments of these hulls is computed in order to extract equivalent circle radii and equivalent ellipse axes. The results are shown in Fig. 2-28. In the figure, it is clearly seen that this procedure underestimates the true radius (axes) due to the polygonal approximation of the convex hull. Now, the ratio of the area of a circumscribed circle to an inscribed regular polygon with $n$ vertices is

$$\frac{A_{circ}}{A_{poly}} = \frac{2\pi}{n\sin\left(\frac{2\pi}{n}\right)} \tag{86}$$

Taking the square-root of this ratio as a correction factor, the approximation is improved, as shown in Fig. 2-29. From Fig. 2-29, it is clear that the approximation of the correlation is not at all accurate beyond about 2.5 times the length-scale $d$. Thus, the correlation computation is repeated with a field reduced in size from the full field by $2.5d$ at each edge, and using no padding of the domain. This results in a much smaller window on the correlation structure, but the approximation is greatly improved, as seen in Fig. 2-30. This again clearly improves the quality of the approximation. For the final step, the values of r (or a and b) for which there is a change in

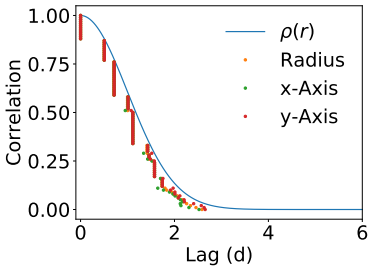


**Figure 2-30 Corrected, reduced approximation of the correlation structure of simulated random field with box length / correlation length = 20 and correlation length / pixel size = 2.**

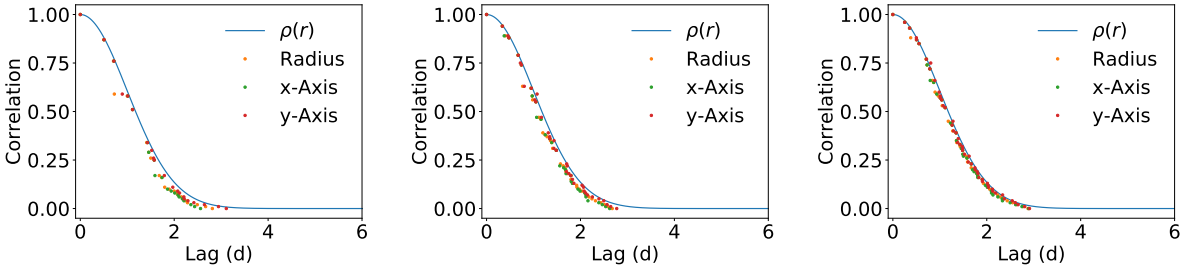


**Figure 2-31 Corrected, reduced approximation of the correlation structure of simulated random field with box length / correlation length = 20 and correlation length / pixel size = 2, 3, 4.**

the correlation are extracted, yielding the final set of data shown in Fig. 2-31. Also shown in Fig. 2-31 is the convergence with respect to the pixel size. Evidently, a pixel size of $0.25d$ yields a reasonably converged set of data for this problem.

With this theoretical and computational machinery in hand, the next step is to analyze a problem of some value. The first choice is a problem in 2D crystal elasticity, as described next.

The computation of elastic response is relatively inexpensive, so a large microstructure is created in order to fully characterize the correlation structure of the mechanical fields, and to insulate this calculation from any pollution of boundary effects. The microstructure, shown in Fig. 2-32, is comprised of 16384 square-shaped grains arrayed in a 128-grain by 128-grain grid. Each grain is discretized with 64 quadrilateral elements with square aspect, arrayed in an 8 by 8 grid. The total number of 2D finite elements is thus around 1M. An elastic step is simulated with a finite time step, and the mechanical fields are recorded.

The stress field is shown component-wise in Fig. 2-33. It is seen in the figure that the fields are heterogeneous, with some correlation structure that appears as an irregular waviness. This structure is clearly illuminated in the plots of the autocorrelations in Fig. 2-33. Some interesting qualitative features can be seen in the plots of autocorrelation. First, the orientation-dependence of the correlation structures for the normal stresses clearly reflects the waviness apparent in the fields. For the xx-component of the stress, the waves appear to be aligned in the y-direction (as if moving in the x-direction). There are faint vertical lines in the plot of the xx- stress

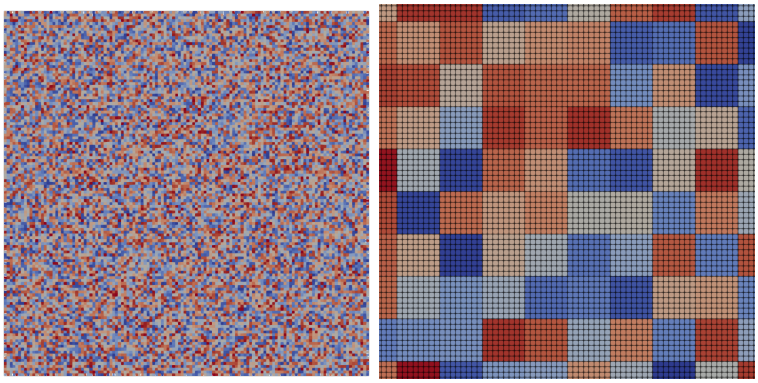

**Figure 2-32 Idealized two-dimensional microstructure with $16384 = 128^2$ grains, each represented by $64 = 8^2$ finite elements. Left: full microstructure. Right: portion of microstructure enlarged to show detail.**

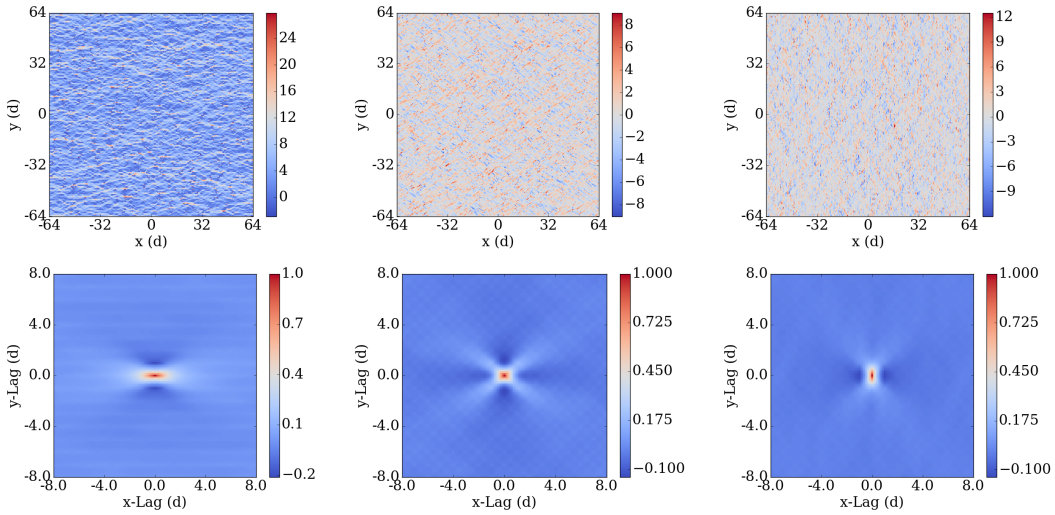


**Figure 2-33 Fields (top row) and autocorrelations (bottom row) for stress components -xx (left column), -xy (middle column), and -yy (right column).**

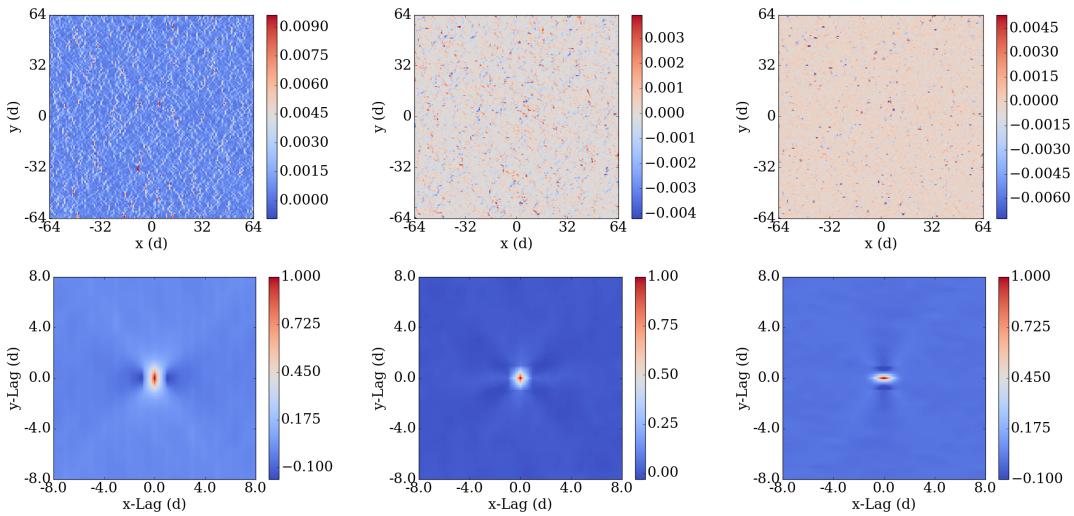


**Figure 2-34 Fields (top row) and autocorrelations (bottom row) for rate of deformation components -xx (left column), -xy (middle column), and -yy (right column).**

autocorrelation, indicating that this order persists over a length-scale much larger than the grain size. Also, there is a weak negative correlation evident between the values in one grain and the adjacent grain in the x-direction (x-adjacent), indicating that regions of high stress intensity are x-adjacent to regions of low stress intensity, reinforcing the intuitive notion of waviness. For the yy-stress the story is similar, but rotated into the y-direction. For the xy-component of the stress, there is positive correlation with grains in the diagonal neighboring positions and week negative correlation with grains in the x- and y-adjacent neighboring positions. It is tempting to conclude on the basis of these structures that there exists a short-range order induced by the governing equations and a superposed long-range order induced by the microstructure, but deeper analysis would be required to fully realize such conclusions and provide some quantification of these effects.

The components of the rate of deformation are shown in Fig. 2-34. It is immediately evident that the qualitative analysis of the stress component fields applies to the components of the rate of deformation, but with a rotation of the structure (90° for the normal components, and 45° for the shear component).

The internal power $\dot{W} = \boldsymbol{\sigma} : \boldsymbol{D}$ field is shown in Fig. 2-35. The local correlation structure has an interesting landscape that bears further analysis. The long-range structure is quite clear; there appear points of relatively high correlation at every point in the figure with x-lag and y-lag equal to an integer multiple of the grain size. It is very tempting to conclude that this long-range structure relates to the stress-concentration that appears at grain boundaries and quadruple points. The quantification of this effect is an ongoing effort, but the results that follow suggest that there is an important phenomenology revealed by this observation. To illustrate this and other salient points, the analysis turns to the elasto-viscoplastic response next.

In light of the rapid decay of the autocorrelation evident in the results in the previous section, and

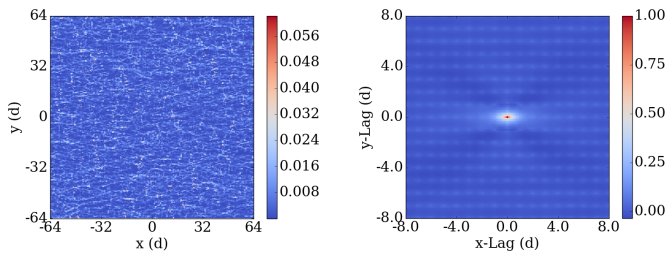


**Figure 2-35 Field (left) and autocorrelation (right) for internal power.**

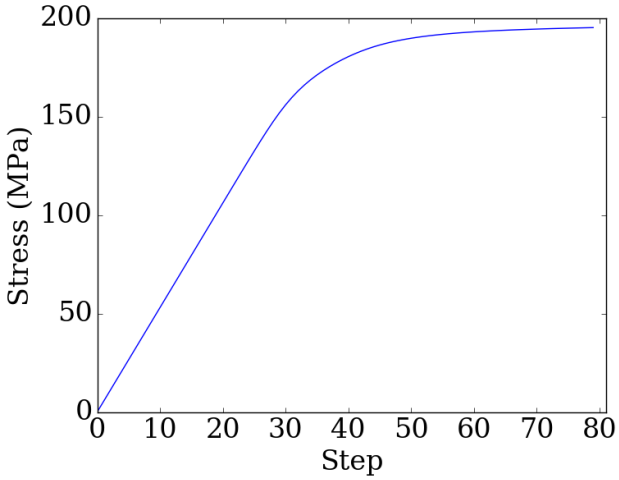


**Figure 2-36 Stress response of $4 \times 4$ microstructure given as function of timestep.**

driven by a desire to reduce the computational cost for the more involved elasto-viscoplastic calculations, a much smaller microstructure is examined in this section. Here, the finite element domain consists of $16 = 4 \times 4$ grains, each discretized with $256 = 16 \times 16$ quadrilateral elements. Simulations are run over many steps, well into the regime of post-yield plasticity. Here the focus is on the mechanical behavior in the vicinity of yield, which reveals interesting properties of the autocorrelation of the mechanical fields.

For reference, the stress as a function of timestep is plotted in Fig. 2-36. The internal power fields are plotted for a few representative timesteps in Fig. 2-37. The fields before step 20 and after step 50 are qualitatively similar to those shown in Fig. 2-37, although the absolute magnitude of the fields change. Around yield, though, there is a significant shift from the elastic toward the (nearly) fully viscoplastic behavior. The autocorrelation function values corresponding to these snapshots are shown in Fig. 2-38. There is a clear shift in the plots in Fig. 2-38 from a correlation structure that is initially biased toward the x-direction, through a more isotropic structure near yield, to a structure that is biased in the y-direction in the post-yield regime. Looking ahead, it seems likely that the post-yield structure is setting up the microstructure to localize along a y-oriented band of high power intensity, as would be expected. In the regime investigated here, what is clear is that a semi-permanent structure develops in the power field, as evidenced by the estimate of the correlation length shown in Fig. 2-39. In the figure, it can be seen that the correlation length of the internal power field is maintained at around the grain size $d$ over the

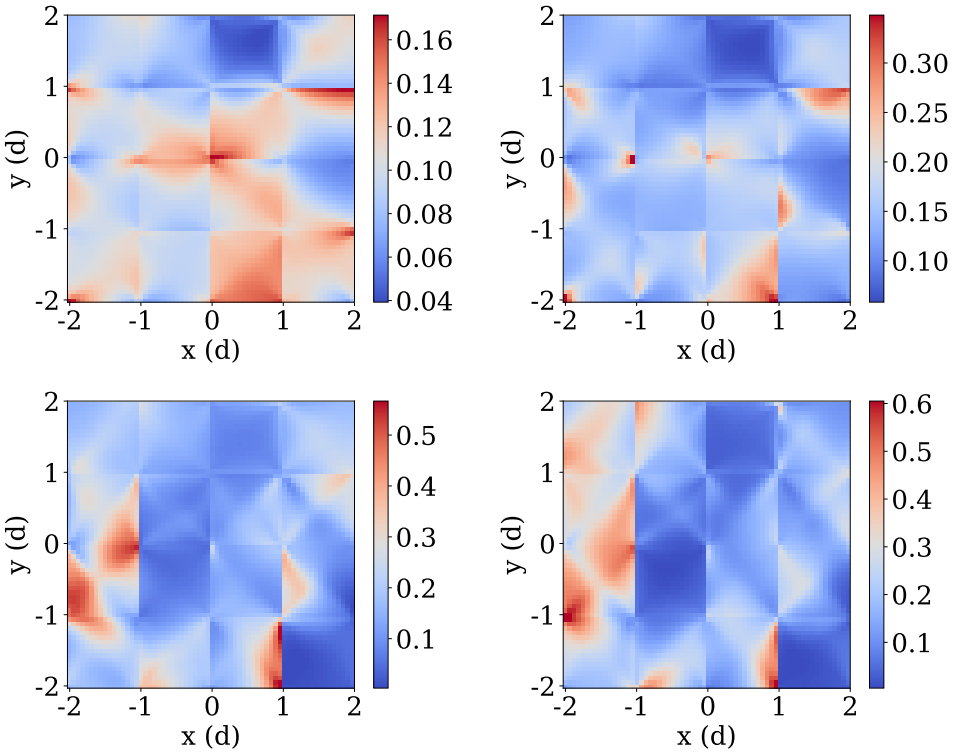


**Figure 2-37 Power field for timesteps 20, 30, 40, 50.**

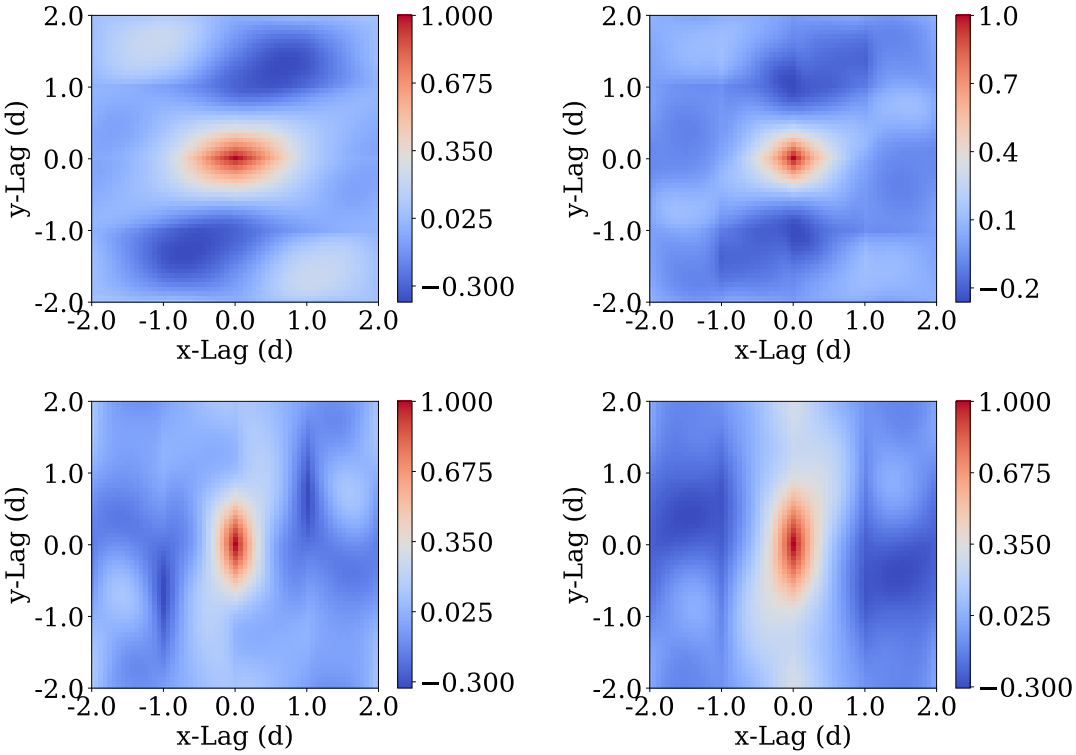


**Figure 2-38 Autocorrelations for the internal power at timesteps 20, 30, 40, 50.**

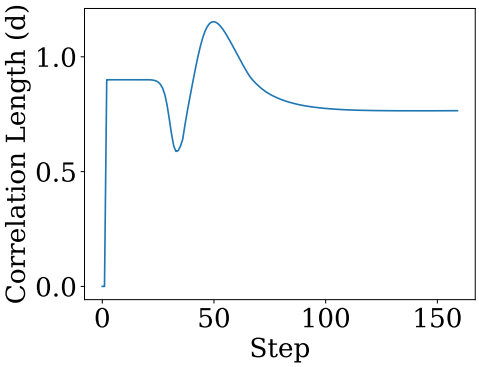


**Figure 2-39 The evolution of the estimated correlation length.**

course of the simulation, and that it is very stable in both the fully elastic and the (nearly) fully viscoplastic regimes. To investigate points beyond the end of this stable regime, a more realistic microstructure is considered in the following section.

# 3. UNCERTAINTY QUANTIFICATION METHODS FOR REPRESENTING MATERIAL VARIABILITY

In this section we describe techniques to model a distribution of mechanical responses by mapping the variability onto physical, interpretable material parameters of a chosen model. We also outline how to use Bayesian model section to select the most plausible model from a set of models given data, and how to handle high-dimensional uncertainties such as the specific locations of voids simultaneously with parameter distributions.

## 3.1. Physical parameter distributions

We adopt a Bayesian approach to the calibration problem [23, 24, 25, 26, 27, 28], which involves searching for the plausible parameters $\boldsymbol{\theta}$ of the selected model given data. In contrast to least-squares fitting resulting in a single set of parameter values, in a Bayesian perspective the parameters are considered random variables with associated probability density functions (PDFs) that incorporate both prior knowledge and observed data. The choice of Bayesian methods is well motivated by the data, which agree with the chosen model to a high degree but uncertainty is present in the model parameters both within and across all batches. Bayesian calibration results in a joint posterior probability density of the parameters $p(\boldsymbol{\theta}|D,M)$ based on the observations $D$ given the model choice $M$. The parametric uncertainty reflected in the posterior PDF depends on the consistency of the model with the data and the amount of data. As mentioned in the Introduction, we aim to quantify the material variability using this probabilistic framework and physical interpretations of the model parameters.

### 3.1.1. Bayesian inference for parameter calibration

Consider our model $M$ for the engineering stress $\sigma = M(\varepsilon;\boldsymbol{\theta})$, being a full finite element plasticity model with an underlying plasticity model, where $\varepsilon$ is the independent variable and $\boldsymbol{\theta}$ is the vector containing physical parameters $\{E,Y,H,K,B\}$ as well as auxiliary and nuisance parameters which will be defined later. By setting $\{H,K,B\}$ or $\{K,B\}$ to zero we can form a nested sequence of models with 2, 3, or 5 parameters with perfect plastic, linear hardening, or saturation hardening phenomenology, respectively. Given that we only have one dimensional tension data (no information on lateral contraction), we fix the Poisson's ratio to a commonly accepted value for steel, $\nu = 0.3$; however, we allow the Young's modulus, $E$, to vary so that the locus of yield points is not constrained to a line. We also allow for geometric variability through a non-dimensional cross-section correction factor, $A$, that influences the model output linearly, $\sigma = A \times M(\varepsilon;\boldsymbol{\theta})$, and include $A$ in the parameter set $\boldsymbol{\theta}$. This geometric correction is motivated by the fact that the observed engineering stress data was computed using an average cross-sectional areas based on the outer dimensions of each sample, and can be interpreted as the ratio of the effective load bearing area of the sample to its measured average area. The correction factor $A$ aims to mitigate the effect of utilizing one nominal value for cross-sectional area per sample rather than utilizing a more accurate spatially-varying area profile for each sample and the fact that the outer dimensions lead to an overestimate of actual load bearing area of the AM tensile specimens due to the physical imperfections. Since the gauge length, and hence the strain, are relatively error free, we do not include a correction factor for it in the calibration parameters.

In a Bayesian setting for model calibration and selection, Bayes' rule is used to relate the information contained in the data and prior assumptions to the parameters in the form of a posterior probability density function as

$$p(\boldsymbol{\theta}|\mathcal{D},M) = \frac{p(\mathcal{D}|\boldsymbol{\theta},M)\,p(\boldsymbol{\theta}|M)}{p(\mathcal{D}|M)}\,. \tag{87}$$

Here $p(\mathcal{D}|\boldsymbol{\theta},M)$ is the likelihood of observing the data $\mathcal{D}$ given the parameters $\boldsymbol{\theta}$ and model $M$, $p(\boldsymbol{\theta}|M)$ is the prior density on the parameters reflecting our knowledge *before* incorporating the observations, and $p(\mathcal{D}|M)$ is the model evidence (which we will compute for model selection purposes). It is important to note that the denominator is typically ignored when sampling from the posterior since it is a normalizing factor, independent of $\boldsymbol{\theta}$, that ensures the posterior PDF to integrate to unity; however, this term, known as the model *evidence*, plays a central role in model selection, as will be described later. In this context, we will employ uninformative (or weakly informative) prior densities due to lack of prior knowledge of the model parameters in the present context of the response of AM tensile specimens. Experimental data influences the resulting posterior probability only through the likelihood $p(\mathcal{D}|\boldsymbol{\theta},M)$, which is based on some normalized measure of the distance between the data $\mathcal{D}$ and the model predictions $M(\varepsilon;\boldsymbol{\theta})$. The likelihood plays an analogous role to the cost/objective function in traditional fitting/optimization in the sense that it describes the misfit between model predictions and observational data. Specific forms of the likelihood will be discussed in Sec. 3.1.2. As Eq. (87) suggests, the outcome is conditioned on the model chosen, leading to questions regarding model comparison and selection which will be discussed in Sec. 3.1.3. In general, given the complexities of the model $M$, the posterior density $p(\boldsymbol{\theta}|\mathcal{D},M)$ is not known in closed form and one has to resort to numerical

methods to evaluate it. Markov chain Monte Carlo (MCMC) methods [29, 30] provide a suitable way to sample from the posterior density, while kernel density estimation, for example, can be used to provide subsequent estimates of the posterior PDF.

### 3.1.2. Accounting for material variability using error models

We want quantify the effect of material variability induced by the additive manufacturing process on the predicted mechanical response. To do this we use a Bayesian model calibration framework with statistical error models that provide stochastic model predictions. There are many approaches to model error characterization and quantification. In a Bayesian framework, Kennedy and O'Hagan [23] developed a framework for characterizing model error by employing a linear stochastic model in the form of an additive Gaussian process discrepancy term (see also [31, 32, 33]). Despite its flexibility, this additive error model cannot guarantee that the stochastic model predictions indeed satisfy the underlying governing equations and physical constraints (*e.g.* positivity of solution fields). Secondly, the discrepancy terms are calibrated to specific output responses and not generally relevant in characterizing variability of unobserved model outputs (or parameters).

An alternative strategy of increasing popularity is to embed the variability into the physical model itself, rendering it a stochastic model. This approach essentially assigns statistical bias correction terms to internal model components or parameters (see, for example, [34, 35, 28, 36, 37, 38, 39, 40]). Note that, while this approach alleviates the aforementioned limitations of the additive error model, the stochastic model predictions are bound to the original structure of the model and thus susceptible to possible deficiencies relating to the model structure itself (*e.g.* due to unmodeled physics [41, 42]).

We will consider these two approaches in representing the effects of material variability. Since each strategy leads to qualitatively different predictions, interpretations, and realizations, we are interested in how each is able to capture intrinsic material variability. In this section, we will discuss how, given that plastic strain is a coarse metric of the inelastic deformation in additively manufactured materials, discrepancies between the observed data and the model predictions can be interpreted physically.

Consider the $k$-th stress-strain curve from the $i$-th batch which consists of a sequence of stress observations $\{\sigma_j^{(i,k)}\}_{j=0}^{n_\varepsilon-1}$ obtained at the strain locations $\{\varepsilon_j\}_{j=0}^{n_\varepsilon-1}$. A widely-adopted approach is to express the discrepancy between a noisy observation and the true stress using an additive measurement noise model, as in

$$\sigma_j^{(i,k)} = M_t^{(i,k)}(\varepsilon_j) + \eta_j^{(i,k)}, \tag{88}$$

where $M_t^{(i,k)}$ is the true stress and $\{\eta_j^{(i,k)}\}_{j=0}^{n_\varepsilon-1}$ are independent and identically distributed (i.i.d.) Gaussian random variables that capture the measurement errors. This i.i.d. assumption is a justifiable one since one can argue that the batches are independent. Furthermore, within a given batch, we assume all the $N_i$ stress-strain curves are independent since each experiment is a self-contained test, performed on separate specimens.

The true stress can also be approximated by a model prediction, $M(\varepsilon_j;\boldsymbol{\theta})$, and additive model error, $\delta_j^{(i,k)}$, given by

$$M_t^{(i,k)}(\varepsilon_j) = M(\varepsilon_j;\boldsymbol{\theta}) + \delta_j^{(i,k)}, \tag{89}$$

with corresponding model parameter vector $\boldsymbol{\theta}$. This is a commonly used method due to its simplicity [23]. Combining Eqs. 88 and 89, we get the relationship between model predictions and observed stress:

$$\sigma_j^{(i,k)} = M(\varepsilon_j;\boldsymbol{\theta}) + \delta_j^{(i,k)} + \eta_j^{(i,k)}. \tag{90}$$

A structure for the model error, $\delta_j^{(i,k)}$, is more difficult to prescribe than that for the measurement error. Given that this additional term is not physically associated with the presumed sources of non-measurement (material and other physical) variability, its applicability outside the training regime is tenuous. Furthermore, the additive combination of the two error terms can lead to challenges in disambiguation in a parameter estimation context (resulting in identifiability-related issues). To alleviate such issues, one commonly-used simplifying assumption is to also assume an i.i.d. Gaussian model errors, $\delta_j^{(i,k)}$. Under this assumption, the two sources of errors can be combined into one error term, $\zeta_j^{(i,k)}$, as in

$$\sigma_j^{(i,k)} = M(\varepsilon_j;\boldsymbol{\theta}) + \zeta_j^{(i,k)}. \tag{91}$$

In lieu of a completely characterized error model (which is rarely obtained in practice), the i.i.d. zero-mean Gaussian random variables $\zeta_j^{(i,k)}$ are completely characterized by an unknown variance given by $\varsigma^2$. Given the full data set for the $i$-th batch (denoted by $\mathcal{D}_i$), the resulting parameter likelihood has the form:

$$p(\mathcal{D}_i|\boldsymbol{\theta},M) = \prod_{j=0}^{n_\varepsilon-1}\prod_{k=1}^{N_i}(2\pi\varsigma^2)^{-1/2}\exp\left(-\frac{(\sigma_j^{(i,k)} - M(\varepsilon_j;\boldsymbol{\theta}))^2}{2\varsigma^2}\right). \tag{92}$$

The standard deviation $\varsigma$ of the joint error attributed to modeling error as well as observational noise can be either fixed in advance based on prior knowledge or inferred along with the other unknown parameters $\boldsymbol{\theta}$. Moreover, it can be assumed to be either constant or varying with the strain value.

As mentioned, the use of an additive model error term in Eq. (89) can lead to violations of physical laws and constraints [43, 44] and other difficulties. In order to avoid these difficulties, we embed the model variability/discrepancy in key parameters, essentially converting the unknown parameters into random variables that introduce variability in model predictions due to their uncertain nature. This approach, as detailed in [28], represents selected parameters using polynomial chaos expansions (PCE). In our context, we will assume a uniform distribution for each parameter in Eq. (91), given by the first-order Legendre-Uniform PCE:

$$\theta_i = \alpha_{i,0} + \alpha_{i,1}\xi_i\ , \tag{93}$$

in which $\alpha_{i,0}$ represents the mean term and $\alpha_{i,1}$ dictates the level of variability in $\theta_i$ which contributes to the variability in the observed responses. We will also consider the model selection

problem as to whether or not to embed the variability in $\theta_i$, which amounts to keeping the $\alpha_{i,1}$ term or setting it explicitly to zero. These coefficients (one or two per parameter) need to be inferred from the experimental observations. Such embedding of variability, along with an additive measurement noise term, can account for both material variability and measurement errors, respectively. A noticeable advantage of this approach, when compared to employing additive error alone, is that the material variability is explicitly captured by the model parameters and hence we can propagate the calibrated *parametric* variability through numerical simulations to any output of interest. Note that this use of a PCE is distinct from its use in the surrogate modeling, where the extent of $\boldsymbol{\theta}$ will selected to cover the feasible range of the parameters and not inferred, as it is in this context. Also note that higher order expansions of $\theta_i$ are capable of capturing correlations in the embedded variability. We employ the first order representation Eq. (93) to minimize the number of unknowns $\alpha_{i,j}$ that need to be calibrated.

The problem of calibrating such an embedded variability model is equivalent to that of estimating the probability density functions of the parameters in which the variability is embedded. Specifically, our objective is to estimate $\boldsymbol{\alpha} = \{\alpha_{i,0}, \alpha_{i,1}, \ldots\}$ that parametrize the density of $\boldsymbol{\theta}$. This is in contrast to the additive error formulation of Bayesian inference for parameter estimation, in which one infers the model parameters and not their density. Also, the data for our present calibration problem motivates the embedded approach since it suggests the uncertainties are aleatory/irreducible rather than epistemic/reducible. Specifically, the similar mechanical responses primarily vary sample-to-sample, as opposed to varying within the response of a particular sample, which suggests variations of material properties across specimens as opposed to a stochastic process active in each specimen.

In this context, the model calibration problem thus involves finding the posterior distribution on $\boldsymbol{\alpha}$ via Bayes' theorem Eq. (87)

$$p(\boldsymbol{\alpha}|\mathcal{D}, M) = \frac{p(\mathcal{D}|\boldsymbol{\alpha}, M)\, p(\boldsymbol{\alpha}|M)}{p(\mathcal{D}|M)}, \tag{94}$$

where $\boldsymbol{\alpha}$ has been substituted for $\boldsymbol{\theta}$, $p(\boldsymbol{\alpha}|\mathcal{D}, M)$ denotes the posterior PDF, $p(\mathcal{D}|\boldsymbol{\alpha}, M)$ is the likelihood PDF, and $p(\boldsymbol{\alpha}|M)$ is the prior PDF. Note that $\boldsymbol{\alpha}$ reduces to the classical parameter vector $\boldsymbol{\theta}$ when no embedding of variability is performed ($\theta_i = \alpha_{i,0}$ and $\alpha_{i,j} = 0$ for $j > 0$). Among the different options detailed in Ref. [28] for the likelihood construction, we employ the marginalized likelihood, which for the $i$-th batch $\mathcal{D}_i$, can be written as

$$p(\mathcal{D}_i|\boldsymbol{\alpha}, M) = \frac{1}{(2\pi)^{\frac{N_i n_\varepsilon}{2}}} \prod_{j=0}^{n_\varepsilon - 1} \prod_{k=1}^{N_i} \frac{1}{\varsigma_j(\boldsymbol{\alpha})} \exp\left[ -\frac{(\mu_j(\boldsymbol{\alpha}) - \sigma_j^{(i,k)})^2}{2\varsigma_j^2(\boldsymbol{\alpha})} \right], \tag{95}$$

where

$$\mu_j(\boldsymbol{\alpha}) = \mathbb{E}_{\boldsymbol{\xi}}[M(\varepsilon_j; \boldsymbol{\theta}(\boldsymbol{\alpha}, \boldsymbol{\xi}))] \tag{96}$$

and

$$\varsigma_j^2(\boldsymbol{\alpha}) = \mathbb{V}_{\boldsymbol{\xi}}[M(\varepsilon_j; \boldsymbol{\theta}(\boldsymbol{\alpha}, \boldsymbol{\xi}))] + \varsigma^2 \tag{97}$$

are the mean and variance of the model predicted stress at fixed $\boldsymbol{\alpha}$ and strain point $\varepsilon_j$. These moments are computed using the quadrature techniques that are commonly relied upon in uncertainty propagation, as in the input characterization, Eq. (93); see Ref. [28] for detailed description of the methodology involved in likelihood evaluation.

#### *3.1.3. Bayesian model selection*

The expansion in Eq. (93) resulting from the embedded model discrepancy approach is general in that it does not impose limitations on which parameters should embed the variability. Furthermore, as mentioned in Sec. 3.1.1, we can model the stress using 2, 3, or 5 physical parameters. We have also chosen to examine the inclusion of a cross-section correction factor, $A$, which could also be chosen as another parameter in which to embed an variability. Therefore, there are three physical models that are competing to fit the data, with up to 6 physical parameters, all of which are competing to be bestowed with an embedded variability term. This amounts to a total of 88 plausible models that are competing to fit the given data. Since determining the optimal model and optimal set of parameters for embedding of model variability *a priori* is not possible, we perform model selection using Bayes factors [45, 46]. This method of model selection is a data based approach that selects the optimal model as the one that strikes the best balance between data-fit and model simplicity [47, 48]. This balance is monitored using the so-called model evidence, or marginal likelihood, for each model $M$, given by

$$p(\mathcal{D}|M) = \int p(\mathcal{D}|\boldsymbol{\alpha}, M)\, p(\boldsymbol{\alpha}|M)\, \mathrm{d}\boldsymbol{\alpha}\,. \tag{98}$$

The computation of the model evidence $p(\mathcal{D}|M)$ is typically neglected in Bayesian calibration as it acts merely as a normalizing factor in Bayes' rule, Eq. (87). The model evidence acts as a quantitative Ockham's razor that, when maximized, performs an explicit trade-off between the data-fit and the model simplicity [47]. This is elucidated when examining the logarithm of the model evidence [49, 50]:

$$\mathbb{E}[\ln p(\mathcal{D}|M)] = \mathbb{E}[\ln p(\mathcal{D}|\boldsymbol{\alpha}, M)] - \mathbb{E}\left[\ln \frac{p(\boldsymbol{\alpha}|\mathcal{D}, M)}{p(\boldsymbol{\alpha}|M)}\right] \tag{99}$$

where the expectation $\mathbb{E}[\cdot]$ is with respect to the posterior PDF, $p(\boldsymbol{\alpha}|\mathcal{D}, M)$. The first term on the right hand side of Eq. (99) quantifies the data-fit and is known as *goodness-of-fit*. The second term is equal to the relative entropy (or Kullback-Leibler divergence) between the prior and posterior PDFs, also known as the *information gain* [51]. Given sufficient data $\mathcal{D}$, the information gain is normally higher for more complex models (models with more parameters or with parameters of greater prior PDF support reflecting poor prior knowledge as to their values). Hence, the information gain term quantifies model complexity by examining the relative difference between prior and posterior PDFs. This is in contrast to the frequentist approach where model complexity, in general, only depends on the number of model parameters rather than their relative prior supports [51].

Model selection using Bayes factors involves the pairwise comparison of plausible models, with Bayes factor defined as the ratio of their evidences given by

$$B(M_i, M_j) = \frac{p(\mathcal{D}|M_i)}{p(\mathcal{D}|M_j)} = \frac{\int p(\mathcal{D}|\boldsymbol{\alpha}, M_i)\, p(\boldsymbol{\alpha}|M_i)\, \mathrm{d}\boldsymbol{\alpha}}{\int p(\mathcal{D}|\boldsymbol{\alpha}, M_j)\, p(\boldsymbol{\alpha}|M_j)\, \mathrm{d}\boldsymbol{\alpha}} \tag{100}$$

with $B(M_i, M_j) > 1$ indicating that model $M_i$ is more likely while $B(M_i, M_j) < 1$ indicates that $M_j$ is the more likely model. One can supplement the evidence with prior belief on these models (called prior model probability) and in that case we would be interested in the ratios of posterior model probabilities. In our context, we assume that all models have equal prior probabilities ahead of analyzing the data and thus Bayes factor is a suitable way to compare the available models.

The key challenge is to compute the model evidence efficiently and accurately. In this investigation, we will modify a technique known as adaptive Gauss-Hermite quadrature [52, 53, 40, 54] by employing importance sampling for integration rather than Gauss quadrature, due to the poor scalability of quadrature techniques in higher dimensions. In an importance sampling framework, we utilize a multivariate normal distribution $q$ as a proposal/sampling distribution, with a mean vector $\boldsymbol{\mu}$ and covariance matrix $\boldsymbol{\Sigma}$ equal to the posterior mean and posterior covariance of $\boldsymbol{\alpha}$, *i.e.*

$$q(\boldsymbol{\alpha}) = \frac{1}{\sqrt{(2\pi)^{d_\alpha} |\boldsymbol{\Sigma}|}} \exp\left( -\frac{1}{2} (\boldsymbol{\alpha} - \boldsymbol{\mu})^\intercal \boldsymbol{\Sigma}^{-1} (\boldsymbol{\alpha} - \boldsymbol{\mu}) \right). \tag{101}$$

The model evidence $\eta$, being an integral over the parameter space, can now be estimated using importance sampling with $q$ as the proposal distribution. To do this, we reformulate the evidence as

$$\eta = \int p(\mathcal{D}|\boldsymbol{\alpha}, M)\, p(\boldsymbol{\alpha}|M)\, \mathrm{d}\boldsymbol{\alpha} = \int \frac{\int p(\mathcal{D}|\boldsymbol{\alpha}, M)\, p(\boldsymbol{\alpha}|M)}{q(\boldsymbol{\alpha})} q(\boldsymbol{\alpha}) \mathrm{d}\boldsymbol{\alpha}\,, \tag{102}$$

and utilize the change of variable $\boldsymbol{\alpha} = \mathsf{L}\widetilde{\boldsymbol{\alpha}} + \boldsymbol{\mu}$, with $\mathsf{L}$ being the lower triangular matrix in the Cholesky decomposition of the covariance matrix, $\boldsymbol{\Sigma} = \mathsf{L}\mathsf{L}^\intercal$, to obtain the following formulation for the evidence:

$$\eta = \int \frac{\int p(\mathcal{D}|\mathsf{L}\widetilde{\boldsymbol{\alpha}} + \boldsymbol{\mu}, M)\, p(\mathsf{L}\widetilde{\boldsymbol{\alpha}} + \boldsymbol{\mu}|M)}{\exp\left(-\frac{1}{2}\widetilde{\boldsymbol{\alpha}}^\intercal \widetilde{\boldsymbol{\alpha}}\right)} \exp\left( -\frac{1}{2} \widetilde{\boldsymbol{\alpha}}^\intercal \widetilde{\boldsymbol{\alpha}} \right) |\mathsf{L}|\, \mathrm{d}\widetilde{\boldsymbol{\alpha}}\,. \tag{103}$$

$\eta$ can now be approximated using Monte Carlo sampling strategy as

$$\eta \approx \frac{1}{N_{LH}} \sum_{k=1}^{N_{LH}} |\mathsf{L}| \frac{\int p(\mathcal{D}|\mathsf{L}\widetilde{\boldsymbol{\alpha}_k} + \boldsymbol{\mu}, M)\, p(\mathsf{L}\widetilde{\boldsymbol{\alpha}_k} + \boldsymbol{\mu}|M)}{\exp\left(-\frac{1}{2}\widetilde{\boldsymbol{\alpha}_k}^\intercal \widetilde{\boldsymbol{\alpha}_k}\right)}, \tag{104}$$

where $\widetilde{\boldsymbol{\alpha}_k}$, $k = 1, \ldots, N_{LH}$, are Latin Hypercube samples [55] drawn from a standard multi-variate normal distribution. For the estimator in Eq. (104) to be accurate, we need good estimates for the posterior mean vector and covariance vector, $\boldsymbol{\mu}$ and $\boldsymbol{\Sigma}$), which can be obtained adaptively using

the iterations:

$$\boldsymbol{\mu}_n = \frac{1}{N_{LH}} \sum_{k=1}^{N_{LH}} \left[ \begin{array}{c} |\mathsf{L}_{n-1}| \frac{p(\mathcal{D}|\mathsf{L}_{n-1}\widetilde{\boldsymbol{\alpha}_k}+\boldsymbol{\mu}_{n-1},M)p(\mathsf{L}_{n-1}\widetilde{\boldsymbol{\alpha}_k}+\boldsymbol{\mu}_{n-1}|M)}{\exp\left(-\frac{1}{2}\widetilde{\boldsymbol{\alpha}_k}^{\mathsf{T}}\widetilde{\boldsymbol{\alpha}_k}\right)} \\ \times(\mathsf{L}_{n-1}\widetilde{\boldsymbol{\alpha}_k}+\boldsymbol{\mu}_{n-1}) \end{array} \right] \tag{105}$$

$$\boldsymbol{\Sigma}_n = \frac{1}{N_{LH}} \sum_{k=1}^{N_{LH}} \left[ \begin{array}{c} |\mathsf{L}_{n-1}| \frac{p(\mathcal{D}|\mathsf{L}_{n-1}\widetilde{\boldsymbol{\alpha}_k}+\boldsymbol{\mu}_{n-1},M)p(\mathsf{L}_{n-1}\widetilde{\boldsymbol{\alpha}_k}+\boldsymbol{\mu}_{n-1}|M)}{\exp\left(-\frac{1}{2}\widetilde{\boldsymbol{\alpha}_k}^{\mathsf{T}}\widetilde{\boldsymbol{\alpha}_k}\right)} \\ \times(\mathsf{L}_{n-1}\widetilde{\boldsymbol{\alpha}_k})(\mathsf{L}_{n-1}\widetilde{\boldsymbol{\alpha}_k})^{\mathsf{T}} \end{array} \right] \tag{106}$$

$$\eta_n = \frac{1}{N_{LH}} \sum_{k=1}^{N_{LH}} |\mathsf{L}_n| \frac{p(\mathcal{D}|\mathsf{L}_n\widetilde{\boldsymbol{\alpha}_k}+\boldsymbol{\mu}_n,M)p(\mathsf{L}_n\widetilde{\boldsymbol{\alpha}_k}+\boldsymbol{\mu}_n|M)}{\exp\left(-\frac{1}{2}\widetilde{\boldsymbol{\alpha}_k}^{\mathsf{T}}\widetilde{\boldsymbol{\alpha}_k}\right)} \tag{107}$$

where $n$ denotes the iteration number. For each individual model, these iterations start with an initial guess for the posterior parameter mean vector and covariance matrix. We obtain those from an initial run of a Markov chain Monte Carlo sampler over the parameter posterior. The iterations stop with a termination criterion on the evidence $\eta$. For this application, the termination criteria is met when the relative change in $\eta$ is less than $10^{-6}$.

#### *3.1.4. Surrogate modeling*

The sampling of the parameters' posterior probability density and the evaluation of the Bayesian model evidence involves many evaluations of the computational model. Since the finite-element based forward model is relatively expensive to query (each tension simulation takes approximately 1 cpu-hour), the inverse problem of parameter estimation and model selection via direct evaluation becomes infeasible. Instead, we construct inexpensive-to-evaluate, accurate surrogates for the response of interest using polynomial chaos expansion (PCE) [56, 57, 58]. Marzouk *et al.* [59] have shown that such surrogates can be effectively constructed using UQ techniques with a presumed uniform density on the parameters' range of interest.

Since rough bounds of each of the parameters can be estimated from the data and knowledge of similar materials, we represent the unknown parameters $\boldsymbol{\theta}$ using a spectral PCE in terms of a set of independent and identically distributed standard uniform random variables $\boldsymbol{\xi} \sim [-1,1]^{d_\theta}$, as in

$$\boldsymbol{\theta}(\boldsymbol{\xi}) = \sum_{i=0}^{P_\theta} \boldsymbol{\theta}_i \Psi_i(\boldsymbol{\xi}), \tag{108}$$

where $d_\theta$ represents the dimensionality of $\boldsymbol{\theta}$, $\Psi_I(\boldsymbol{\xi})$ are the orthogonal PC basis elements (Legendre polynomials in this case), and $P_\theta$ defines the number of terms in the expansion. Eq. (108) is, essentially, a linear transformation that maps standard uniform random variables to the unknown parameters over their range of interest. A corresponding expansion of the model response, acting as a polynomial-based surrogate model, can be written as

$$M(\varepsilon_j;\boldsymbol{\xi}) \approx \sum_{i=0}^{P_M} \sigma_i(\varepsilon_j)\Psi_i(\boldsymbol{\xi}) \ , \tag{109}$$

and is constructed as a function of the physical parameters, $\{E,Y,H,K,B\}$, at each value of engineering strain $\varepsilon_j$ at which data is available. The PC coefficients for the inputs, $\boldsymbol{\theta}_i$, and outputs,

$\sigma_i(\varepsilon_j)$, of the model can be obtained, using one of two approaches: Galerkin projection or stochastic collocation. We utilize a non-intrusive stochastic collocation method with regression [60] to estimate the unknown PC coefficients as it does not require modification of the existing computational models and simulators. Details on this procedure are given in Ref. [55], with an application of PCE surrogate modeling with computationally intensive numerical models in Ref. [61].

## 3.2. Model parameter distributions and aleatoric material uncertainty

Since the CT scans where only able to resolve voids with diameters larger that the 7.5 $\mu$m pixel size and there is evidence [5] that a population of sub-threshold pores exist initially, and can grow and nucleate, we employed a hybrid modelling approach. Specifically, we chose to represent the resolvable pores explicitly in finite element meshes and the sub-threshold pores via damage, an implicit homogenized porosity field governed by an evolution equation. The selected viscoplastic damage constitutive model is described in Refs. [62, 63, 64, 65]. Coupling between the explicit and implicit voids is provided by an "element death" mechanism that allows highly damaged elements to act like voids by no longer contributing to the local stress response and therefore adding to the explicit porosity. For efficiency we only simulate the gauge section with simple tension effected by minimal Dirichlet boundary conditions. To enable sufficient sampling of the porosity realizations and avoid the added complexity of boundary reconstruction schemes, we chose to voxelate the porosity on structured mesh. We set the mesh resolution to be comparable to the CT scan resolution, this aspect will be discussed in more detail in Sec. 3.2.1. Furthermore, the CT scans do not cover the entire gauge section nor the distinct crust and are limited in number, so we created a model, detailed in Sec. 3.2.1, to provide sufficient statistically similar realizations for the uncertainty quantification discussed in Sec. 3.2.4.

Given the observed phenomenology and the need to model a population of sub-threshold voids that may nucleate and growth, we selected an isothermal variant of the Bammann-Chiesa-Johnson (BCJ) viscoplastic damage model [62, 63, 64, 65]. In the context of small strain plasticity appropriate for metals, stress $\boldsymbol{\sigma}$ is given by a linear elastic mixture rule:

$$\boldsymbol{\sigma} = (1-\phi)\mathbb{C}(\boldsymbol{\varepsilon} - \boldsymbol{\varepsilon}_p) \,, \tag{110}$$

based on void fraction $\phi$, where $\mathbb{C}$ is the (isotropic) elastic modulus tensor with components $[\mathbb{C}]_{ijkl} = E/(1+v)\left(v/(1-2v)\delta_{ij}\delta_{kl} + 1/2(\delta_{ik}\delta_{jl} + \delta_{il}\delta_{jk})\right)$ which depends on Young's modulus $E$ and Poisson's ratio $v$. Here $\boldsymbol{\varepsilon}$ is the total strain, $\boldsymbol{\varepsilon}_p$ is the plastic strain, and $\boldsymbol{\varepsilon} - \boldsymbol{\varepsilon}_p$ is the elastic strain. The plastic strain $\boldsymbol{\varepsilon}_p$ evolves according to:

$$\dot{\boldsymbol{\varepsilon}}_p = \sqrt{\frac{3}{2}} f \sinh^n \left( \frac{\sigma/(1-\phi) - \kappa}{Y} - 1 \right) \frac{\mathbf{s}}{\|\mathbf{s}\|} \tag{111}$$

with the isotropic hardening $\kappa$ governed by:

$$\dot{\kappa} = (H - R\kappa)\,\dot{\varepsilon}_p \tag{112}$$

with $\kappa(t=0)=\kappa_0$. Here, $\mathbf{s}=\operatorname{dev}\boldsymbol{\sigma}$ is the deviatoric stress, $\sigma\equiv\sqrt{\frac{3}{2}\mathbf{s}\cdot\mathbf{s}}$ is the von Mises stress, $Y$ is the yield stress, $f$ is the flow coefficient, $n$ is the flow exponent, $H$ is the hardening modulus, $R$ is the recovery coefficient, and $\dot{\varepsilon}_p=\sqrt{2/3\dot{\boldsymbol{\varepsilon}}_p\cdot\dot{\boldsymbol{\varepsilon}}_p}$ is the equivalent plastic strain rate. Recovery is associated with dislocation annihilation and related processes.

The implicit void volume fraction $\phi$ is associated with material damage and is related to void concentration $\eta$ and the average void size $\nu$ by $\phi\equiv\eta\nu/(1+\eta\nu)$. For nucleation, the void concentration $\eta$ (a number density) evolves according to:

$$\dot{\eta}=\left(N_1\left(\frac{2^2}{3^3}-\frac{J_3^2}{J_2^3}\right)+N_3\frac{p}{\sigma}\right)\eta\,\dot{\varepsilon}_p \tag{113}$$

where $p=1/3\,\boldsymbol{\sigma}\cdot\mathbf{I}$ is the pressure, $J_2=1/2\operatorname{tr}\mathbf{s}^2=1/3\,\sigma^2$ and $J_3=1/3\operatorname{tr}\mathbf{s}^3$. The $N_1$ component responds to torsion, and the $N_3$ component corresponds to nucleation due to tension/compression (triaxiality), refer to Ref. [63, Table 2]. The growth of the average void size $\nu$ is given by:

$$\dot{\nu}=\sqrt{\frac{2}{3}}\frac{1+\eta\nu}{\eta}\left((1+\eta\nu)^{m+1}-1\right)\sinh\left(\frac{2(2m-1)}{2m+1}\frac{p}{\sigma}\right)\,, \tag{114}$$

where $m$ is the damage exponent. As shown in Karlson *et al.* [65] and in Brown and Bammann [64], Eq. (114) can be extended to include the effect of newly nucleated voids, assuming them to have volume $\nu_0$:

$$\dot{\nu}=\sqrt{\frac{2}{3}}\frac{1+\eta\nu}{\eta}\left((1+\eta\nu)^{m+1}-1\right)\sinh\left(\frac{2(2m-1)}{2m+1}\frac{p}{\sigma}\right)-(\nu-\nu_0)\frac{\dot{\eta}}{\eta}. \tag{115}$$

Then, Eq. (113) and Eq. (115) can be combined, and using arguments in Brown and Bammann [64] in the limit of vanishing volume of newly nucleated voids, the evolution relation for the void volume fraction (porosity), $\phi$ is obtained:

$$\dot{\phi}=\sqrt{\frac{2}{3}}\dot{\varepsilon}_{\mathrm{p}}\frac{1-(1-\phi)^{m+1}}{(1-\phi)^m}\sinh\left(\frac{2(2m-1)}{2m+1}\frac{p}{\sigma}\right)+(1-\phi)^2\dot{\eta}\nu_0. \tag{116}$$

Lastly, once the void fraction $\phi$ exceeds a threshold $\phi_{\max}$ the material (as discretized by the finite element) is considered completely failed.

#### *3.2.1. Microstructures*

To develop models that are consistent with experimentally-observed failure metrics while accounting for the resolvable porosity, we need a means of generating mesh-based realizations of the visible porosity. Various approaches have previously been proposed in literature to model randomly porous media [66, 67, 68]. We will use a Karhunen-Lóeve expansion (KLE) (see *e.g.* Ref. [69]) to model porous media as a random process through an intermediate Gaussian random process. KLE is a mean-square optimal representation of square-integrable stochastic processes and has been widely-used in many engineering and scientific fields. Much like a Fourier series representation, KLE represents a stochastic process using a linear combination of orthogonal

functions; however, KLE differs from Fourier series in that the coefficients are random variables (as opposed to deterministic scalar quantities) and the basis depends on the correlation function of the process being modeled (as opposed to pre-specified harmonic functions).

In particular, we follow the methodology proposed by Ilango *et al.* [70] to construct KLE models for the porosity process of the core and crust regions. Given the experimental data, we assume that the binary random process modeling porosity $\varphi(\mathbf{x})$ is homogeneous and isotropic [71, 67], with a two-point correlation function given by

$$\mathrm{R}_{\varphi\varphi}(\mathbf{x}_1, \mathbf{x}_2) = \mathbb{E}[\varphi(\mathbf{x}_1)\varphi(\mathbf{x}_2)] = \mathrm{R}_{\varphi\varphi}(r) \tag{117}$$

where $r = \|\mathbf{x}_1 - \mathbf{x}_2\|$ is the distance between positions $\mathbf{x}_1$ and $\mathbf{x}_2$. Under these assumptions, we can approximate the statistics: mean porosity $\bar{\varphi}$ and spatial correlation $\mathrm{R}_{\varphi\varphi}$, as ensemble averages utilizing the available CT scans of the porous media as described in Ref. [67]. Then, with a KLE representation of $\varphi(\mathbf{x})$, we can generate realizations by sampling $\varphi(\mathbf{x})$ on structured mesh covering the nominal gauge section of the tensile specimens and at a resolution commensurate with the CT voxels. Specifically, we generated realizations of these processes on a structured grid $135\times135\times534$ voxels identical to the CT scan with 7.5$\mu$m pixel resolution, where the outer 10 voxels in cross-section were designated as the crust.

Starting with the core region, we obtained a mean porosity of $\bar{\varphi}$= 0.008 and the experimental correlation function $\mathrm{R}_{\varphi\varphi}(r)$ as a function of distance $r$ between voxels. There is noise in the underlying experimental data which is predominantly attributed to (a) a finite sample of specimens being analyzed and (b) the process of obtaining and post-processing CT images. In order to filter out this noise while satisfying physical constraints relating to correlation functions, we fit the data to the widely-used power-exponential correlation function [72, 73]:

$$\mathrm{R}(r) = \exp\left(-\left(\frac{r}{\kappa}\right)^{\nu}\right), \tag{118}$$

where $\kappa > 0$ is the correlation length and $\nu \leq 2$ is a tunable parameter. Calibration of this correlation function to the experimental data resulted in a correlation length $\kappa = 0.0526$mm and power $\nu = 1.122$. In order to capture 99.99% of the energy of the process, the KLE for the core region is truncated at 10,676 terms out of a total of 69,984.

A similar model was constructed for the crust region. Lacking CT data of the crust, we assumed the correlation length of its binary porosity process is approximately the same as that for the core region, with a mean porosity that is ten times of that of the core. This results in a truncated KLE for the intermediate Gaussian process with 32,366 terms to capture 99.99% of the energy of the process.

#### *3.2.2. Calibration parameter selection*

In order to reduce the high dimensionality of the tunable constitutive model parameters $\{E, \nu, Y, \ldots\}$, we fixed a number of parameters based on numerical stability considerations, expert knowledge, and preliminary sensitivity studies. Table 3-1 summarizes the division into parameters that will be calibrated $\boldsymbol{\theta}$ and those that are fixed.

In making this determination, we take the perspective that the basic elastic-plastic parameters $E$, $\nu$, $Y$ represent the well-determined, intrinsic properties of the fully dense, undamaged materials and hence are fixed, pre-determined constants; consequently, we allow other parameters to account for the observed variable response. For instance, we designated the initial damage $\phi_0$ as parameter for calibration to account for variance in the observed effective modulus $\bar{E}$, refer to Table 2-1. Likewise, the initial hardening $\kappa_0$ has a confounding effect in determining the observed yield stress $\sigma_Y$ (refer to Eq. (111)), so it, alone, was allowed to largely determine this feature. Preliminary studies allowed us to set the maximum damage for element death parameter $\phi_{\max}$ at 0.5 to emulate the failure characteristics of the experimental data. We found the model response was not particularly sensitive to this value. Additional preliminary sensitivity studies using Sobol indices ranked the sensitivity of the torsion nucleation parameter $N_1$ orders of magnitude below competing parameters, whereas the sensitivity of the failure features to the triaxiality nucleation parameter $N_3$ was highly ranked; hence, $N_1$ was fixed and $N_3$ was left for calibration.

To specify the initial density $\eta_0$ and initial size at nucleation, $v_0$, of the unresolved voids we took the value $\eta_0 v_0 = 10^{-4}$ for a similar material from [65], estimated $v_0 = 0.1\ \mu\text{m}^3$ based on the size of the CT voxels ($421.5\ \mu\text{m}^3$), and arrived at $\approx 30$ voids per finite element. This population is sufficient to satisfy the basic premise of the damage model, *i.e.* that there is an ensemble of uncorrelated voids present.

The remaining parameters, flow exponent $n$, damage exponent $m$, flow coefficient $f$ were fixed at published values, see *e.g.* Ref. [65]; preliminary studies showed that the response was relatively insensitive to $f$ as well.

Physical reasoning and accepted values for similar materials were used to center the calibration parameters $\boldsymbol{\theta} = \{R, H, \kappa_0, \phi_0, N_3\}$. Both the hardening $H$ and recovery $R$ parameters were included in this set to capture the range of post yield slopes and maximum stresses observed in the data (refer to Eq. (112)). The ranges of the calibration parameters were obtained through an iterative process involving the bounds of parameter space explored by the Monte Carlo sampler described in Sec. 3.2.4.

### *3.2.3. Surrogate model*

To calibrate likely values for the parameters $\boldsymbol{\theta}$ given the experimental data, we will use Bayesian model calibration techniques developed in Sec. 3.2.4. This statistical inversion relies on the joint sampling of the posterior probability density function (PDF) of the parameters $\boldsymbol{\theta}$ using Markov chain Monte Carlo (MCMC) sampling-based strategies. The joint characterization of the posterior parameter PDF of 5 independent parameters usually requires at least $10^6$ samples, where each sample is forward model simulation of the computationally-intensive finite element model. One popular strategy that reduces this computational burden relies on surrogate models of the response of the expensive physical simulations. Such surrogates capture the complex, often nonlinear, mapping from the unknown parameters $\boldsymbol{\theta}$ to observable, system outputs $\mathcal{F}$ are relatively cheap to evaluate an are of sufficient accuracy.

In a previous study [1], we employed a polynomial chaos expansion (PCE) [56, 57] to construct surrogates over the domain of plausible values of unknown parameters. Such methodology

| Parameter | | Value |
|---|---|---|
| Young's modulus (GPa) | $E$ | 240 |
| Poisson's ratio | $\nu$ | 0.27 |
| Yield strength (MPa) | $Y$ | 600 |
| Initial void size ($\mu$m$^3$) | $\nu_0$ | 0.1 |
| Initial void density ($\mu$m$^{-3}$) | $\eta_0$ | $10^{-3}$ |
| Flow exponent | $n$ | 10 |
| Damage exponent | $m$ | 2 |
| Torsion nucleation | $N_1$ | 10 |
| Flow coefficient | $f$ | 10 |
| Maximum damage | $\phi_{\max}$ | 0.5 |
| Isotropic dynamic recovery | $R$ | [0.1,10] |
| Isotropic hardening (GPa) | $H$ | [2,10] |
| Initial hardening (MPa) | $\kappa_0$ | [200,600] |
| Initial damage | $\phi_0$ | [0.0001,0.2] |
| Triaxiality nucleation | $N_3$ | [5,15] |

**Table 3-1 Parameter values for fixed parameters (upper) and ranges for calibration parameters (lower) $\boldsymbol{\theta} = \{R, H, \kappa_0, \phi_0, N_3\}$.**

exploits global polynomial basis which non-optimal for capturing strongly nonlinear input-output mappings. Specifically, PCE surrogates require higher-order basis to capture the nonlinearities accurately, implying an exponential growth in the number of unknown PCE coefficients to tune (proportional to number of forward model simulations required to calibrate such surrogates). We first attempted the construction of third-order PCE surrogates in the 5-dimensional parameter space. The PCE coefficients were obtained using Galerkin projection utilizing 241 simulations corresponding to quadrature points obtained using Smolyak's sparse tensorization and nested Clenshaw-Curtis quadrature formula. The accuracy was measured using normalized root-mean-square error with 100 additional simulations corresponding to Monte Carlo samples in parameter space. Such surrogates were exhibiting slow convergence against increasing PCE order from 1 through 3, with the 4-th order PCE surrogates requiring a prohibitive 801 simulations.

Instead, we chose to utilize Radial Basis Functions (RBF) [74, 75, 76], being one of the most capable multidimensional approximation methods [77], to construct surrogate response models for each physical feature $\mathcal{F}$ as a function of the calibration parameters $\boldsymbol{\theta}$. For each porosity realization constructed using the methodology outlined in Sec. 3.2.1, we fit 6 RBF surrogates corresponding to the 6 features of interest $\mathcal{F}$ reported in Table 2-1. Generally, one could construct one global surrogate per feature to cover the space of KLE coefficients used in modeling the explicit porosity process as well as the unknown parameters, but we opted against that approach due to the extremely high-dimensionality of the KLE coefficient space (see Sec. 3.2.1 for details). We start with a set of parameter points $\boldsymbol{\theta}_i$, $i = 1, \ldots, n$, and corresponding feature values, $f_i = f(\boldsymbol{\theta}_i)$ for each feature $f$ in $\mathcal{F}$. The RBF approximation, $f \approx \tilde{f}(\boldsymbol{\theta})$, is a linear combination of basis functions (kernels) that depend on the distances between the evaluation point, $\boldsymbol{\theta}$, and a set of

kernel centers, $\boldsymbol{\theta}_J$, $J = 1, \ldots, M$ given by

$$\tilde{f}(\boldsymbol{\theta}) = \sum_{J=1}^{M} c_J \mathcal{K}(\|\boldsymbol{\theta} - \boldsymbol{\theta}_J\|_2) \tag{119}$$

where $\|\cdot\|$ denotes the Euclidean norm, and coefficients $c_J$ are to be determined. Widely-used kernels include Gaussian, $\mathcal{K}(r) = e^{-(\varepsilon r)^2}$, multiquadric, $\mathcal{K}(r) = \sqrt{1 + (\varepsilon r)^2}$, and cubic, $\mathcal{K}(r) = r^3$, where $\varepsilon$ is a tunable parameter. (See [78] for a more complete list of RBF kernels.) After preliminary comparative investigations (results omitted for brevity), we chose to utilize Gaussian kernels, since they lead to the least cross-validation errors in our context.

In many applications, the centers are chosen to be the data points $\{\boldsymbol{\theta}_J\} = \{\boldsymbol{\theta}_i\}$, with $M = n$. The constants, in that setting, may be determined by ensuring that the approximation will exactly match the given data at the data points, leading to an interpolative approximation function. In this realistic application, the features extracted from the simulations are corrupted by relatively small, yet significant, noise relating to feature-extraction from stress-strain curves sampled at a finite set of strain values. In other words, the true value $f_i$, corresponding to parameter realization $\boldsymbol{\theta}_i$, is known only up to a small amount of unknown noise. In that case, an interpolative RBF approximation would be equivalent to fitting the unknown noise along with the underlying feature. More generally, over-fitting leads to erroneous surrogates even in the noise-free case due to parameter identifiability issues.

To alleviate the issue of over-fitting the noise in the extracted features, we will choose to have the number of centers to be less than the number of available data points, *i.e.* $M < n$. An added advantage of a smaller choice for the number of centers than available data points is the reduced cost to evaluate the trained RBF surrogates. The number of centers $M$ and their locations, being a modeling choice, will be chosen using cross-validation. Both sets of data points and centers for RBF surrogate construction will be obtained using latin hypercube sampling (LHS) [79], resulting in a sample that is predominantly random, but is uniform in each separate dimension. Although more optimal strategies exist for choosing the data points and centers adaptively (see [80] for example), we chose this space-filling design that can be used for purposes beyond the RBF surrogate construction.

For each porosity realization, we run $n = 200$ forward model simulations at a set of corresponding LHS samples in parameter space with parameter ranges given in Table 3-1.

### *3.2.4. Bayesian calibration*

In this section we develop a combined treatment of the aleatoric uncertainties related to the explicit porosity configurations and epistemic uncertainties of the material parameters uncertainties. The procedure involves an ensemble of mesh-based realizations of the observable porosity $\varphi = \{\varphi_I\}$ and marginalization over the resulting response surrogates. We separate the parameters into three categories: (a) the high dimensional porosity as represented by the realizations $\varphi$ controlled by the KLE parameters $\boldsymbol{\xi}$, (b) the physical parameters of interest including the "embedded" error/beta distributions for a subset of the parameters $\boldsymbol{\theta}$, and (c) the

hyper parameters for the additive uncorrelated measurement noise intensities $\boldsymbol{\gamma}$. The corresponding model of the experimental data $D$ is

$$f_{aI}(\boldsymbol{\theta},\boldsymbol{\gamma}) = \tilde{f}_a(\boldsymbol{\theta};\varphi_I) + \eta_a(\boldsymbol{\gamma}_a) \tag{120}$$

where $\tilde{f}_a$ is the surrogate model for feature $f_a$ given porosity realization $\varphi_I$ and $\eta_a$ is the corresponding independent additive noise with parameters $\boldsymbol{\gamma}_a$. The data $D$ is comprised of all the feature $\mathcal{F}$ measurements across all the experimental tests of individual specimens.

Generally speaking, the statistical calibration of models using experimental data involves inferring a set of unknown, or weakly known, parameters. Oftentimes, a subset of those parameters may not be directly relevant for subsequent analysis (such as sensitivity analysis or forward propagation of uncertainty). Such parameters, termed "nuisance" parameters, are still important in the calibration process and are thus jointly inferred with the parameters of interest. The parameters $\boldsymbol{\gamma}$ determining the measurement noise $\eta$ are a common example of this kind of parameter.

In this subsection, we describe how we deal with a different kind of nuisance parameter vector, the observable porosity field $\varphi(\mathbf{x})$, which is used to represent the high-dimensional random process that acts as an uncontrollable source of uncertainty in the physical system, *i.e.* the location and sizes of voids. In UQ terms, such source of uncertainty contributes to *aleatory* uncertainty [81], arising from the inherent variability of a phenomenon (in this case the random porosity distribution) and cannot be further reduced from the available data (*i.e.* when making predictions we cannot rely on knowing the locations of voids). In contrast, the unknown parameter vector $\boldsymbol{\theta}$ of interest contributes to to epistemic uncertainty [81] arising from incomplete knowledge of the phenomenon and can be reduced with the available data $D$. In this context, both types of uncertainty have probabilistic characterization. However, modelers utilizing UQ techniques make this distinction as the two types of uncertainties require separate treatment in a Bayesian setting (see [82] for a philosophical discussion on the need to separate sources of uncertainties in this fashion).

In such setting, one performs joint inference of the uncertain parameters and nuisance parameters. The joint posterior PDF of the uncertain parameter vector $\boldsymbol{\theta}$ and nuisance parameter vector $\varphi$ is first decomposed using the probabilistic chain rule:

$$p(\boldsymbol{\theta},\varphi\,|\,D) = p(\boldsymbol{\theta}\,|\,D,\varphi)\,p(\varphi\,|\,D)\ . \tag{121}$$

The second term on the right hand side of Eq. (121) is the marginal PDF of $\varphi$ conditional on the data vector $D$. We will assume that $\varphi$ is independent of the available data $D$ which describes features of the stress-strain response of individual test specimens. In other words, the available stress-strain data does not inform the porosity distribution and hence $\varphi$ is classified as a source of aleatory uncertainty. With this assumption, we replace $p(\varphi\,|\,D)$ with a pre-specified PDF $\pi(\phi)$ which leads to:

$$p(\boldsymbol{\theta},\varphi\,|\,D) = p(\boldsymbol{\theta}\,|\,D,\varphi)\,\pi(\varphi)\ . \tag{122}$$

In our context $\pi(\phi)$ is determined by the KLE described in Sec. 3.2.1 tuned to the experimental average porosity and spatial correlation.

We are interested in the posterior PDF for the parameter vector of interest, namely $\boldsymbol{\theta}$. We can obtain this PDF by marginalizing the joint PDF in Eq. (122) over $\varphi$

$$\begin{aligned} p(\boldsymbol{\theta}\,|\,D) &= \int p(\boldsymbol{\theta},\varphi\,|\,D)\ \mathrm{d}\varphi \\ &= \int p(\boldsymbol{\theta}\,|\,D,\varphi)\,\pi(\varphi)\ \mathrm{d}\varphi \end{aligned} \tag{123}$$

In general, the marginalized posterior PDF in Eq. (123) does not have an analytical solution and one must resort to deterministic or stochastic schemes of numerical integration in practice. One conceptually simple approach utilizes Monte Carlo (stochastic) integration method to arrive at the following approximation for the marginalized posterior $\widehat{p}(\boldsymbol{\theta}\,|\,D)$:

$$p(\boldsymbol{\theta}\,|\,D) \approx \widehat{p}(\boldsymbol{\theta}\,|\,D) = \sum_{I=1}^{N_{\mathrm{MC}}} p(\boldsymbol{\theta}\,|\,D,\varphi_I) \tag{124}$$

with $\varphi_I$ denoting independent samples of $\varphi$ drawn from $\pi(\varphi)$. Bayes' law can be applied to Eq. (123), resulting in:

$$\widehat{p}(\boldsymbol{\theta}\,|\,D) \propto \frac{1}{N_{\mathrm{MC}}} \sum_{I=1}^{N_{\mathrm{MC}}} p(D\,|\,\boldsymbol{\theta},\varphi_I)\,p(\boldsymbol{\theta}\,|\,\varphi_I)\ . \tag{125}$$

The first and second terms inside the summation in Eq. (125) correspond to the likelihood and prior of the parameter vector $\boldsymbol{\theta}$, respectively, both conditional on the specific realization of nuisance parameter vector $\varphi_I$. Without loss of generality, we make the assumption that the parameters of interest are independent of the nuisance parameters, prior to the assimilation of data. That is, the prior PDF of the $\boldsymbol{\theta}$ does not depend on $\varphi$. Eq. (125) can then be rewritten as:

$$\begin{aligned} \widehat{p}(\boldsymbol{\theta}\,|\,D) &\propto \frac{1}{N_{\mathrm{MC}}} \sum_{I=1}^{N_{\mathrm{MC}}} p(D\,|\,\boldsymbol{\theta},\varphi_I)\,p(\boldsymbol{\theta}) \\ &= \left[\frac{1}{N_{\mathrm{MC}}} \sum_{I=1}^{N_{\mathrm{MC}}} p(D\,|\,\boldsymbol{\theta},\varphi_I)\right] p(\boldsymbol{\theta})\ . \end{aligned} \tag{126}$$

Eq. (126) provides a Monte Carlo approximation to the marginalized posterior of the parameter vector $\boldsymbol{\theta}$ which, in turn, relies on a Monte Carlo approximation to the *marginalized likelihood* of $\boldsymbol{\theta}$ (given in square brackets). Such likelihood can be thought as an *average* likelihood for the parameter vector $\boldsymbol{\theta}$ over all possible realizations of $\varphi$. Since the $\varphi$ parameter space is high-dimensional in our context (on the order of 10,000 parameters, refer to Sec. 3.2.1), the Monte Carlo approximation is the only feasible one available. To further expedite the process, we will fix sample $\varphi$ once to obtain a fixed ensemble of realizations $\varphi_I$, $I = 1,\ldots,N_{\mathrm{MC}}$. This allows us to construct $N_{\mathrm{MC}}$ PC-based surrogates for the observable quantities in terms of the unknown parameters $\boldsymbol{\theta}$, one for each realization of the porosity $\varphi$. Such surrogates would expedite the marginalized likelihood evaluation in Eq. (126), which is subsequently sampled using MCMC sampling procedure.

# 4. MACHINE LEARNING MODELS OF MICROSTRUCTURAL RESPONSE

In this section we describe means of constructing neural network models via classical representation theory and that incorporate the details of initial microstructure in order to predict specific response.

## 4.1. Representations the mean response

Here, we provide a concise overview of representation theory and how we apply it in the context of constitutive modeling by (artificial) neural networks (NNs). Specifically, we employ a generalization of the Tensor Basis Neural Network (TBNN) [83] concept based on an understanding of classical representation theory. With it we construct models that represent the selected output as a function of inputs with complete generality and compact simplicity. This construction is distinct from the predominance of component-based NN constructions, for example those mentioned in the Introduction, in that basic symmetries, such as frame invariance are built in to the representation and do not need to be learned.

### *4.1.1. Representation theory*

Representation theorems for functions of tensors have a foundation in group theory [84, 85, 86, 87] with the connection being that symmetry is described as functional invariance under group action. In mechanics, the relevant invariance under group action are rotations (and translations) of the coordinate system, which is known as *material frame indifference*, *invariance under super-posed rigid body motions* or simply *objectivity*. This is a fundamental and exact symmetry. Practical applications of representation theory to mechanics are given in Truesdell and Noll's monograph [88, Sec. 7-13] and Gurtin's text [89, Sec. 37] and address complete, irreducible representations of general functions of physical vector and tensor arguments. For example, the scalar function $f(\mathbf{A})$ of a (second order) tensor $\mathbf{A}$ is invariant if

$$f(\mathbf{A}) = f(\mathbf{G}\mathbf{A}\mathbf{G}^T) \ , \tag{127}$$

and a (second order) tensor-valued function $\mathbf{M}(\mathbf{A})$ is objective if

$$\mathbf{G}\mathbf{M}(\mathbf{A})\mathbf{G}^T = \mathbf{M}(\mathbf{G}\mathbf{A}\mathbf{G}^T) \ , \tag{128}$$

for every member $\mathbf{G}$ of the orthogonal group.

Underpinning the representations of $f$ and $\mathbf{M}$ are a number of theorems. The *spectral theorem* states that any *symmetric* second order tensor $\mathbf{A}$ has spectral representation :

$$\mathbf{A} = \sum_{i=1}^{3} \lambda_i \mathbf{a}_i \otimes \mathbf{a}_i \ , \tag{129}$$

composed of its eigen-values $\{\lambda_i\}$ and eigen-vectors $\{\mathbf{a}_i\}$ where $i = 1,3$. The spectral representation of $\mathbf{A}$ makes powers of $\mathbf{A}$ take a simple form: $\mathbf{A}^n = \sum_i \lambda_i^n \mathbf{a}_i \otimes \mathbf{a}_i$ (and in particular $\mathbf{A}^0 \equiv \mathbf{I}$). The equally important Cayley-Hamilton theorem states that the tensor $\mathbf{A}$ satisfies its characteristic equation :

$$\mathbf{A}^3 - \underbrace{(\lambda_1+\lambda_2+\lambda_3)}_{J_1=\mathrm{tr}\,\mathbf{A}}\mathbf{A}^2 + \underbrace{(\lambda_1\lambda_2+\lambda_2\lambda_3+\lambda_3\lambda_1)}_{J_2=\frac{1}{2}\left(\mathrm{tr}^2\mathbf{A}-\mathrm{tr}\,\mathbf{A}^2\right)}\mathbf{A} - \underbrace{(\lambda_1\lambda_2\lambda_3)}_{J_3=\det\mathbf{A}}\mathbf{I} = \mathbf{0}\ , \tag{130}$$

where $\{J_i\}$ are the *principal (scalar) invariants* of $\mathbf{A}$. The (generalized) Rivlin's identities [90, 91] provide similar relations for multiple tensors and their joint invariants.

Scalars that respect Eq. (127), such as $\{J_i\}$, are called *scalar invariants* and are formed from (polynomials or, more generally, functions of) the eigenvalues of $\mathbf{A}$. Hence, $f(\mathbf{A})$ reduces to

$$f(\mathbf{A}) = f(I) \tag{131}$$

where $I$ is a set of scalar invariants of $\mathbf{A}$, and hence $f$ is also an invariant. A set of invariants $I$ is considered *irreducible* if each of its elements cannot be represented in terms of others and conveys a sense of completeness and simplicity. Since the eigenvalues $\{\lambda_i\}$ are costly to compute, typically traces such as $\{\mathrm{tr}\,\mathbf{A}, \mathrm{tr}\,\mathbf{A}^2, \mathrm{tr}\,\mathbf{A}^3\} = \{\sum_i \lambda_i, \sum_i \lambda_i^2, \sum_i \lambda_i^3\}$ are employed as scalar invariants. Joint invariants of a functional basis for multiple arguments are formed with the help of Pascal's triangle.

For tensor-valued functions such as $\mathbf{M}(\mathbf{A})$ in Eq. (128), a power series representation

$$\mathbf{M}(\mathbf{A}) = \sum_{i=0}^{\infty} c_i(I)\mathbf{A}^i \tag{132}$$

is a good starting point. The coefficient functions $c_i$ are represented in terms of scalar invariants as in Eq. (131). This power series representation can be reduced by application of the Cayley-Hamilton theorem (130), in the recursive form $\mathbf{A}^{j+3} = J_1\mathbf{A}^{j+2} - J_2\mathbf{A}^{j+1} + J_3\mathbf{A}^j$. The *transfer theorem* (as referred to by Gurtin [89, Sec. 37]) states that isotropic functions such as $\mathbf{M}(\mathbf{A})$ inherit the eigenvalues of their arguments and implies the fact that these functions are co-linear with their arguments. Also Wang's lemma ($\mathbf{I}, \mathbf{A}, \mathbf{A}^2$ span the space of all tensors co-linear with $\mathbf{A}$) is a consequence of Eq. (129) and Eq. (130), and gives a sense of completeness of the representation:

$$\mathbf{M}(\mathbf{A}) = c_0(I)\mathbf{I} + c_1(I)\mathbf{A} + c_2(I)\mathbf{A}^2\ . \tag{133}$$

Eq. (133) evokes the general representation for a symmetric tensor function of an arbitrary number of arguments in terms of a sum of scalar coefficient functions multiplying the corresponding elements of the tensor basis. The general methodology for constructing the functional basis to represent scalar functions is given in Rivlin and Ericksen [92], and the corresponding methodology to construct tensor bases is developed in Wang [93, 94].

Representation theory, like machine learning, does not determine the *appropriate* arguments/inputs and output for the constitutive functions. In mechanics, there is a certain amount of fungibility to both. For instance, the (spatial) Cauchy stress can easily be transformed into the (referential) first Piola-Kirchhoff stress, and left and right Cauchy-Green stretch have same

eigenvalues but different eigen-bases. Also, any of the Seth-Hill/Doyle-Ericksen strain family [95, 96, 97] provide equivalent information on deformation, and any of the objective rates formed from Lie derivatives [98, 99, 100, 101] provide equivalent measures of rate of deformation; however, some choices of arguments and output lead to greater simplicity than others.

Lastly, it is important to note that isotropic functions are not restricted to isotropic responses. The addition of a structure tensor characterizing the material symmetry to the arguments allows isotropic function theory to be applied so that the joint invariants encode anisotropies [102, 103, 104, 105, 106, 107].

#### *4.1.2. Plasticity*

Briefly, plasticity is an inelastic, history-dependent process due to dislocation motion or other dissipative phenomena. We assume the usual multiplicative decomposition [108, 109] of the total deformation gradient $\mathbf{F}$ into elastic (reversible) $\mathbf{F}_e$ and plastic (irreversible) $\mathbf{F}_p$ components

$$\mathbf{F} = \mathbf{F}_e \mathbf{F}_p \ . \tag{134}$$

As a consequence, the velocity gradient in the current configuration, $\mathbf{l} \equiv \dot{\mathbf{F}}\mathbf{F}^{-1}$, can be additively decomposed into elastic and plastic components :

$$\mathbf{l} = \dot{\mathbf{F}}_e \mathbf{F}_e^{-1} + \mathbf{F}_e \underbrace{\dot{\mathbf{F}}_p \mathbf{F}_p^{-1}}_{\mathbf{L}_p} \mathbf{F}_e^{-1} \ , \tag{135}$$

refer to [110, Sec. 8.2]. The assumption that $\mathbf{F}_p$ is pure stretch (no rotation) reduces $\mathbf{L}_p$ to $\mathbf{D}_p = \operatorname{sym} \mathbf{L}_p$. The elastic deformation determines the stress, for instance the Cauchy stress $\mathbf{T}$:

$$\mathbf{T} = \hat{\mathbf{T}}(\mathbf{F}_e) = \mathbf{T}(\mathbf{e}_e) \ , \tag{136}$$

and the evolution of the plastic state is determined by a *flow rule*, *e.g.* :

$$\dot{\mathbf{F}}_p = \mathbf{D}_p \mathbf{F}_p \ \text{ where } \ \mathbf{D}_p = \hat{\mathbf{D}}_p(\mathbf{F}_p, \mathbf{T}) = \mathbf{D}_p(\mathbf{b}_p, \boldsymbol{\sigma}) \ , \tag{137}$$

where $\mathbf{F}_p$ quantifies the plastic state and $\mathbf{T}$ the driving stress. Invariance allows the reduction of the argument of $\mathbf{T}$ to, for example, the objective, elastic Almansi strain $\mathbf{e}_e = \frac{1}{2}\left(\mathbf{I} - \mathbf{b}_e^{-1}\right)$ based on the left Cauchy-Green/Finger stretch tensor $\mathbf{b}_e = \mathbf{F}_e \mathbf{F}_e^T$. Similarly, the state variable in the flow rule can be reduced by applying invariance, for example, $\mathbf{b}_p = \mathbf{F}_p \mathbf{F}_p^T$. The driving stress can be attributed to the deviatoric part of the pull-back of the Cauchy stress $\mathbf{T}$: $\boldsymbol{\sigma} = \operatorname{dev}\left[\mathbf{F}_e^{-1}\mathbf{T}\mathbf{F}_e^{-T}\right]$ which is also invariant and also coexists in the intermediate configuration with $\mathbf{D}_p$. Furthermore, a deviatoric tensor basis element, such at $\boldsymbol{\sigma}$, generates an isochoric flow which respects plastic incompressibility $\det \mathbf{F}_p \equiv 1$. Other choices of the inputs and outputs of the stress and flow functions are discussed in Results section. Typically both the stress and flow are derived potentials to ensure elastic energy conservation for the stress and associative flow for the flow rule; however, in this work we to allow for a more general flow and non-differentiable NN model. (Experiments typically cannot measure potentials directly).

A few basic properties are built into traditional empirical models that need to be learned in typical NN models. First, zero strain, $\mathbf{e}_e = \mathbf{0}$, implies zero stress :

$$\mathbf{T}(\mathbf{0}) = \mathbf{0} \,, \tag{138}$$

and, likewise, zero driving stress should result in zero plastic flow :

$$\mathbf{D}_p(\mathbf{F}_p, \mathbf{0}) = \mathbf{0} \,. \tag{139}$$

Also there is a dissipation requirement for the plastic flow. Generally speaking, the Coleman-Noll [111] argument, together with the first and second law of thermodynamics, applied to a free energy in terms of the elastic deformation and a plastic history variable results in: (a) the stress being conjugate to the elastic strain rate, and (b) the internal, plastic state variable, when it evolves, reduces the free energy via $\mathbf{M} \cdot \mathbf{L}_p \geq 0$ where $\mathbf{M}$ is the Mandel stress

$$\mathbf{M} = \det(\mathbf{F}) \left[\mathbf{F}_e^T \mathbf{F}_e\right] \left[\mathbf{F}^{-1} \mathbf{T} \mathbf{F}^{-T}\right] \tag{140}$$

This reduces to

$$\mathbf{T} \cdot \mathbf{d}_p \geq 0 \,, \tag{141}$$

refer to Ref. [110, Sec. 8.2]. Also, given the physics of dislocation motion, it is commonly assumed that the plastic deformation is incompressible, $\det \mathbf{F}_p = 1$, which implies the flow is deviatoric

$$\operatorname{tr} \mathbf{D}_p = 0 \tag{142}$$

For more details see the texts Refs. [110, 112, 113].

## 4.2. Application to neural network constitutive modeling

We generalize the Tensor Basis Neural Network (TBNN) formulation [83] to build NN representations for the stress relation, Eq. (136), and the plastic flow rule, Eq. (137), that embed a number of symmetries and constraints. Both $\mathbf{T}$ and $\mathbf{D}_p$ are required to be isotropic functions of their arguments by invariance. As discussed, classical representation theorems give the general form

$$\mathbf{f}(\mathcal{A}) = \sum_i f_i(I)\, \mathbf{B}_i \,, \tag{143}$$

where $\mathcal{A} \equiv \{\mathbf{A}_1, \mathbf{A}_2, \ldots\}$ are the pre-supposed dependencies/arguments of function $\mathbf{f}$, $I \equiv \{I_j\}$ is an (irreducible) set of scalar invariants of $\mathcal{A}$, and $\mathcal{B} = \{\mathbf{B}_j\}$ is the corresponding tensor basis. In Eq. (143), only the scalar coefficient functions are $\{f_i\}$ are unknown once the inputs have been selected and hence they are represented with a dense NN using the selected scalar invariants $I$ as inputs embedded in the overall TBNN structure. In the TBNN framework, the sum the NN functions $\{f_i(I)\}$ and the corresponding tensor basis elements $\{\mathbf{B}_i\}$ in Eq. (143) is accomplished by a so-called *merge layer*, and the functions $\{f_i\}$ are trained simultaneously (refer to Fig. 4-1 and more details will be given in Sec. 4.2.1). This formulation is in contrast to the standard, component-wise NN formulation:

$$\mathbf{f}(\mathcal{A}) = \sum_{i,j} f_{ij}([\mathbf{A}_1]_{ij}, [\mathbf{A}_2]_{ij}, \ldots)\, \mathbf{e}_i \otimes \mathbf{e}_j \,, \tag{144}$$

which is based on components of both the inputs $\{\mathbf{A}_1, \mathbf{A}_2, \ldots\}$ and the output $\mathbf{f}$.

For the stress, we assume a single symmetric tensor input selected from the Seth-Hill/Doyle-Ericksen elastic strain family, in particular $\mathbf{e}_e$, is sufficient, so that representation Eq. (133):

$$\mathbf{T} = \sigma_0(I)\mathbf{I} + \sigma_1(I)\mathbf{e}_e + \sigma_2(I)\mathbf{e}_e^2 \,, \tag{145}$$

is appropriate. Despite this formulation being based on strain, versus stretch, it does not embed the zero stress property, Eq. (138), and, hence, $\sigma_0(I)$ will need to learn that zero strain implies zero stress. Since we prefer to impose, rather than learn, physical constraints such as Eq. (138) since this reduces the necessary training data [83] and the exact satisfaction leads to conservation and other properties necessary for stability, *etc.* Exact satisfaction of Eq. (138) can accomplished a few different ways: (a) shifting the basis with the Cayley-Hamilton theorem (130)

$$\mathbf{T} = \sigma_1\mathbf{e}_e + \sigma_2\mathbf{e}_e^2 + \sigma_3\mathbf{e}_e^3 \,, \tag{146}$$

refactoring (b) some $\mathbf{T} = \left(I_2\sigma_0'\right)\mathbf{I} + \sigma_1'\mathbf{e}_e + \sigma_2'\mathbf{e}_e^2$, or (c) all $\mathbf{T} = I_2\left(\sigma_0''\mathbf{I} + \sigma_1''\mathbf{e}_e + \sigma_2''\mathbf{e}_e^2\right)$ of the coefficient functions $\{\sigma_i\}$ with $I_2 = \operatorname{tr}\mathbf{e}_e^2$. In general, any of these representations can be expressed on the spectral basis

$$\mathbf{T} = \sum_i \sum_{j=1}^{3} \sigma_i \lambda_j^i \mathbf{a}_j \otimes \mathbf{a}_j = \sum_{j=1}^{3} \left( \sum_i \sigma_i \lambda_j^i \right) \mathbf{a}_j \otimes \mathbf{a}_j \tag{147}$$

so there is a (weak) equivalence between coefficient functions of the various representations. Here, $\mathbf{e}_e = \sum_i \lambda_i \mathbf{a}_i \otimes \mathbf{a}_i$.

As mentioned, we assume that the inputs to the flow rule are (a) a history variable $\mathbf{b}_p$, and (b) driving stress $\boldsymbol{\sigma}$. A general function representation from classical theory for an isotropic function of two (symmetric) tensor arguments requires ten invariants [90] (see also [114, Ch.3, Eq. 9 and 11]):

$$I \equiv \{I_i\} = \{\operatorname{tr}\mathbf{b}_p, \operatorname{tr}\mathbf{b}_p^2, \operatorname{tr}\mathbf{b}_p^3, \operatorname{tr}\boldsymbol{\sigma}, \operatorname{tr}\boldsymbol{\sigma}^2, \operatorname{tr}\boldsymbol{\sigma}^3, \operatorname{tr}\mathbf{b}_p\boldsymbol{\sigma}, \operatorname{tr}\mathbf{b}_p^2\boldsymbol{\sigma}, \operatorname{tr}\mathbf{b}_p\boldsymbol{\sigma}^2, \operatorname{tr}\mathbf{b}_p^2\boldsymbol{\sigma}^2\} \tag{148}$$

and eight tensor generators/basis elements

$$\mathcal{B} \equiv \{\mathbf{B}_i\} = \{\mathbf{I}, \mathbf{b}_p, \mathbf{b}_p^2, \boldsymbol{\sigma}, \boldsymbol{\sigma}^2, \operatorname{sym}\mathbf{b}_p\boldsymbol{\sigma}, \operatorname{sym}\mathbf{b}_p^2\boldsymbol{\sigma}, \operatorname{sym}\mathbf{b}_p\boldsymbol{\sigma}^2\} \,, \tag{149}$$

where $\operatorname{sym}\mathbf{A} \equiv \frac{1}{2}(\mathbf{A} + \mathbf{A}^T)$. To satisfy the zero flow condition, Eq. (139), we can shift basis for the second, stress argument and eliminate all basis elements solely dependent on the first, plastic state argument:

$$\mathcal{B} = \{\boldsymbol{\sigma}, \boldsymbol{\sigma}^2, \boldsymbol{\sigma}^3, \operatorname{sym}\mathbf{b}_p\boldsymbol{\sigma}, \operatorname{sym}\mathbf{b}_p^2\boldsymbol{\sigma}, \operatorname{sym}\mathbf{b}_p\boldsymbol{\sigma}^2\} \,. \tag{150}$$

Plastic incompressibility, in the form of deviatoric plastic flow, Eq. (142), can imposed by applying the linear operator dev, $\operatorname{dev}\mathbf{A} = \mathbf{A} - \frac{1}{3}\operatorname{tr}(\mathbf{A})\mathbf{I}$,

$$\begin{aligned}\mathbf{D}_p = {} & f_{01}\operatorname{dev}\boldsymbol{\sigma} + f_{11}\operatorname{sym}\operatorname{dev}\mathbf{b}_p\boldsymbol{\sigma} + f_{02}\operatorname{dev}\boldsymbol{\sigma}^2 \\ & + f_{21}\operatorname{dev}\operatorname{sym}\mathbf{b}_p^2\boldsymbol{\sigma} + f_{12}\operatorname{dev}\operatorname{sym}\mathbf{b}_p\boldsymbol{\sigma}^2\end{aligned}$$

Dissipation of plastic flow can be strictly imposed by requiring that the flow be directly opposed to the stress in Eq. (141) which implies:

$$\mathbf{D}_p = f_1\,\boldsymbol{\sigma} + f_3\,\boldsymbol{\sigma}^3 \ , \tag{151}$$

and $f_1(I) > 0$ and $f_3(I) > 0$. In this study we will rely on the learning process to ensure the positivity of the coefficient functions $f_1$ and $f_3$ but this could be accomplished exactly with the Macauley bracket (ramp function) applied to $f_1$ and $f_3$, for example.

We train the NN models of plasticity with data from two traditional plasticity models. In this section we give details of (a) the traditional models, (b) the training of the NNs, and (c) numerical integration of the TBNN plasticity model.

In an exploration of the fundamental properties of NNs applied to plasticity, we seek to represent responses of two models: (a) a poly-crystalline representative volume element (RVE) with grain-wise crystal plasticity (CP) response (an *unknown* closed form model since the poly-crystalline aspect of the CP model obscures its closed form), and (b) a simple visco-plasticity (VP) material point (a *known* closed form model). Both are finite deformation models so that invariance and finite rotation are important; and both are visco-plastic in the sense of lacking a well-defined yield surface and strictly dissipative character.

Briefly, crystal plasticity (CP) is a well-known meso-scale model of single crystal deformation. Here we use crystal plasticity to prescribe the response of individual crystals in a perfectly bonded polycrystalline aggregate. The theoretical development of CP is described in Refs. [115, 116, 117, 118, 119] and the computational aspects in reviews [120, 121].

Specifically, for the crystal elasticity, we employ a St. Venant stress rule formulated with the second Piola-Kirchhoff stress mapped to the current configuration

$$\mathbf{T} = \frac{1}{\det\mathbf{F}}\mathbf{F}\left(\mathbb{C}\mathbf{E}_e\right)\mathbf{F}^T \tag{152}$$

where the elastic modulus tensor $\mathbb{C} = C_{11}\mathbb{J} + C_{12}(\mathbb{I}-\mathbb{J}) + C_{44}(\mathbf{I}\otimes\mathbf{I}-\mathbb{J})$ has cubic crystal symmetries with $C_{11}, C_{12}, C_{44}$ = 204.6, 137.7, 126.2 GPa, and $\mathbf{E}_e = \frac{1}{2}\left(\mathbf{F}_e^T\mathbf{F}_e - \mathbf{I}\right)$ is the elastic Lagrange strain. Here $[\mathbb{J}]_{ijkl} = \delta_{ij}\delta_{kl}\delta_{ik}\delta_{jl}$, $[\mathbb{I}]_{ijkl} = \frac{1}{2}\left(\delta_{ik}\delta_{jl} + \delta_{il}\delta_{jk}\right)$ and $\delta_{ij}$ is the Kronecker delta. Plastic flow can occur on any of 12 face-centered cubic (FCC) slip planes. Each crystallographic slip system, indexed by $\alpha$, is characterized by Schmid dyads $\mathbf{P}_\alpha = \mathbf{s}_\alpha \otimes \mathbf{n}_\alpha$ composed of the allowed slip direction, $\mathbf{s}_\alpha$, and the normal to the slip plane, $\mathbf{n}_\alpha$. Given the set $\{\mathbf{P}_\alpha\}$, the plastic velocity gradient is constructed via:

$$\mathbf{L}_p = \sum_\alpha \dot{\gamma}_\alpha \mathbf{P}_\alpha \ , \tag{153}$$

which is inherently volume preserving in the (incompatible) intermediate/lattice configuration. Finally, the slip rate $\dot{\gamma}_\alpha$ is related to the applied stress through the resolved shear (Mandel) stress $\tau_\alpha = \mathbf{M}\cdot\mathbf{P}_\alpha$, for that slip system. We employ a common power-law form for the slip rate relation

$$\dot{\gamma}_\alpha = \dot{\gamma}_{\alpha 0}\left|\frac{\tau_\alpha}{g_\alpha}\right|^{1/m}\tau_\alpha \ , \tag{154}$$

where $\dot{\gamma}_{\alpha 0}$ = 122.0 (MPa-s)$^{-1}$ is a reference strain rate, $m = 20$ is a rate sensitivity exponent, and $g_\alpha$ = 355.0 MPa is a hardness value. These parameters are representative of steel.

With this model in Albany [122], we simulate the polycrystalline response using a uniform mesh $20 \times 20 \times 20$ with the texture assigned element-wise (via Dream3d [123]) and strict compatibility enforced at the voxelated grain boundaries. Ten realizations with 15, 15, 17, 18, 18, 19, 19, 20, 20, 21, 22 grains were sampled from an average grain size ensemble and each grain was assigned a random orientation. Minimal boundary conditions to apply the various loading modes ( tension, shear, *etc.* ) were employed on the faces and edges of the cubical representative volumes. Also, we limit samples to a single, constant strain rate 1.0 1/s.

The simple visco-plastic (VP) model consists of a St. Venant stress rule in the current configuration with Almansi strain:

$$\mathbf{T} = \mathbb{C}\mathbf{e}_e \ , \tag{155}$$

where $\mathbb{C} = \lambda \mathbf{I} \otimes \mathbf{I} + 2\mu\mathbb{I}$ isotropic parameters $\lambda = \frac{E\nu}{(1+\nu)(1-2\nu)}$ and $\mu = \frac{E}{2(1+\nu)}$ with Young's modulus $E$ = 200 GPa and Poisson's ratio $\nu$ = 0.3, together with a simple (associative) power law for the flow rule:

$$\mathbf{D}_p = c\|\mathbf{s}\|^p \mathbf{s} \ , \tag{156}$$

where $c$ = 0.001 MPa$^{-1-p}$-s$^{-1}$ and $p$ = 0.1 are material constants.

#### 4.2.1. Neural network representation and machine learning algorithm

A typical NN, such as the representation of Eq. (144), is a two-dimensional feed-forward, directed network consisting of an input layer, output layer and $L$ intervening hidden layers where neighboring layers are densely connected. Each layer $\ell_i$ consists of $N$ nodes $(ij)$. The vector of outputs, $\mathsf{y}_i$, of the nodes $(ij), j \in (1,N)$ of layer $i$ is the weighted sum of the outputs of the previous layer $\ell_{i-1}$ offset by a threshold and passed through a ramp-like or step-like *activation* function $a(x)$:

$$\mathsf{x}_i = a(\mathsf{y}_i) \ \text{ with } \ \mathsf{y}_i = \mathsf{W}_i \mathsf{x}_{i-1} + \mathsf{b}_i \ , \tag{157}$$

where $\mathsf{W}_i$ is the weight matrix for (hidden) layer $\ell_i$ of the state/output of nodes of the previous layer $\mathsf{x}_{i-1}$ and $\mathsf{b}_i$ is the corresponding threshold vector. In our application the input layer consists of the $N_I$ invariants $I$ and the $N_{\mathcal{B}}$ elements of the tensor basis $\mathcal{B}$. The elements of $I$ form the arguments of the coefficient functions, each having a $L \times N$ neural network representation, while the elements of $\mathcal{B}$ pass through the overall network until they are combined with the coefficient functions according to Eq. (143) to form the output via a *merge* layer that does the summation. After exploring the C0 step- and ramp-like *rectifying* activation functions commonly used, we employ the ramp-like (C1 continuous) Exponential Linear Unit (ELU) [124] activation function:

$$a(x) = \begin{cases} \exp(x) - 1 & \text{if } \ x < 0 \\ x & \text{else} \end{cases} \tag{158}$$

to promote smoothness of the response and limit the depth of the network necessary to represent the response relative that necessary with saturating step-like functions.

Training the network weights $\mathsf{W}_i$ and thresholds $\mathsf{b}_i$ is accomplished via the standard back-propagation of errors [125, 126] which, in turn, drives a (stochastic) gradient-based descent (SGD) optimization scheme to minimize the so-called *loss*/error, $E$. We employ the usual root mean square error (RMSE)

$$E = \frac{1}{2N_D} \sum_{(\mathsf{x}_k, \mathsf{d}_k) \in D} \|\mathsf{y}(\mathsf{x}_k) - \mathsf{d}_k\|^2 \ , \tag{159}$$

where $D$ is the set of training data composed of inputs $\mathsf{x}_k = \{I_k, \mathcal{B}_k\}$ and corresponding output $\mathsf{d}_k$. The gradient algorithm relies on: (a) the change in $E$ with respect to each weight $\mathsf{W}_i$

$$\frac{\partial E}{\partial \mathsf{W}_i} = \underbrace{\frac{\partial E}{\partial \mathsf{x}_i} \frac{\partial \mathsf{x}_i}{\partial \mathsf{y}_i}}_{\Delta_i} \frac{\partial \mathsf{y}_i}{\partial \mathsf{W}_i} = \mathsf{x}_{i-1} \otimes \Delta_i \tag{160}$$

and (b) each threshold $\mathsf{b}_i$

$$\frac{\partial E}{\partial \mathsf{b}_i} = \underbrace{\frac{\partial E}{\partial \mathsf{x}_i} \frac{\partial \mathsf{x}_i}{\partial \mathsf{y}_i}}_{\Delta_i} \frac{\partial \mathsf{y}_i}{\partial \mathsf{b}_i} = \Delta_i \ , \tag{161}$$

where

$$\Delta_i = \left(\mathsf{W}_{i+1}^T \Delta_{i+1}\right) \odot a'(\mathsf{y}_i) \ \text{ for } \ i \neq L \ \text{ with } \ \Delta_L = \sum_{(\mathsf{x}_k, \mathsf{d}_k) \in D} (\mathsf{y}(\mathsf{x}_k) - \mathsf{d}_k) \odot a'(\mathsf{y}_L) \tag{162}$$

Here $a'$ is the derivative of weight function, $[\mathsf{a} \otimes \mathsf{b}]_{ij} = a_i b_j$ is the tensor product, and $[\mathsf{a} \odot \mathsf{b}]_i = a_i b_i$ element-wise Hadamard-Schur product. The recursion seen in Eq. (162) gives back-propagation its name. The gradient defined by these expressions is evaluated with random sampling of subset of training data $D$ called *minibatches*. Also, search for a minimum along this direction is governed by a step size called the *learning rate* in the ML community. These standard constructions are trivially generalized to the TBNN structure since the inputs $\mathcal{B}$ are not directly related to $\mathsf{W}_i$ nor $\mathsf{b}_i$, and are merely scaled by the coefficient functions to form the output $\mathsf{y}$, refer to Fig. 4-1. For more details of the SGD algorithm, see Ref. [127, Ch.2].

To begin the training, the unknown weights, $\{\mathsf{W}_i\}$, and thresholds, $\{\mathsf{b}_i\}$, are initialized with normally distributed random values to break the degeneracy of the network and enable local optimization. Since multiple local minima for training are known to exist, choosing an ensemble of initial weights which are then optimized improves the chances of finding a global minimum and the distribution of the solutions indicates the robustness of the training. Also, the full set of input data is divided into a training set $D$, used to generate the errors for the back-propagation algorithm; a test set $T$, for assessing convergence of the descent algorithm; and a third set $V$ for cross-validation, to estimate the predictive capability of the trained network. Ensuring that the errors based on $T$ are comparable to those on $V$ reduces the likelihood over-fitting data with a larger than necessary NN. We chose to divide the available data in a $T : D : V = 20{:}72{:}8$ ratio. In addition, we sample individual stress-strain curves produced by the CP and VP simulators so as to maintain approximate uniform density of data based on curve arc-length (*vs.* based on strain) to capture high-gradient (elastic) and transition (yield) regimes. Also, it should be noted that we allow ourselves to train on inputs derived from the plastic deformation gradient, $\mathbf{F}_p$, despite the

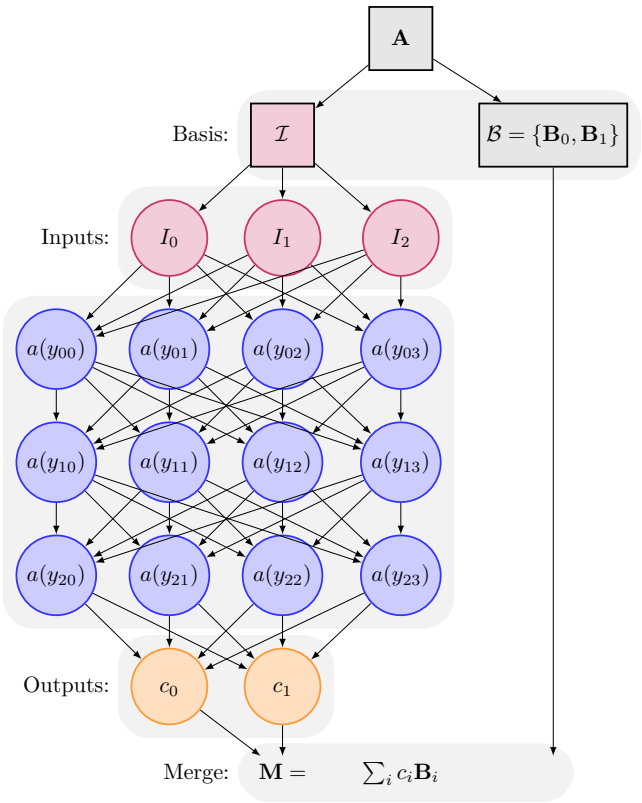


**Figure 4-1 TBNN structure for $\mathbf{M}(\mathbf{A}) = \sum_i c_i(I)\mathbf{B}_i$ with 3 invariants $I = \{I_0, I_1, I_2\}$, a $3 \times 4$ NN, 2 coefficient functions $\{c_0(I), c_1(I)\}$, and 2 tensor basis elements $\mathcal{B} = \{\mathbf{B}_0, \mathbf{B}_1\}$. The scaling operations described in Sec. 4.2.1 are omitted for clarity. The linear transformation $\mathsf{y}_i = \mathsf{W}_i\mathsf{x}_{i-1} + \mathsf{b}_i$ of the outputs $\mathsf{x}_{i-1}$ of layer $i-1$ to the inputs $\mathsf{y}_i$ of layer $i$ is denoted by the arrows connecting the nodes of layer $i-1$ to those of layer $i$. The nonlinearity of the activation functions $a(\mathsf{y}_i)$ is represented by $a(y_{ij})$ where $y_{ij}$ are the components of $\mathsf{y}_i$.**

fact that this quantity is difficult to observe directly in experiments. A critical part of the training algorithm is normalizing the data so that the NN maps $O(1)$ inputs to $O(1)$ outputs since having $\mathsf{W}_i, \mathsf{b}_i \sim O(1)$ will achieve better SGD convergence. We also shift and scale the scalar invariants $I$ so that they have a mean zero, variance one distribution. We normalize the other set of inputs, the tensor basis $\mathcal{B}$, using the maximum Frobenius norm of the basis generators, *e.g.* $\mathbf{b}_p$ and $\boldsymbol{\sigma}$, over the training set $D$. During training, the output tensors are normalized similarly based on their maximum norms over $D$, so that

$$\mathbf{f} = \sum_i \underbrace{\frac{1}{s_{\mathbf{f}}} \bar{f}_i(\bar{I}) s_{\mathbf{B}_i}}_{f_i(I)} \mathbf{B}_i \,, \tag{163}$$

where $s_{\mathbf{f}}$ is the scaling of output $\mathbf{f}$; $s_{\mathbf{B}_i}$ is the scaling of basis element $\mathbf{B}_i$ based on the powers of principal generator (*e.g.* if $\mathbf{B}_i = \mathbf{b}^a\mathbf{s}^b$ then $s_{\mathbf{B}_i} = s_{\mathbf{b}}^a s_{\mathbf{s}}^b$ where $s_{\mathbf{b}}$ is the scaling of $\mathbf{b}$); and $\bar{I} = s_{I_i} I_i$ is the set of scaled and shifted invariants. These scales have the added benefit of coarsely encoding the range of training data so the extrapolation during prediction can be detected.

Convergence is assessed by averaging the error with respect to $T$ over previous iterations of the SDG (in this work we average over the last 4-10 iterations) and terminating when this average converges, but not before performing a minimum number of iterations (1000 in this work). More discussion of the training approach can be found in [83], although in that work the learning rate was held fixed rather than decaying as the training proceeds, as in this study.

#### *4.2.2. Integration algorithm*

We need a time-integration scheme to solve the differential-algebraic system Eq. (136) and Eq. (137). We assume it is deformation driven so that $\mathbf{F} = \mathbf{F}(t)$ is data. To form a numerical integrator, we rely on the well-known exponential map

$$\mathbf{F}_{n+\alpha} = \exp\left(\alpha \Delta t \left[\mathbf{D}_p\right]_n\right) \mathbf{F}_n \tag{164}$$

which is an explicit/approximate solution to Eq. (137). In Table 4-1 we outline an adaptive scheme based on a midpoint rate at $t_{n+\alpha}$ and interpolation of the deformation gradient:

$$\log \mathbf{F}_{n+\alpha} = \log \mathbf{F}_n + \alpha \log \Delta\mathbf{F} = (1-\alpha) \log \mathbf{F}_{n+1} + \alpha \log \mathbf{F}_n \tag{165}$$

with $\Delta\mathbf{F} = \mathbf{F}_{n+1}\mathbf{F}_n^{-1}$ so $\mathbf{F}_{n+\alpha} = \exp(\alpha \log \Delta\mathbf{F})\,\mathbf{F}_n$. Since we do not rely on the NN models of stress Eq. (136) and flow (137) being directly differentiable,[1] we use a simple relaxation scheme to enforce consistency:

$$\left[\mathbf{F}_p\right]_{n+1} = \exp\left(\Delta t\, \mathbf{D}_p \left(\left[\mathbf{F}_p \mathbf{F}_p^T\right]_n, \operatorname{dev} \mathbf{T}\left(\frac{1}{2}\left(\mathbf{I} - \mathbf{F}^{-T}\left[\mathbf{F}_p^T \mathbf{F}_p\right]_n^{-1} \mathbf{F}^{-1}\right)\right)\right)\right)\left[\mathbf{F}_p\right]_n \tag{166}$$

for $\left[\mathbf{F}_p\right]_{n+1}$ given $\left[\mathbf{F}_p\right]_n$ and $\mathbf{F} \equiv \mathbf{F}_{n+1} = \mathbf{F}(t_{n+1})$. Here we have simply substituted stress and flow rules into Eq. (164) with the particular arguments $\mathbf{T}(\mathbf{e}_e)$ and $\mathbf{D}_p(\mathbf{b}_p, \mathbf{s})$. If any step has an increase in error formed from the residual of Eq. (166) the step size is cut; and, conversely, when a sub-step converges, the remainder of the interval is attempted.

[1] This relaxation could be improved by using the derivatives already computed by the backpropagation algorithm in a Newton solver with a trust region based on the bounds of the training data.

For step $n+1$

- Initialize $\mathbf{F} = \mathbf{F}_n$ and $\Delta\mathbf{F} = \mathbf{F}_{n+1}\mathbf{F}_n^{-1}$
- Sub-step: while $\alpha < 1$
- Try $\alpha = 1$, $\mathbf{F}_{n+\alpha} = \exp(\alpha \log(\Delta\mathbf{F}))\,\mathbf{F}_n$
  - Relaxation: loop over $k$, initialize $[\mathbf{F}_p]^*_{k=0} = \mathbf{F}_p$:
    1. $\mathbf{b}^*_p = \left[\mathbf{F}\mathbf{F}^T\right]^*_k$ and $\mathbf{b}^*_e = \mathbf{F}\left[\left(\mathbf{F}_p^T\mathbf{F}_p\right)^{-1}\right]^*_k\mathbf{F}^T$
    2. $\mathbf{T}^* = \mathbf{T}(\mathbf{b}^*_e)$ and $\mathbf{s}^* = \frac{1}{\det\mathbf{F}}\operatorname{dev}\mathbf{T}^*$
    3. $[\mathbf{D}_p]^*_k = \mathbf{f}(\mathbf{b}^*_p, \mathbf{s}^*)$
    4. $[\mathbf{F}_p]_{n+\alpha} = \exp\left(\alpha\Delta t\,\mathbf{D}^*_p\right)[\mathbf{F}_p]_n$
    5. if $\left\|[\mathbf{D}_p]^*_k - [\mathbf{D}_p]^*_{k-1}\right\| < \varepsilon\left\|[\mathbf{D}_p]_{k-1}\right\|$ then exit, converged
       else if $\left\|[\mathbf{D}_p]^*_k - [\mathbf{D}_p]^*_{k-1}\right\| > \left\|[\mathbf{D}_p]^*_{k-1} - [\mathbf{D}_p]^*_{k-2}\right\|$ then diverging, cut step $\alpha = 1/2\alpha$
       else $\alpha \mathrel{+}= \Delta\alpha$
  - Update $\mathbf{T}_{n+1} = \mathbf{T}^*$ and $[\mathbf{F}_p]_{n+1} = [\mathbf{F}_p]^*$

**Table 4-1 Time integration algorithm with adaptive time-stepping.**

## 4.3. Representations of the response due to microstructure

For a (single) crystal, the elastic modulus tensor $\mathbb{C}$ is defined by

$$\mathbb{C} = \boldsymbol{\partial}_{\varepsilon}\boldsymbol{\sigma}\,, \tag{167}$$

where the stress $\sigma$ and strain $\varepsilon$ states are measured in the crystal frame with axes $\{\mathbf{E}_i\}$. This stiffness tensor may be rotated to the particular orientation of the crystal in the polycrystalline aggregate $\{\mathbf{e}_i = \mathbf{R}\mathbf{E}_i\}$ via

$$\tilde{\mathbb{C}} = \mathbf{R}\boxtimes\mathbb{C} = \sum_{i,j,k,l}[\mathbb{C}]_{ijkl}\,\mathbf{R}\mathbf{E}_i\otimes\mathbf{R}\mathbf{E}_j\otimes\mathbf{R}\mathbf{E}_k\otimes\mathbf{R}\mathbf{E}_l\,, \tag{168}$$

where $\boxtimes$ is the Kronecker product.

To obtain the apparent modulus tensor $\bar{\mathbb{C}}$ of a polycrystal, it is not sufficient to simply volume-average the anisotropic elastic moduli for each grain. The compatibility and equilibrium conditions between neighboring grains create non-uniform strain and stress fields that cannot be resolved analytically. Nevertheless, two simple bounding estimates may be derived for the stiffness tensor. The Voigt average [128] for a polycrystal with grain volume fractions $\phi_g$, where $g$ indexes grains, is

$$\langle\mathbb{C}\rangle = \sum_g \phi_g\mathbb{C}_g \tag{169}$$

and the Reuss average [129] is given by

$$\langle\mathbb{C}\rangle = \left(\sum_g \phi_g\mathbb{C}_g^{-1}\right)^{-1}. \tag{170}$$

The Voigt average of the stiffnesses $\mathbb{C}$ gives an upper bound to $\bar{\mathbb{C}}$ and corresponds to the assumption that the strain state is uniform throughout the polycrystal. The Reuss average of the compliances $\mathbb{C}^{-1}$ gives a lower bound and corresponds to the assumption that the stress state is uniform. Since the grain compatibility and boundary conditions limit the accuracy of either of these assumptions, there may be a substantial discrepancy between these averages and the true elastic moduli. As mentioned, the Voigt-Reuss-Hill approximation [130] is simply the mean of the two bounds

$$\langle \mathbb{C} \rangle = \frac{1}{2} \sum_g \phi_g \mathbb{C}_g + \frac{1}{2} \left( \sum_g \phi_g \mathbb{C}_g^{-1} \right)^{-1} \tag{171}$$

This treatment typically lowers the bias relative to the two separate estimators but is equivocal to the particular boundary conditions.

For plastic response, Taylor [131] and Sachs [132] developed the corresponding theories to Voigt and Reuss. These models are generally not completely analytical and require significant computation to approximate, for example, the common problem of evolving uniaxial states of stress. Briefly, the isostrain approximation assumes the stress $\boldsymbol{\sigma}_g$ in each grain $g$ is a function of a uniform deformation gradient $\mathbf{F}$, the elastic modulus tensor $\mathbb{C}_g$, and the local material state $\mathbf{F}_g^e$ (with $\mathbf{F} \equiv \mathbf{F}_g^e \mathbf{F}_g^p$). For a uniaxial-stress deformation, the constitutive model is updated according to a prescribed $\mathbf{F}$, and a volume-averaged stress $\boldsymbol{\sigma} = \sum_g \phi_g \boldsymbol{\sigma}_g$ which is computed. A nonlinear solver must then be employed to iterate on the value of $\mathbf{F}$ until a uniaxial $\boldsymbol{\sigma}$ is obtained, subject to a constraint on $\mathbf{F}$ from the displacement-control of the effective boundary condition. In the isostress condition, a uniform stress $\boldsymbol{\sigma}$ is prescribed, and a volume-averaged displacement gradient $\mathbf{F} = \sum_g \phi_g \mathbf{F}_g$ is computed from the constitutive update. The value of $\boldsymbol{\sigma}$ must then be iterated until the constraint on $\mathbf{F}$ due to the effective boundary condition is satisfied. Either strategy (isostrain or isostress) must be applied step-wise over a finite sequence of time-steps to approximate the evolution of the material state for a given deformation history. The resulting approximations are systematically biased, with the isostrain approximation of Taylor giving and effective upper bound on the flow stress, and the isostress approximation of Sachs giving the corresponding lower bound. As in the elastic case, an approximation can be constructed based on averaging the two bounds, reducing the bias in an essentially empirical fashion.

In Ref. [3], the neural-network approach developed here is compared to these classical treatments, with separate evaluations for the elastic and elasto-viscoplastic responses. Specifically, it is shown that the neural-network approach naturally eliminates the biases exhibited by the other homogenization techniques without the need for *ad hoc* averaging.

#### *4.3.1. Neural Networks*

The basic neural network is a two-dimensional feed-forward network, often called a multilayer perceptron (MLP) [133]. It is a non-linear model that can scale to handle arbitrary complexity rapidly and, hence, is one of the most commonly employed NN architectures. As with all NNs, it has an input layer and an output layer, each with a node per scalar, and an arbitrary number of intervening layers. Adjacent layers of nodes are fully/densely connected in the sense that the state of the nodes of a layer is the vector $\mathsf{x}_i$ of outputs from the previous layer multiplied by a weight

matrix $\mathsf{W}$, added to a threshold/bias vector $\mathsf{b}_i$ (both defined per layer, here index by $i$), then mapped through an activation function $f(\mathsf{W}_i\mathsf{x}_i + \mathsf{b}_i)$ applied component-wise. In this work we employed ramp-like activation function, the sharp C0 rectified linear unit (ReLU) [134] and the C1 softplus [135] activation functions, with similar results. Adding layers between the input features and the output targets, models of arbitrary complexity may be developed but at the cost of requiring larger amounts of training/calibration data to determine the unknown weights $\mathsf{W}_i$ and biases $\mathsf{b}_i$. Using now standard algorithms, such as the stochastic gradient descent algorithm [136], the unknown parameters can be optimized to maximize the accuracy of the NN model on held-out test data.

Although MLPs are quite effective in response prediction for a modest number of inputs, it is usually impractical to train an MLP to perform regression or classification on image data, such as a voxelated realization of a polycrystal in the application at hand. The number of parameters required to feed each voxel into an MLP of sufficient complexity would currently require prohibitively large amounts of data and computing power. Furthermore, many features of interest in a given image have local, spatial correlations, and it typically effective to process subsets of voxels simultaneously since distant regions of an image are usually uncorrelated with each other.

In this section we briefly describe the proposed hybrid neural network, Fig. 4-2, and its sub-networks and their constituent layers. The proposed network is composed of: (a) an image processing component (a *convolutional* network, yellow and green)to assimilate the information in the initial microstructure ("image" input, red) relevant to the stress response, and (b) a neural network with feedback (a *recurrent* network, blue) to emulate the history dependence of the stress (output, orange) on the strain ("history" input, red). In this section we give an overview of the hybrid architecture in the context of the more traditional applications of its components. The particular component parameters, such as specific kernel size and pooling type, will be given in the Results section.

For a more detailed description of the various and now standard components of our NN refer to the texts in Refs. [127, 137], reviews Refs. [138, 139], and the documentation for Keras and Tensorflow libraries used in this work Refs. [140, 141]

#### *4.3.2. Convolutional neural network*

To resolve the issues that make application of MLPs to image data impractical, the convolutional neural network (CNN) [142] architecture was developed. Convolutional neural networks are typically used in handwriting translation, face recognition and other image processing tasks such as reconstruction. A simplified schematic of a CNN is shown in Fig. 4-2 in yellow. The image data can be represented as a matrix $\mathsf{X}$ of dimensions $n+m$, where $n$ is the number of spatial dimensions and $m$ are the number of image components, which we take to be the components of the crystallographic orientation vector $p(\mathbf{x}_I)$ at each voxel $I$. As in standard image and signal processing, a discrete convolutional kernel $\mathsf{K}$ is applied to the image, resulting in a new image $\mathsf{Y} = \mathsf{K} * \mathsf{X}$ where $*$ is the usual convolution operator. The kernel is compact in each spatial dimension and acts on rectangular subsets of pixels, effectively eliciting local features of the

image. Similar to an MLP, an activation function $f$ is then applied to each pixel of the output image to produce $\mathsf{Z} = f(\mathsf{Y})$. As in an MLP, multiple convolutional layers may be applied in succession, but it is also often effective to introduce a pooling operation, in which the image is reduced in size by taking a norm of neighboring sets of pixels and returning the filtered result into a new image. For example, the max-pooling operation applied over a $2\times2$ window in a two dimensional $10\times10$ image will find the highest value of the pixel in each disjoint $2\times2$ set and return each maximum in a new $5\times5$ image. This operation forces the network to compress the information in the image to a smaller set of features. The weight-sharing of the convolution operations and the image reductions thus provide an efficient way of processing image data in a neural network while requiring much smaller set of meta-parameters than a direct application of a MLP. Multiple replica filters with independent kernel components can be applied to input image to increase the richness of the derived features.

The output of the CNN, which is structured 3 dimensional image data in this case, may be flattened to a vector to be compatible with the input of MLP which, in this design, is a encoder. The encoder is a data compression unit usually part of a self-consistent autoencoder used to generate artificial realizations similar to the training data. The encoder, colored green in Fig. 4-2, is simply a MLP that decreases in width (number of nodes layer to layer) in order to compress the information content of the data.

The output of the encoder of image data is then fed to a recurrent neural network (RNN) colored blue in Fig. 4-2. The general class of RNNs are particularly suited to modeling history dependent data since its feedback structure accounts for causality. While a CNN takes in an image of locally structured data, a RNN takes in a sequence of data, in this case the time series of applied strains $\boldsymbol{\varepsilon}_i, i = 1,n$ and resulting stress $\boldsymbol{\sigma}_i$. An individual recurrent layer takes the state of the previous time step $\mathsf{y}_i$ and, along with a weighted version of the contemporary input $\boldsymbol{\varepsilon}_i$, to predict the output in the subsequent time step: $\mathsf{y}_{i+1} = f(\mathsf{y}_i + \mathsf{W}\boldsymbol{\varepsilon}_i)$. Similar to how a CNN processes spatial data, the same weights $\mathsf{W}$ and activation $f$ are used with each time step, thus reducing the number of parameters necessary to process the information in the series data. This design avoids the high-dimensionality of attempting to predict the entire time series simultaneously by taking advantage of the time correlation in the data. The weights $\mathsf{W}$ and state variables $\mathsf{y}_i$ are trained by comparing the prediction error $||\boldsymbol{\sigma}_i - \mathsf{y}_i||$ sequentially at each time step $i$ and updating the parameters to reduce the observed error. An RNN encodes time dependence through evolving state variables $\mathsf{y}_i$ and thus avoids the need for observing the full history at once to make predictions. In this work we employ a more complex but widely adopted version of an RNN composed of long short-term memory units (LSTM) [143]. The LSTM includes a set of additional internal variables and weights that increase the influence of data from earlier in the series on the current state of the network. Similar to the CNN architecture, the output from a recurrent neural network (RNN) is fed into an (linear, mixing) MLP to increase the feature richness before yielding the output.

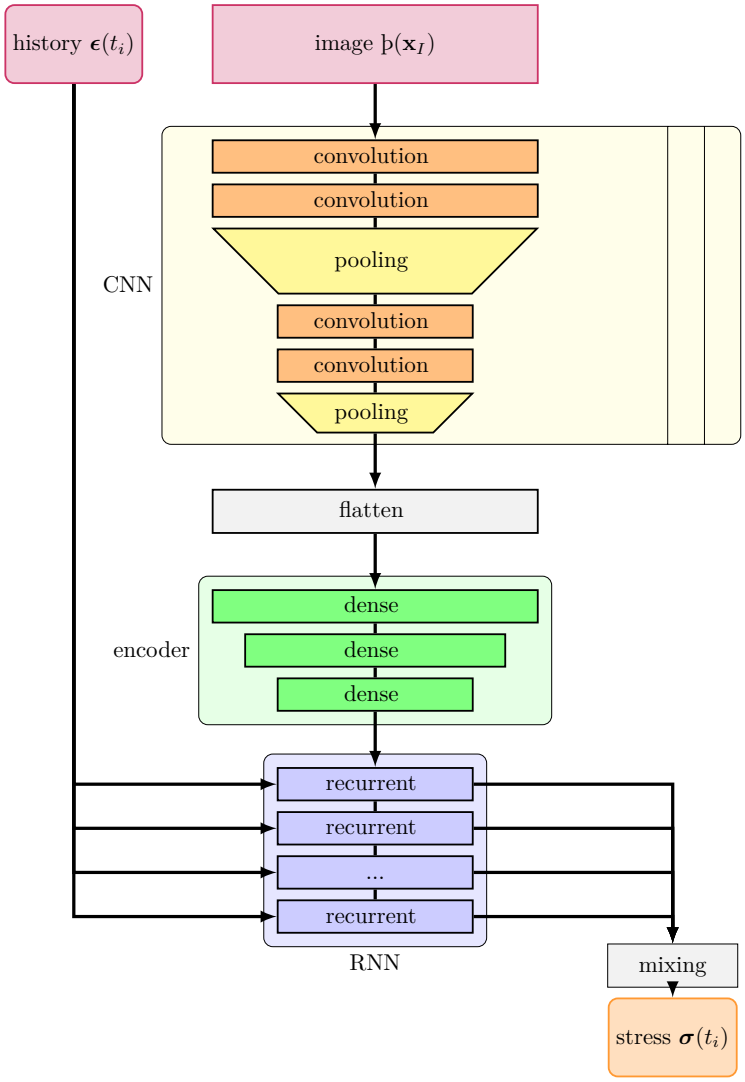


**Figure 4-2 Hybrid neural network architecture with convolutional neural network (CNN, yellow), encoder (decreasing width feed forward NN, green), and recurrent neural network (RNN, blue, shown in an "unrolled" diagram) components. Note that independent CNNs are simultaneously applied to the image and their output is combined in the flatten operation that takes the spatially correlated outputs and produces a vector of this on-grid data. The inputs are the strain history $\boldsymbol{\varepsilon}_i = \boldsymbol{\varepsilon}(t_i)$ over a sequence of times $t_i, i = 0, n$ and initial microstructure $p_I = p(\mathbf{x}_I)$ at the image voxels $\mathbf{x}_I$ (red). The output is stress $\boldsymbol{\sigma}_i$ at corresponding times (orange).**

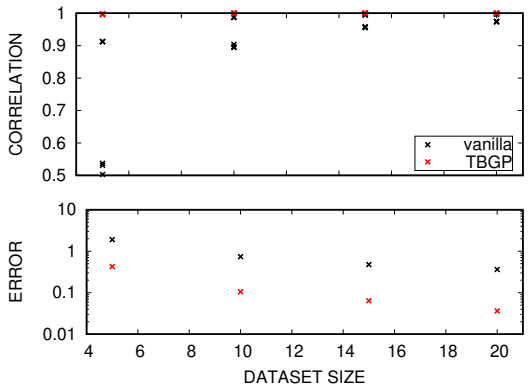


**Figure 5-1 Comparison of the tensor basis Gaussian process to a traditional Gaussian process of stress response. The tensor basis model has superior accuracy and correlation with the data.**

# 5. CONCLUSION

The project has been very productive as evidenced by the number of papers and presentations enumerated in Sec. 1. There are also a number of tantalizing and important developments that have been produced as the project is coming to a close. These latest results will be the basis for follow-on work.

## 5.1. A tensor basis Gaussian process model

We have developed neural network models of mechanical response that respect exact symmetries and invariances (see Sec. 4). Neural networks are effective when thousands of data points are available. Not all applications can support this amount of training data, so we have also extended the tensor basis formulation to Gaussian process modeling. Fig. 5-1 shows that the tensor basis formulation is distinctly superior to traditional implementations of Gaussian process models of stress-strain data. Alternatively we have consider multi-fidelity techniques that allow us to augment expensive, accurate experimental data with less costly lower-scale simulation data.

## 5.2. Predicting full field crystal plasticity response with neural networks

As an extension of the convolutional-recurrent neural network we developed to predict the stress-strain response of a particular microstructure, we developed a similar network to predict the full field evolving stress response. Fig. 5-2 shows the fidelity of the full stress field predictions with the underlying model. For this dataset, correlation of $> 95\%$ was achieved across the deformation process. These models can be used instead of the expensive crystal plasticity models used to train them, in particular they can be used as accurate surrogate models in UQ studies.

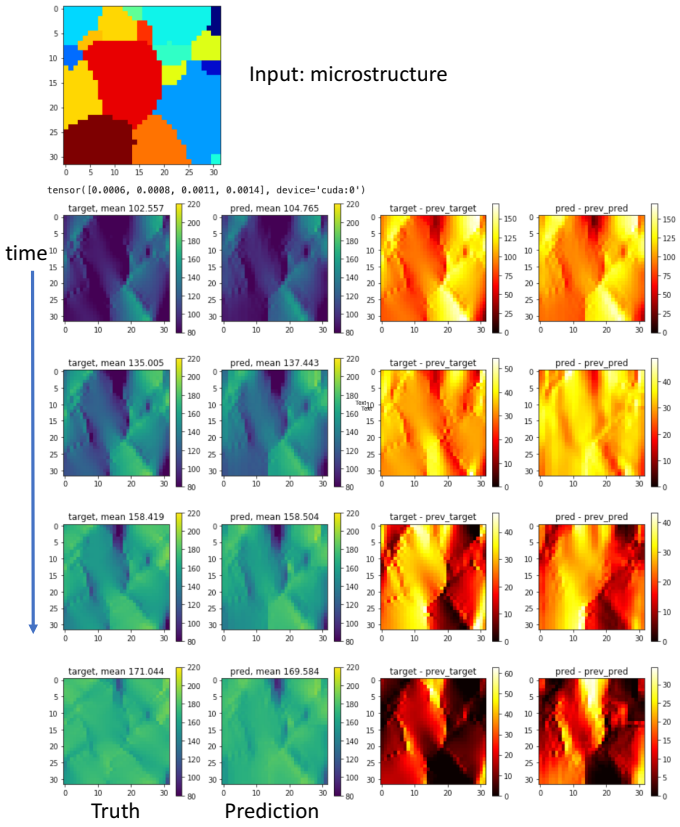


**Figure 5-2 Neural network predictions of the full field stress evolutions. Top: the microstructure used for the predictions. Left: comparison of the predictions of the evolution of the 11 stress field in response to tension and the true fields given by the underlying model. Right: comparison of the predictions of the evolution of stress differences from step to step and the underlying model.**

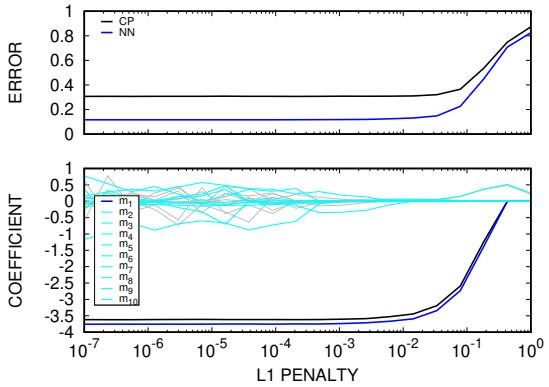


**Figure 5-3 Sensitivity of sparse linear model of the crystal plasticity (CP) model used to create the data and sparse linear model of the neural network (NN) model trained on the data. A L1 penalty is used to enforce sparsity and the sparse linear model is most useful where the penalty is high but not so high as to affect accuracy. The NN clearly represents the underlying model's sensitivity to the first moment of the grain size distribution and the insensitivity to the higher moments. The error in the sparse linear model of the NN is lower since the NN representation of the data is simpler.**

## 5.3. Interpretability of image based neural network models

Since it is well-known that neural networks, and in particular image-based neural networks, can make seemingly accurate predictions for the wrong reasons, we investigated the interpretability and sensitivity of our models using a variety of techniques. Fig. 5-3 shows that that convolutional neural network model trained on initial microstructures has the same global sensitivities as the underlying model. Hence, we have some confidence that the predictions are based on physical aspects of the training images.

# REFERENCES

[1] Francesco Rizzi, Mohammad Khalil, Reese E Jones, Jeremy A Templeton, Jakob T Ostien, and Brad L Boyce. Bayesian modeling of inconsistent plastic response due to material variability. *Computer Methods in Applied Mechanics and Engineering*, 353:183–200, 2019.

[2] Reese Jones, Jeremy A Templeton, Clay M Sanders, and Jakob T Ostien. Machine learning models of plastic flow based on representation theory. *Computer Modeling in Engineering & Sciences*, pages 309–342, 2018.

[3] Ari L Frankel, Reese E Jones, Coleman Alleman, and Jeremy A Templeton. Predicting the mechanical response of oligocrystals with deep learning. *Computational Materials Science*, 169:109099, 2019.

[4] Brad L Boyce, Bradley C Salzbrenner, Jeffrey M Rodelas, Laura P Swiler, Jonathan D Madison, Bradley H Jared, and Yu-Lin Shen. Extreme-value statistics reveal rare failure-critical defects in additive manufacturing. *Advanced Engineering Materials*, 2017.

[5] N.M. Heckman, T.A. Ivanoff, A.M. Roach, B.H. Jared, D.J. Tung, H.J. Brown-Shaklee, T. Huber, D.J. Saiz, J.R. Koepke, J.M. Rodelas, J.D. Madison, B.C. Salzbrenner, L.P. Swiler, R.E. Jones, and B.L. Boyce. Automated high-throughput tensile testing for process optimization and process-aware design. *In preparation*, 2019.

[6] A Needleman. Void growth in an elastic-plastic medium. *Journal of Applied Mechanics*, 39(4):964–970, 1972.

[7] Jeffrey Koplik and A Needleman. Void growth and coalescence in porous plastic solids. *International Journal of Solids and Structures*, 24(8):835–853, 1988.

[8] Richard W Hertzberg. Deformation and fracture mechanics of engineering materials. 1989.

[9] Ejaz Ahmad, Tanvir Manzoor, Kanwar Liaqat Ali, and JI Akhter. Effect of microvoid formation on the tensile properties of dual-phase steel. *Journal of materials engineering and performance*, 9(3):306–310, 2000.

[10] John G Cowie, Morris Azrin, and Gregory B Olson. Microvoid formation during shear deformation of ultrahigh strength steels. *Metallurgical transactions A*, 20(1):143–153, 1989.

[11] Walter D Pilkey and Deborah F Pilkey. *Peterson's stress concentration factors*. John Wiley & Sons, 2008.

[12] Rudolph Earl Peterson and R Plunkett. Stress concentration factors, 1975.

[13] Jonathan Pegues, Michael Roach, R Scott Williamson, and Nima Shamsaei. Surface roughness effects on the fatigue strength of additively manufactured ti-6al-4v. *International Journal of Fatigue*, 116:543–552, 2018.

[14] Hassel M. Ledbetter. Monocrystal-polycrystal elastic constants of a stainless steel. *physica status solidi (a)*, 85:89–96, 1984.

[15] J. D. Eshelby. The determination of the elastic field of an ellipsoidal inclusion, and related problems. *Proceedings of the Royal Society of London. Series A, Mathematical and Physical Sciences*, 241(1226):376–396, 1957.

[16] T. Mori and K. Tanaka. Average Stress in Matrix and Average Elastic Energy of Materials with Misfitting Inclusions. *Acta Metallurgica*, 21:571–574, 1973.

[17] Ekkehart Kröner. Berechnung der elastischen konstanten des vielkristalls aus den konstanten des einkristalls. *Zeitschrift für Physik*, 151(4):504–518, 1958.

[18] W. Voigt. Ueber die beziehung zwischen den beiden elasticitätsconstanten isotroper körper. *Annalen der Physik*, 274(12):573–587, 1889.

[19] A. Reuss. Berechnung der fließgrenze von mischkristallen auf grund der plastizitätsbedingung für einkristalle . *Zeitschrift für Angewandte Mathematik und Mechanik*, 9(1):49–58, 1929.

[20] Rodney Hill. The elastic behaviour of a crystalline aggregate. *Proceedings of the Physical Society A*, 65:349–354, 1952.

[21] Erik Vanmarcke. *Random Fields: Analysis and Synthesis*. MIT Press, Cambridge, MA, 1983.

[22] Masanobu Shinozuka and George Deodatis. Simulation of multi-dimensional gaussian stochastic fields by spectral representation. *Applied Mechanics Reviews*, 49(1):29–53, 1996.

[23] Marc C Kennedy and Anthony O'Hagan. Bayesian calibration of computer models. *Journal of the Royal Statistical Society: Series B (Statistical Methodology)*, 63(3):425–464, 2001.

[24] D.S. Sivia. *Data Analysis: A Bayesian Tutorial*. Oxford Science, 1996.

[25] Youssef M. Marzouk, Habib N. Najm, and Larry A. Rahn. Stochastic spectral methods for efficient bayesian solution of inverse problems. *Journal of Computational Physics*, 224(2):560 – 586, 2007.

[26] F. Rizzi, O.M. Knio, H.N. Najm, B.J. Debusschere, K. Sargsyan, M. Salloum, and H. Adalsteinsson. Uncertainty Quantification in MD Simulations. Part II: Inference of force-field parameters. *SIAM J. Multiscale Model. Simul.*, 10(4):1460–1492, 2012.

[27] F. Rizzi, R. E. Jones, B. J. Debusschere, and O. M. Knio. Uncertainty quantification in md simulations of concentration driven ionic flow through a silica nanopore. ii. uncertain potential parameters. *The Journal of Chemical Physics*, 138(19):194105, 2013.

[28] K. Sargsyan, H. N. Najm, and R. Ghanem. On the Statistical Calibration of Physical Models. *International Journal for Chemical Kinetics*, 47(4):246–276, 2015.

[29] Dani Gamerman and Hedibert F Lopes. *Markov chain Monte Carlo: stochastic simulation for Bayesian inference*. CRC Press, 2006.

[30] Bernd A Berg and Alain Billoire. *Markov chain Monte Carlo simulations*. Wiley Online Library, 2008.

[31] Dave Higdon, Marc Kennedy, James C Cavendish, John A Cafeo, and Robert D Ryne. Combining field data and computer simulations for calibration and prediction. *SIAM Journal on Scientific Computing*, 26(2):448–466, 2004.

[32] Maria J Bayarri, James O Berger, Rui Paulo, Jerry Sacks, John A Cafeo, James Cavendish, Chin-Hsu Lin, and Jian Tu. A framework for validation of computer models. *Technometrics*, 49(2):138–154, 2007.

[33] John Tinsley Oden, Ivo Babuška, and Danial Faghihi. Predictive computational science: Computer predictions in the presence of uncertainty. In *Encyclopedia of Computational Mechanics Second Edition*, pages 1–26. American Cancer Society, 2017.

[34] C. Soize. A nonparametric model of random uncertainties for reduced matrix models in structural dynamics. *Probabilistic Engineering Mechanics*, 15(3):277–294, 2000.

[35] M. Strong and J. Oakley. When is a model good enough? Deriving the expected value of model improvement via specifying internal model discrepancies. *SIAM/ASA J Uncertainty Quantification*, 2:106–125, 2014.

[36] Yanyan He and Dongbin Xiu. Numerical strategy for model correction using physical constraints. *Journal of Computational Physics*, 313:617–634, 2016.

[37] Pascal Pernot and Fabien Cailliez. A critical review of statistical calibration/prediction models handling data inconsistency and model inadequacy. *AIChE Journal*, 63(10):4642–4665, 2017.

[38] Souleymane Zio, Henrique F. da Costa, Gabriel M. Guerra, Paulo L.B. Paraizo, Jose J. Camata, Renato N. Elias, Alvaro L.G.A. Coutinho, and Fernando A. Rochinha. Bayesian assessment of uncertainty in viscosity closure models for turbidity currents computations. *Computer Methods in Applied Mechanics and Engineering*, 342:653 – 673, 2018.

[39] Rebecca E. Morrison, Todd A. Oliver, and Robert D. Moser. Representing model inadequacy: A stochastic operator approach. *SIAM/ASA J Uncertainty Quantification*, 6(2):457–496, 2018.

[40] Layal Hakim, Guilhem Lacaze, Mohammad Khalil, Khachik Sargsyan, Habib Najm, and Joseph Oefelein. Probabilistic parameter estimation in a 2-step chemical kinetics model for n-dodecane jet autoignition. *Combustion Theory and Modelling*, 22(3):446–466, 2018.

[41] Gabriel Terejanu. From model calibration and validation to reliable extrapolations. In *Model Validation and Uncertainty Quantification, Volume 3*, pages 205–211. Springer, 2016.

[42] Rebecca E Morrison, Todd A Oliver, and Robert D Moser. Representing model inadequacy: A stochastic operator approach. *SIAM/ASA Journal on Uncertainty Quantification*, 6(2):457–496, 2018.

[43] Maher Salloum and Jeremy A Templeton. Inference and uncertainty propagation of atomistically informed continuum constitutive laws, part 2: Generalized continuum models based on gaussian processes. *International Journal for Uncertainty Quantification*, 4(2), 2014.

[44] Maher Salloum and Jeremy A Templeton. Inference and uncertainty propagation of atomistically informed continuum constitutive laws, part 2: Generalized continuum models based on gaussian processes. *International Journal for Uncertainty Quantification*, 4(2), 2014.

[45] J. Berger and L. Pericchi. The intrinsic bayes factor for model selection and prediction. *Journal of the American Statistical Association*, 91:109–122, 1996.

[46] I. Verdinelli and L. Wasserman. Bayes factors, nuisance parameters, and imprecise tests. In J. M. Bernardo, J. O. Berger, A. P. Dawid, and A. F. M. Smith, editors, *Bayesian Statistics 5*, pages 765–771. Oxford University Press, London, 1996.

[47] J.L. Beck. Bayesian system identification based on probability logic. *Structural Control and Health Monitoring*, 17(7):825–847, 2010.

[48] Robert E Kass and Adrian E Raftery. Bayes factor review; improper prior. *Journal of the American Statistical Association*, 90(430):pp. 773–795, 1995.

[49] M. Muto and J.L. Beck. Bayesian Updating and Model Class Selection for Hysteretic Structural Models Using Stochastic Simulation. *Journal of Vibration and Control*, 14(1-2):7–34, 2008.

[50] Rimple Sandhu, Chris Pettit, Mohammad Khalil, Dominique Poirel, and Abhijit Sarkar. Bayesian model selection using automatic relevance determination for nonlinear dynamical systems. *Computer Methods in Applied Mechanics and Engineering*, 320:237–260, 2017.

[51] Sadanori Konishi and Genshiro Kitagawa. *Information Criteria and Statistical Modeling (Springer Series in Statistics)*. Springer, oct 2007.

[52] Jennifer C Naylor and Adrian FM Smith. Applications of a method for the efficient computation of posterior distributions. *Applied Statistics*, pages 214–225, 1982.

[53] Qing Liu and Donald A Pierce. A note on gauss-hermite quadrature. *Biometrika*, 81(3):624–629, 1994.

[54] Mohammad Khalil and Habib N. Najm. Probabilistic inference of reaction rate parameters from summary statistics. *Combustion Theory and Modelling*, 22(4):635–665, 2018.

[55] O.P. Le Maître and O.M. Knio. *Spectral Methods for Uncertainty Quantification*. Springer, New York, NY, 2010.

[56] N. Wiener. The Homogeneous Chaos. *Am. J. Math.*, 60:897–936, 1938.

[57] R.G. Ghanem and P.D. Spanos. *Stochastic Finite Elements: A Spectral Approach*. Springer Verlag, New York, 1991.

[58] D. Xiu and G.E. Karniadakis. The Wiener-Askey polynomial chaos for stochastic differential equations. *SIAM Journal on Scientific Computing*, 24(2):619–644, 2002.

[59] Y. M. Marzouk, H. N. Najm, and L. A. Rahn. Stochastic spectral methods for efficient Bayesian solution of inverse problems. *Journal of Computational Physics*, 224(2):560–586, 2007.

[60] Dongbin Xiu. *Numerical methods for stochastic computations: a spectral method approach*. Princeton university press, 2010.

[61] Mohammad Khalil, Guilhem Lacaze, Joseph C. Oefelein, and Habib N. Najm. Uncertainty quantification in LES of a turbulent bluff-body stabilized flame. *Proceedings of the Combustion Institute*, 35(2):1147–1156, 2015.

[62] DJ Bammann, ML Chiesa, and GC Johnson. Modeling large deformation and failure in manufacturing processes. *Theoretical and Applied Mechanics*, 9:359–376, 1996.

[63] Mark F Horstemeyer and Arun M Gokhale. A void–crack nucleation model for ductile metals. *International Journal of Solids and Structures*, 36(33):5029–5055, 1999.

[64] Arthur A Brown and Douglas J Bammann. Validation of a model for static and dynamic recrystallization in metals. *International Journal of Plasticity*, 32:17–35, 2012.

[65] Kyle N Karlson, James W Foulk, Arthur A Brown, and Michael G Veilleux. Sandia fracture challenge 2: Sandia california's modeling approach. *International Journal of Fracture*, 198(1-2):179–195, 2016.

[66] J. A. Quiblier. A new three-dimensional modeling technique for studying porous media. *Journal of Colloid and Interface Science*, 98(1):84–102, 1984.

[67] P. M. Adler, C. G. Jacquin, and J. A. Quiblier. Flow in simulated porous media. *International Journal of Multiphase Flow*, 16(4):691–712, 1990.

[68] C. L. Y. Yeong and S. Torquato. Reconstructing random media. *Phys. Rev. E*, 57:495–506, 1998.

[69] Olivier Le Maître and Omar M Knio. *Spectral methods for uncertainty quantification: with applications to computational fluid dynamics*. Springer Science & Business Media, 2010.

[70] S. J. J. Ilango, S. Sarkar, and A. Sameen. Reconstruction of 2-D porous media using karhunen–lóeve expansion. *Probabilistic Engineering Mechanics*, 32:56–65, 2013.

[71] P. Guttorp and P. D. Sampson. Methods for estimating heterogeneous spatial covariance functions with environmental applications. In *Environmental Statistics*, volume 12 of *Handbook of Statistics*, pages 661–689. Elsevier, 1994.

[72] B. D. Ripley. *Spatial Statistics*. John Wiley, 1981.

[73] N. Cressie. *Statistics for Spatial Data*. John Wiley, 1991.

[74] Rolland L. Hardy. Multiquadric equations of topography and other irregular surfaces. *Journal of Geophysical Research (1896-1977)*, 76(8):1905–1915, 1971.

[75] N. Dyn, D. Levin, and S. Rippa. Numerical procedures for surface fitting of scattered data by radial functions. *SIAM Journal on Scientific and Statistical Computing*, 7(2):639–659, 1986.

[76] M. J. D. Powell. Algorithms for approximation. chapter Radial Basis Functions for Multivariable Interpolation: A Review, pages 143–167. Clarendon Press, New York, NY, USA, 1987.

[77] R. Jin, W. Chen, and T.W. Simpson. Comparative studies of metamodelling techniques under multiple modelling criteria. *Structural and Multidisciplinary Optimization*, 23(1):1–13, 2001.

[78] H.-M. Gutmann. A radial basis function method for global optimization. *Journal of Global Optimization*, 19(3):201–227, 2001.

[79] Jerome Sacks, Susannah B. Schiller, and William J. Welch. Designs for computer experiments. *Technometrics*, 31(1):41–47, 1989.

[80] Xin Wei, Yi-Zhong Wu, and Li-Ping Chen. A new sequential optimal sampling method for radial basis functions. *Applied Mathematics and Computation*, 218(19):9635 – 9646, 2012.

[81] T. Bedford and R. Cooke. *Probabilistic risk analysis: foundations and methods*. Cambridge University Press, 2001.

[82] Robert L. Winkler. Uncertainty in probabilistic risk assessment. *Reliability Engineering & System Safety*, 54(2):127–132, 1996.

[83] Julia Ling, Reese Jones, and Jeremy Templeton. Machine learning strategies for systems with invariance properties. *Journal of Computational Physics*, 318:22–35, 2016.

[84] Peter J Olver. *Applications of Lie groups to differential equations*, volume 107. Springer Science & Business Media, 2000.

[85] Roe Goodman and Nolan R Wallach. *Representations and invariants of the classical groups*, volume 68. Cambridge University Press, 1998.

[86] Roe Goodman and Nolan R Wallach. *Symmetry, representations, and invariants*, volume 255. Springer, 2009.

[87] David H Sattinger and Oliver L Weaver. *Lie groups and algebras with applications to physics, geometry, and mechanics*, volume 61. Springer Science & Business Media, 2013.

[88] Clifford Truesdell and Walter Noll. The non-linear field theories of mechanics. In *The non-linear field theories of mechanics*, pages 1–579. Springer, 2004.

[89] Morton E Gurtin. *An introduction to continuum mechanics*, volume 158. Academic press, 1982.

[90] Ronald S Rivlin. Further remarks on the stress-deformation relations for isotropic materials. *Journal of Rational Mechanics and Analysis*, 4:681–702, 1955.

[91] Ronald S Rivlin and Gerald F Smith. On identities for $3\times$ 3 matrices. In *Collected Papers of RS Rivlin*, pages 1550–1558. Springer, 1997.

[92] Ronald Samuel Rivlin and Jerald LaVerne Ericksen. Stress-deformation relations for isotropic materials. *Journal of Rational Mechanics and Analysis*, 4:323–425, 1955.

[93] C-C Wang. On a general representation theorem for constitutive relations. *Archive for Rational Mechanics and Analysis*, 33(1):1–25, 1969.

[94] C-C Wang. A new representation theorem for isotropic functions: An answer to professor gf smith's criticism of my papers on representations for isotropic functions. *Archive for rational mechanics and analysis*, 36(3):166–197, 1970.

[95] BR Seth. Generalized strain measure with applications to physical problems. Technical report, Wisconsin University-Madison, Mathematics Research Center, 1961.

[96] R Hill. On constitutive inequalities for simple materials-I. *Journal of the Mechanics and Physics of Solids*, 16(4):229–242, 1968.

[97] TC Doyle and Jerald L Ericksen. Nonlinear elasticity. In *Advances in applied mechanics*, volume 4, pages 53–115. Elsevier, 1956.

[98] George C Johnson and Douglas J Bammann. A discussion of stress rates in finite deformation problems. *International Journal of Solids and Structures*, 20(8):725–737, 1984.

[99] LAszLo SzABo and Mihály Balla. Comparison of some stress rates. *International journal of solids and structures*, 25(3):279–297, 1989.

[100] P Haupt and Ch Tsakmakis. On the application of dual variables in continuum mechanics. *Continuum Mechanics and Thermodynamics*, 1(3):165–196, 1989.

[101] P Haupt and Ch Tsakmakis. Stress tensors associated with deformation tensors via duality. *Archives of Mechanics*, 48(2):347–384, 1996.

[102] GF Smith and Richard S Rivlin. Stress-deformation relations for anisotropic solids. *Archive for Rational Mechanics and Analysis*, 1(1):107–112, 1957.

[103] GF Smith and Richard S Rivlin. The anisotropic tensors. *Quarterly of Applied Mathematics*, 15(3):308–314, 1957.

[104] AJM Spencer. The formulation of constitutive equation for anisotropic solids. In *Mechanical Behavior of Anisotropic Solids/Comportment Méchanique des Solides Anisotropes*, pages 3–26. Springer, 1982.

[105] JM Zhang and J Rychlewski. Structural tensors for anisotropic solids. *Archives of Mechanics*, 42(3):267–277, 1990.

[106] Bob Svendsen. On the representation of constitutive relations using structure tensors. *International journal of engineering science*, 32(12):1889–1892, 1994.

[107] Q-S Zheng. Theory of representations for tensor functions–a unified invariant approach to constitutive equations. *Applied Mechanics Reviews*, 47(11):545–587, 1994.

[108] Erastus H Lee. Elastic-plastic deformation at finite strains. *Journal of applied mechanics*, 36(1):1–6, 1969.

[109] Vlado A Lubarda. Constitutive theories based on the multiplicative decomposition of deformation gradient: Thermoelasticity, elastoplasticity, and biomechanics. *Applied Mechanics Reviews*, 57(2):95–108, 2004.

[110] Jacob Lubliner. *Plasticity theory*. Dover, 2008.

[111] Bernard D Coleman and Walter Noll. The thermodynamics of elastic materials with heat conduction and viscosity. *Archive for Rational Mechanics and Analysis*, 13(1):167–178, 1963.

[112] J.C. Simo and T.J.R. Hughes. *Computational Inelasticity*. Springer New York, New York, NY, 1998.

[113] Morton E Gurtin, Eliot Fried, and Lallit Anand. *The mechanics and thermodynamics of continua*. Cambridge University Press, 2010.

[114] Jean-Paul Boehler. Representations for isotropic and anisotropic non-polynomial tensor functions. In *Applications of tensor functions in solid mechanics*, pages 31–53. Springer, 1987.

[115] Geoffrey Ingram Taylor. The mechanism of plastic deformation of crystals. part i. theoretical. *Proceedings of the Royal Society of London. Series A*, 145(855):362–387, 1934.

[116] E Kroner. On the plastic deformation of polycrystals. *Acta Metallurgica*, 9(2):155–161, 1961.

[117] JFW Bishop and Rodney Hill. Xlvi. a theory of the plastic distortion of a polycrystalline aggregate under combined stresses. *The London, Edinburgh, and Dublin Philosophical Magazine and Journal of Science*, 42(327):414–427, 1951.

[118] JFW Bishop and Rodney Hill. CXXVIII. A theoretical derivation of the plastic properties of a polycrystalline face-centred metal. *The London, Edinburgh, and Dublin Philosophical Magazine and Journal of Science*, 42(334):1298–1307, 1951.

[119] Jean Mandel. Généralisation de la théorie de plasticité de WT Koiter. *International Journal of Solids and structures*, 1(3):273–295, 1965.

[120] Paul R Dawson. Computational crystal plasticity. *International journal of solids and structures*, 37(1-2):115–130, 2000.

[121] Franz Roters, Philip Eisenlohr, Luc Hantcherli, Denny Dharmawan Tjahjanto, Thomas R Bieler, and Dierk Raabe. Overview of constitutive laws, kinematics, homogenization and multiscale methods in crystal plasticity finite-element modeling: Theory, experiments, applications. *Acta Materialia*, 58(4):1152–1211, 2010.

[122] Albany: a Trilinos-based PDE code. https://github.com/gahansen/Albany. Accessed: 2017-09-30.

[123] Dream3d: Open, extensible software environment to allow integrated processing, characterization and manipulation of microstructure digitally. http://dream3d.bluequartz.net. Accessed: 2017-09-30.

[124] Djork-Arné Clevert, Thomas Unterthiner, and Sepp Hochreiter. Fast and accurate deep network learning by exponential linear units (elus). *arXiv preprint arXiv:1511.07289*, 2015.

[125] Paul Werbos. Beyond regression: New tools for prediction and analysis in the behavior science. *Unpublished Doctoral Dissertation, Harvard University*, 1974.

[126] David E. Rumelhart, Geoffrey E. Hinton, and Ronald J. Williams. Learning representations by back-propagating errors. *Nature*, 323(6088):533–538, 1986.

[127] Michael A Nielsen. *Neural networks and deep learning*. Determination Press, 2015.

[128] Woldemar Voigt. *Lehrbuch der kristallphysik (mit ausschluss der kristalloptik)*. Springer-Verlag, 2014.

[129] A Reuss. Berechnung der fließgrenze von mischkristallen auf grund der plastizitätsbedingung für einkristalle. *ZAMM-Journal of Applied Mathematics and Mechanics/Zeitschrift für Angewandte Mathematik und Mechanik*, 9(1):49–58, 1929.

[130] Richard Hill. The elastic behaviour of a crystalline aggregate. *Proceedings of the Physical Society. Section A*, 65(5):349, 1952.

[131] Geoffrey Ingram Taylor. Plastic strain in metals. *J. Inst. Metals*, 62:307–324, 1938.

[132] G Sachs. Plasticity problems in metals. *Transactions of the Faraday Society*, 24:84–92, 1928.

[133] Frank Rosenblatt. Principles of neurodynamics. perceptrons and the theory of brain mechanisms. Technical report, Cornell Aeronautical Lab Inc., Buffalo NY, 1961.

[134] Laura Resteghini, Pier Luca Lanzi, Roberto Nebuloni, Carlo Riva, Carlo Capsoni, and Piero Gabellini. Single-objective genetic algorithm for dynamic optimization of reconfigurable antenna systems. In *Antennas and Propagation (EuCAP), 2013 7th European Conference on*, pages 1333–1335. IEEE, 2013.

[135] Charles Dugas, Yoshua Bengio, François Bélisle, Claude Nadeau, and René Garcia. Incorporating second-order functional knowledge for better option pricing. In *Advances in neural information processing systems*, pages 472–478, 2001.

[136] Herbert Robbins and Sutton Monro. A stochastic approximation method. In *Herbert Robbins Selected Papers*, pages 102–109. Springer, 1985.

[137] Ian Goodfellow, Yoshua Bengio, and Aaron Courville. *Deep Learning*. MIT Press, 2016. http://www.deeplearningbook.org.

[138] Michael Egmont-Petersen, Dick de Ridder, and Heinz Handels. Image processing with neural networks—a review. *Pattern recognition*, 35(10):2279–2301, 2002.

[139] Yann LeCun, Yoshua Bengio, and Geoffrey Hinton. Deep learning. *nature*, 521(7553):436, 2015.

[140] François Chollet et al. Keras. https://keras.io, 2015.

[141] Martín Abadi, Ashish Agarwal, Paul Barham, Eugene Brevdo, Zhifeng Chen, Craig Citro, Greg S. Corrado, Andy Davis, Jeffrey Dean, Matthieu Devin, Sanjay Ghemawat, Ian Goodfellow, Andrew Harp, Geoffrey Irving, Michael Isard, Yangqing Jia, Rafal Jozefowicz, Lukasz Kaiser, Manjunath Kudlur, Josh Levenberg, Dandelion Mané, Rajat Monga, Sherry Moore, Derek Murray, Chris Olah, Mike Schuster, Jonathon Shlens, Benoit Steiner, Ilya Sutskever, Kunal Talwar, Paul Tucker, Vincent Vanhoucke, Vijay Vasudevan, Fernanda Viégas, Oriol Vinyals, Pete Warden, Martin Wattenberg, Martin Wicke, Yuan Yu, and Xiaoqiang Zheng. TensorFlow: Large-scale machine learning on heterogeneous systems, 2015. Software available from tensorflow.org.

[142] Yann LeCun, Yoshua Bengio, et al. Convolutional networks for images, speech, and time series. *The handbook of brain theory and neural networks*, 3361(10):1995, 1995.

[143] Sepp Hochreiter and Jürgen Schmidhuber. Long short-term memory. *Neural computation*, 9(8):1735–1780, 1997.

Sandia National Laboratories

Sandia National Laboratories is a multimission laboratory managed and operated by National Technology & Engineering Solutions of Sandia LLC, a wholly owned subsidiary of Honeywell International Inc., for the U.S. Department of Energy's National Nuclear Security Administration under contract DE-NA0003525.